THE DESIGN OF TACTILE SENSORS AND THEIR ELASTIC COVER

Ph.D. dissertation

Gábor Vásárhelyi

Supervisor:
Ferenc Kovács, D.Sc.
Doctor of the Hungarian Academy of Sciences

Scientific adviser:
Tamás Roska, D.Sc.
Ordinary Member of the Hungarian Academy of Sciences

fides et ratio

Péter Pázmány Catholic University
Faculty of Information Technology
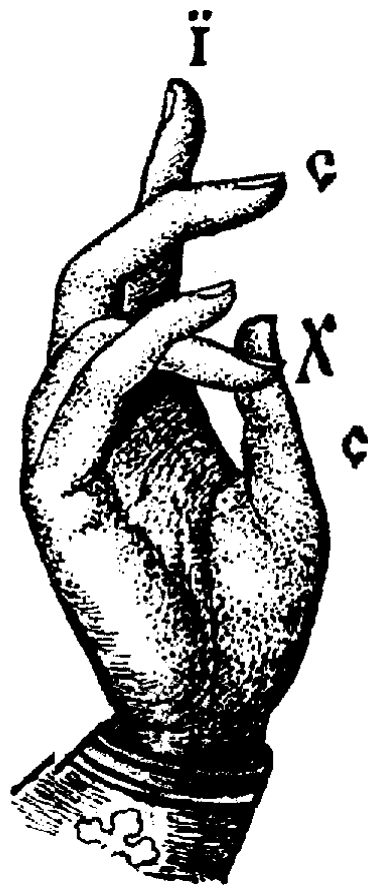Multidisciplinary Technical Sciences Doctoral School

Budapest 2007

„MŰHELY HAIKU:

Talán hozzá se nyúlj. Csak nézd és nézd, míg csak gyönyörű nem lesz.”

Fodor Ákos

"WORKROOM HAIKU:

Maybe don't even touch it. Just look at it, just look until it gets beautiful."

Ákos Fodor

Acknowledgments

First of all, I would like to say thanks to my scientific adviser Tamás Roska, who could always waste his precious time on me by giving the most useful suggestions at the very time I needed them. Thanks are also due to my supervisor Ferenc Kovács for his wide-ranging help.

Thanks especially to all my colleagues at the Research Institute for Technical Physics and Materials Science of the Hungarian Academy of Sciences; to Csaba Dücső, my honorary consultant for the motivation and the indispensable consultations, to Mária Ádám for the enthusiastic and precise help with the sensor development, to Attila Nagy for his unbelievable patience and dexterity in assembling the sensors, to Gyuri Juhász for the stepper motor drive, to Béla Forgács and his group for the measurement setup and the realization of all the stupid ideas that came into my mind, to István Bársony for leading this very group, and finally, to all of them, including those I forgot to mention for their infinite amount of humanity.

Special credits are also due to the fellows at the Doctoral School of the Pázmány University; to Péter Szolgay and Attila Kis for the long-lasting joint work during these years—to Attila also for the good company throughout the haptic conferences. Thanks to Tamás Bárdi, László Havasi and Dani Hillier for their outstanding help with the devil world of computers, and in addition, to Anna Lázár, Zoltán Fodróczi, István Kóbor and the "second year students" for the general good company, useful or useless conversations and the common meals.

Thanks especially to our neurobiologists, László Négyessy, Zoltán Vidnyánszky and József Hámori for providing the basis of the interdisciplinarity at the Doctoral School.

The following temporary consultants deserve special thanks for the enormously motivating technical suggestions: István Páczelt (Miskolc University, Department of Mechanics), Gábor Stépán and László Szabó (Technical University of Budapest, Department of Applied Mechanics), Henrik Farkas (Technical University of Budapest,

THE DESIGN OF TACTILE SENSORS AND THEIR ELASTIC COVER

by

Gábor Vásárhelyi

Abstract

Tactile sensors are artificial analogues of the tactile receptors found in our skin. They measure features of the local contact forces between an object or a surface and the sensor. The commercially-available artificial tactile-sensor arrays are usually only pressure sensors; namely, they measure only the normal load component. In collaboration with the Institute for Technical Physics and Materials Science of the Hungarian Academy of Sciences we developed a three-axial tactile-sensor array that is also capable of detecting the additional two shear-force components, i.e. the ones that are parallel to the surface. In my work I participated in the development, experimentation and system-level integration of these devices, but I mainly focused on the examination and design of the skin-like elastic cover of these sensors. The elastic cover is the first spatial-temporal, dynamic signal-processing layer of the sensor structure with continuous-space input and discrete-space output. Therefore, it plays a crucial role in determining the sensor's overall characteristics. This dissertation mainly focuses on aspects of this mechanical-coding behavior of the elastic cover. First, I introduce the mathematical description of the elastic layer and approve the feasibility of the model by experimental results. Then, I give an analytic solution to a special case of the cover's inverse problem, namely, I show how to extract components of the surface load from the measured signals that are coded by the elastic layer. Finally, I show how the neuromorphic design of the cover's shape can alter the overall coding mechanism of the elastic layer. I thoroughly investigate the role of fingerprint-like elastic hemispheres emerging from the cover surface and apply them on the three-axial sensors and on general pressure-sensor arrays as well to efficiently enhance the capabilities of these devices.

TABLE OF CONTENTS

Chapter One

INTRODUCTION

1.1. Preface

Touch is a fundamental and intriguing sensory modality that is also the least known from many points of view. It is fundamental because tactile information is truly indispensable for our everyday life. Intriguing because it is the only modality that maps the environment through its "tangible" physical reality on the whole body, without having the sensory receptors located in a specific organ. Most of the other modalities sense the world remotely, through secondary physical substances emitted by the observed distant objects. Vision requires scattered light, hearing makes use of the reflected or generated auditory waves, olfaction calls for molecules traveling in the air. In contrast, tactile sensation through concrete physical contact informs us unquestionably about the surroundings. If we see a mirage but we cannot touch it, we know that it is not there. Conversely, if we bump into a glass door, we will notice it for sure, even if we could not perceive it visually. In other words, in case of controversial information coming from more modalities at once, tactile sensation will be the dominant one in many cases.

In general, tactile modality is a truly important sensory system of ours that once being investigated or modeled scientifically, reveals deep beauty and brings on fascination. My Ph.D. work also concerns the sense of touch, but in place of the biological systems it builds on artificial tactile sensors.

The heart of my research is a tactile-sensor array developed at the Institute for Technical Physics and Materials Science of the Hungarian Academy of Sciences (MTA MFA). This tiny MEMS (Micro-Electro-Mechanical-Systems) device encloses sensory and signal-processing elements. It is novel in the manner that compared to the commercially-available pressure-sensor arrays, it can measure, process and pass on not one, but three components of the surface load, namely, not only the one perpendicular to the surface but the two shear components as well. During my work I participated in the development, experimentation and system-level integration of these devices, but in my research I

mainly focused on the examination and design of the skin-like elastic cover of the sensors.

The elastic cover is an indispensable key component of the tactile sensors. Besides providing a certain amount of physical protection, it also plays a fundamental role in the overall procedure of sensation, as a mechanical information-coding layer between the sensors and the environment (let us just think about the increased tactile sensitivity around an abrasion, or our thickening sole during the summer holidays). The elastic layer transfers the surface forces to the sensors in the form of distributed mechanical stress/strain/deformation, no matter which system—mechanoreceptors in the deep skin or artificial tactile sensors—receive them. Consequently, the *elastic cover* can be treated as the *first spatial-temporal, dynamic information-coding layer* of the sensory structure.

My first task was to model and understand this non-trivial, spatial-temporal coding mechanism. In the second run I used an inverse approach—I investigated how I could determine the surface load distribution from the measured, coded signals by making use of the coding mechanism or, alternatively, by intentionally *designing* the geometry and physical parameters of the elastic layer using neuromorphic features in the sensor design.

1.2. Methods of investigation

Before working with artificial tactile sensors, it is worth to get acquainted with one of Nature's many masterpieces, the *human* (or any other living organism's) *tactile system*. All components of an artificial tactile sensor can be associated with parts of the biological analogue; therefore, for a neuromorphic design we can obtain many great ideas from the big old evolution that started its development millions of years ago. It is simply unwise to start working with tactile sensors without gaining knowledge about the neurobiology of touch, the function of the mechanoreceptors or the anatomical structure or mechanical behavior of the skin.

The sensing paradigm of the MEMS devices used in my work is the *piezoresistive effect*. When a piezoresistive material is exposed to mechanical load, it changes its resistivity proportionally to the strain in the material. Our sensors include deformable micro-bridges that contain embedded piezoresistors. Therefore, for the design and evaluation of the

sensors we certainly need some knowledge about the MEMS technology in general and the piezoresistive effect in particular.

Continuum-mechanics is the key word for the mathematical description of the elastic cover of the sensors. In the first run, the elastic matter can be treated as a homogeneous, isotropic, infinite *half-space* that obeys Hooke's law. The input forces act on the only open surface of the half-space, and create a complex stress profile inside the material. Since the stress is mostly concentrated around the indentation and decays rapidly with distance, we can fairly approximate the behavior of the real, finite rubber with the infinite half-space at a depth corresponding to the real rubber thickness. The first task is now to solve the equilibrium equations of the rubber for a given surface-indentation profile, and find the stress/strain/deformation distribution at that specific depth. The inverse problem is about the regeneration of the surface indentation profile from discrete number of strain measurements under the rubber.

The first solutions to the direct problem of the elastic half-space were found a long time ago, around the end of the nineteenth century; yet, the elastic theory had nothing to do with tactile sensors then. It was only in the mid-eighties of the last century when the model became the primary mathematical description of the skin and the artificial cover of pressure sensors, however, with three degree-of-freedom sensors in view, the theory still calls for enhancement.

One of my results is that as an analogue to the finger ridges, I changed the surface of the flat cover to a certain, defined shape. Consequently, the half-space model could not be used any more in the original form. Therefore, as an extension of the elastic half-space, I made a *finite-element model* in contribution with Balázs Fodor to be able to describe the cover with the new geometry as well.

The sensors of the MTA MFA were tested and developed with a *special experimental setup.* In the measurement system the sensors are fixed to a table that can be tilted and moved subtly with a high-precision stepper motor. The sensors can be loaded with forces of different angle and amplitude, acting on a single point or a bigger area. The signals go through an amplification stage developed at our lab and are finally transferred to a computer equipped with special evaluation software.

1.3. Framework of the dissertation

Chapter Two will introduce us to the biology of touch. We will get to know the different types and function of the human mechanoreceptors and gain knowledge about the structure and mechanical behavior of the skin, its different layers and components, with special attention to the function of finger ridges and hairs.

In Chapter Three I will give an introduction to the piezoresistive effect and the most important features of the MEMS sensor structure. I will present our experimental setup and the first experimental results concerning the characteristics and behavior of the pure sensors.

In Chapter Four we will get through the mathematical description of the elastic cover of the sensors using continuum-mechanics and the elastic half-space model. I will show how parameters of a flat cover change the characteristics of the sensors, and prove the feasibility of the mathematical model with experimental results.

Chapter Five is about the inverse problem of the flat elastic cover. I will show the analytic solution of the inverse problem for a point load, and use the deduced equations for creating tactile hyper-accuracy over the receptive field of the flat cover.

In Chapter Six I will talk about neuromorphic elements that can be used in the sensor design to enhance the overall capabilities of the device. I will show some experimental results on the modified behavior of the sensors, which also offer us clear clues on the role of these elements in biological systems. In the same chapter I will also investigate the role of elastic hemispheres that emerge from the flat cover surface. I will show the results of a finite-element simulation of the hemispheres and reveal the many advantages these elements bring to the sensor design, including the simplification of the elastic material's coding mechanism or the possibility for a 1D to 3D conversion of an arbitrary tactile array. I will support the hypotheses of this chapter with real measurements and an application example.

Chapter Seven is a summary with a list of the new scientific results and the future trends our devices might bring into view. A publication list and a detailed and commented bibliography are given at the end, too.

1.3.1. General notes

The references in the dissertation appear in the form (Lastname et al., 2003 [85]), where "Lastname" is the last name of the first author, "2003" is the date of publication and "[85]" is the reference number in the bibliography. I did not want to put only the numbers as a reference, but I could not exclude them either, because the bibliography at the end of the dissertation is ordered according to the scientific laboratories or main research topics, therefore, it cannot appear in alphabetical order.

During the following hundred pages I used *singular* form when the scientific results were the product of only my brain and body. I used *plural* form in the case of joint works and in general discussions during the introductions and conclusions.

Chapter Two

THE SKIN AND ITS MECHANORECEPTORS

2.1. Introduction

Besides the well-known fact that part of the skin is just a simple dead tissue, it encompasses quite a lot of intriguing features and components. The skin itself—as the outermost wrap of our body—is responsible for a basic physical protection against mechanical damage, dehydration, ultraviolet light, severe temperature loss or gain, contamination or diseases. In the meantime, it contains several elements that map different features of the surrounding environment. We can find heat, humidity, proprioceptive or pain sensors embedded in the tissue of the skin and obviously different kinds of tactile receptors as well. While this tissue perfectly fulfils all the requirements these parts demand, gives place to the connections to the nervous system, the blood flow or the immune system, it also determines the characteristics of the tactile sensation by its pure mechanical structure.

A general neurobiological (and some anatomical) description of the skin and its mechanoreceptors can be found in (Kandel et al., 2000 [75]). A good review on the roles and functions of the mechanoreceptors is also given by K. O. Johnson (2001 [17]). In the following, we will restrict our investigations to two main features of the skin. First, we will get a description of the functional anatomy of the four basic tactile receptors that lie in our skin. Second, we will summarize briefly the research results concerning the mechanical structure and characteristics of the skin tissue itself, with special attention to the role hairs and fingerprints play in tactile sensation. The goal of this chapter is to give a brief introduction to those elements of the biological system that can support us with neuromorphic ideas in the artificial tactile-sensor design.

2.2. The four mechanoreceptors of the human skin

Like in vision, the sensory information of the tactile modality travels through the nervous system in parallel channels. The human eye contains millions of similar receptors that signal proportionally to the received light. After a retinal pre-processing, the parallel information gets to the optic nerve in the form of thirty or more so-called retinotopic

channels. The further coding of the neuronal signals more or less preserves this topography, where each channel is responsible for a special feature of the visual scene. In the tactile modality the roles of the first structures in the signaling path are a little bit mixed. The first signal-coding layer is represented by the skin itself, and the parallel channels are separated *after* this coding, according to the different receptor types embedded in the deep layers of the skin. In the human skin there are four main parallel signaling-channels rooting in the four main mechanoreceptor types: the Merkel disc, the Meissner's and Pacinian corpuscle and the Ruffini organ (Figure 2.1).
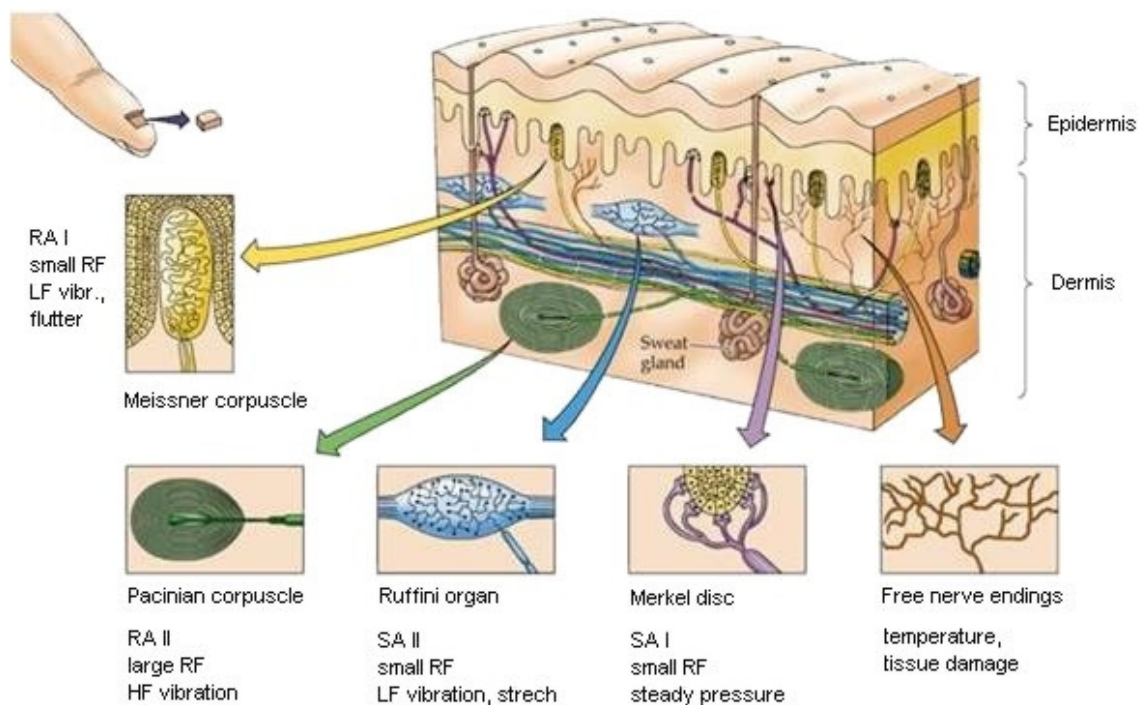
Figure 2.1. The four main mechanoreceptors of the skin with their schematic structure and location (Kandel et al., 2000 [75]). Basic properties of each type are added to the original image.

In the following we will take a look at each receptor type separately, to analyze and compare their function and to get a general view of what kind of tactile information is important for our brain. If we believe that nature is an expert in touch, the knowledge stolen from it might be useful in a later artificial tactile-sensor design.

2.2.1. The Merkel disc

Merkel cells are probably the most precisely described mechanoreceptors, first identified by Friedrich Sigmund Merkel in 1875, as the first known "touch cells" of the glabrous and hairy skin. Merkel corpuscles are oval or discoid in shape with a length of 10−15 µm

along the longer axis, and have spike-like protrusions all around to attach themselves to the surrounding skin tissue (Figure 2.2).
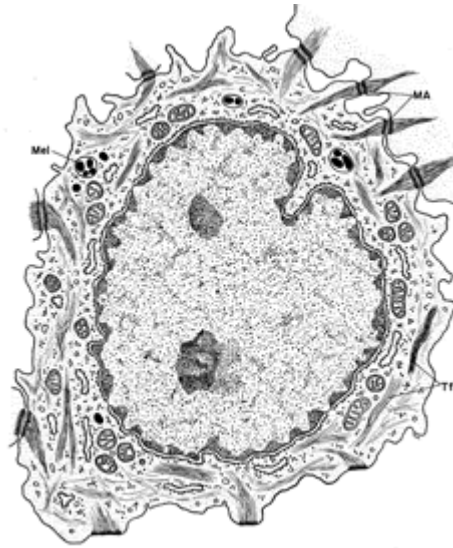
Figure 2.2. The structure of a Merkel cell;
image source: http://www.bioeng.auckland.ac.nz/physiome/images_map.php

Because of their small size and dense appearance, their location being relatively close to the skin surface and their special micro-structure showing slow-adaptation (SA) properties they are most suitable for the high-resolution mapping of constant or low frequency (5−15 Hz) pressure, fine texture, contours or local curvature[1] of the touched surface. Merkel cells are usually found in small clusters, where each cell is connected to one nerve ending, and overlapping clusters of the nerve endings are collected in one single dorsal root ganglion cell (Figure 2.3). Therefore, the spinal neurons will have overlapped receptive fields, with many close peaks in each one. The diameter of the receptive field of one neuron is around 2 mm on our fingers, which is relatively small compared to the ones of the other mechanoreceptors.

---

[1] Contours and local curvature are sensed purely because of the mechanical-stress coding mechanism of the *skin* itself, as we will see later in section 4.2.5.
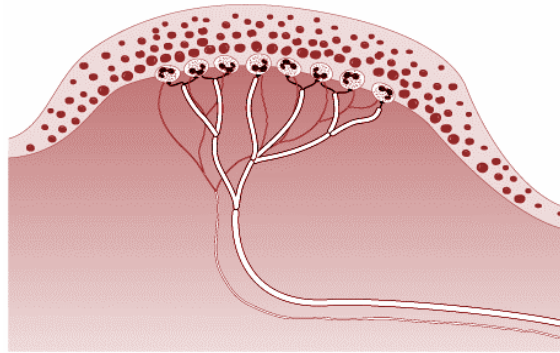
Figure 2.3. Clusters of Merkel cells under the center of a fingerprint ridge. The signal of the receptors in each cluster is collected by one dorsal root ganglion cell; image source: http://www.ilo.org/encyclopaedia/

The location of the Merkel cells in the skin is quite instructive. On the ridged human finger they are mostly located along the center line of the papillary ridges, near the penetration of the sweat gland ducts. In the hairy skin they are situated within the outer root sheath of hair follicles. In one of the most developed tactile structures, the nose of the star-nosed mole, they are located just at the center-base of the so called Eimer's organ (Figure 2.4). Later, when we will have knowledge about the mechanical stress transmission properties of the skin, we will show theoretical and experimental results why these locations are the best for the Merkel cells to be at.

For more anatomical and functional details about the Merkel corpuscles, see (Ogawa, 1996 [61]), (Halata et al., 2003 [62]) or (Moll et al., 2005 [63]).
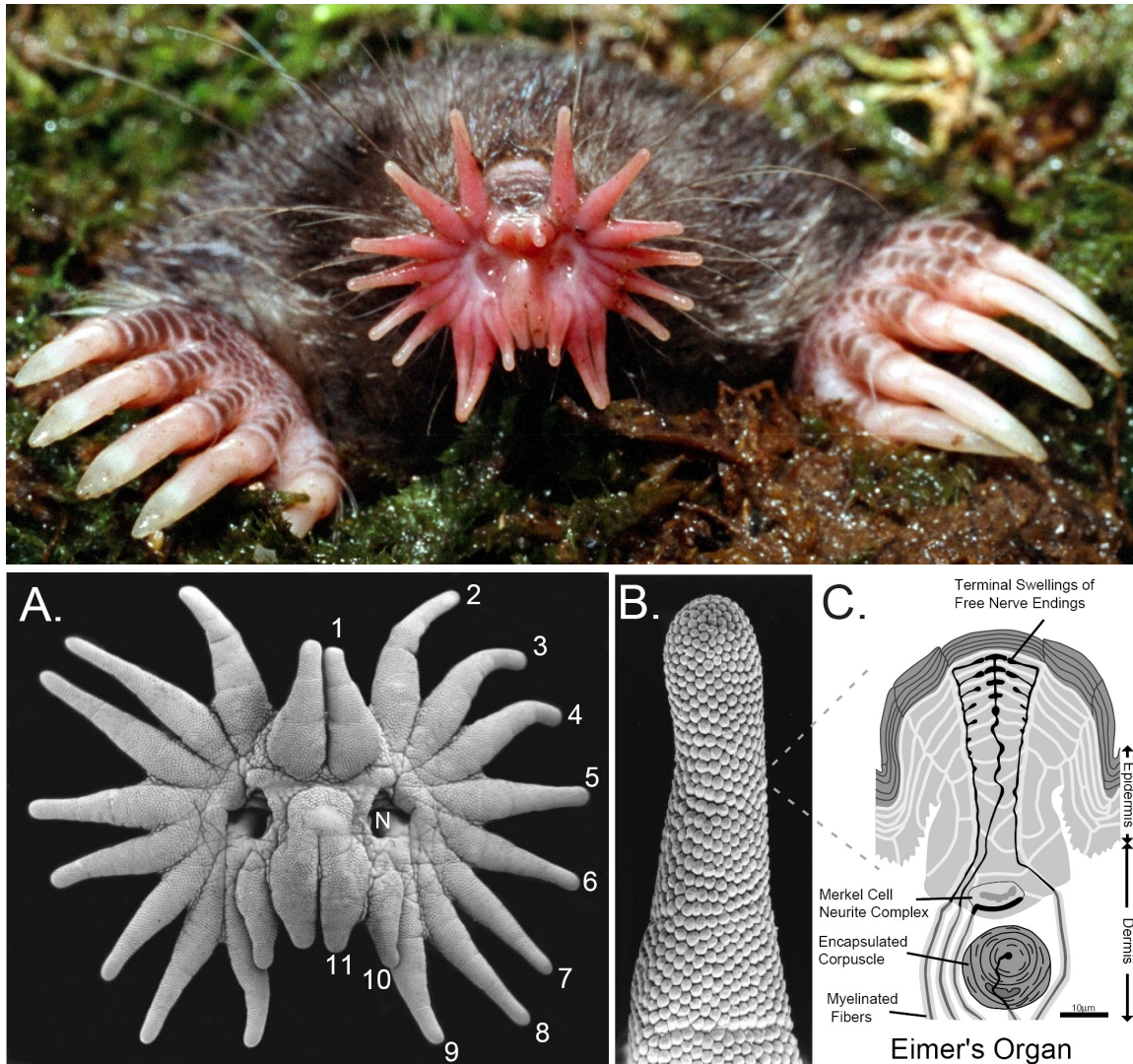
Figure 2.4. One of the most sophisticated tactile organs of the world is the nose of the star-nosed mole (A). It consists of 22 appendages with thousands of mechanoreceptive Eimer's organs on each (B). Each organ is a specialization of the epidermis into a bump-like structure (C). Merkel cells and other tactile receptors are found at the base of each bump (Catania, 1999 [64])

2.2.2. The Meissner's corpuscles

Meissner's corpuscle (discovered by the anatomist Georg Meissner) is the other type of mechanoreceptor that can be found in the superficial layers of the skin with relatively high density. It consists of flattened supportive cells arranged as horizontal lamellae surrounded by a connective tissue capsule (Figure 2.5). They are usually 20-40 µm in diameter and up to 150 µm long.
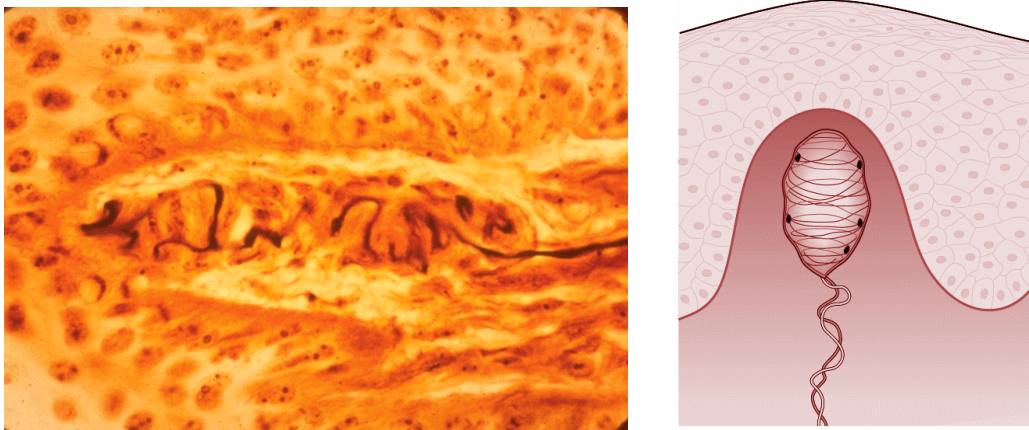
Figure 2.5. Microscopic (left) and schematic (right) view of the Meissner's corpuscle, surrounded by the epidermal skin tissue; image sources: http://www.udel.edu/Biology/Wags/histopage/colorpage/cin/cin.htm (left), http://www.ilo.org/encyclopaedia (right)

The Meissner's corpuscles are located at the border of the dermis and epidermis, where they are mechanically coupled to the papillary ridges. According to (Bolanowski and Pawson, 2003 [68]), in the fingertip of primates they are also positioned along the fingerprint ridges (predicting an important role for the fingerprints in the mechanotransduction). They are rapidly adapting (RA) mechanoreceptors that signal features of motion, the feeling of stroking, fluttering, rubbing or palpation, in the frequency range of 20−50 Hz. Since they are located relatively close to the surface, they also have small receptive field (2−3 mm in diameter). The structure of their receptive field is also similar to the one of the Merkel cells, because these receptors can be found in clusters, too.

2.2.3. The Pacinian corpuscle

The Pacinian corpuscle was named again after its discoverer, the Italian anatomist Filippo Pacini. It is similar in physiology to the Meissner's corpuscle, but larger in size (around 1−2 mm in diameter) and fewer in number. Each corpuscle consists of up to a hundreds of concentric lamellae composed of fibrous connective tissue and fibroblasts, separated by gelatinous material. In the center of the corpuscle there is a fluid-filled cavity with a single afferent nerve ending (Figure 2.6).
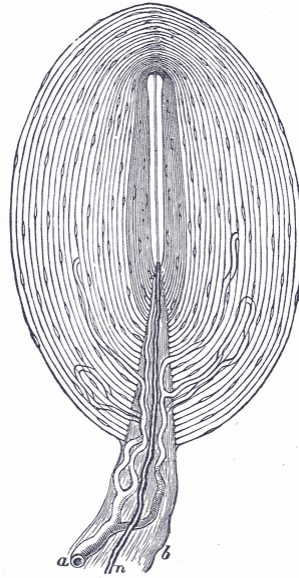
Figure 2.6. Schematic drawing of a Pacinian corpuscle with its many lamellae and a single nerve fiber rooting in the center; image source: http://wikipedia.org

Due to the fine, layered structure, the Pacinian corpuscles are very sensitive to the high-frequency vibrations of up to 400 Hz. Since vibrations are not local but travel in the tissues without being weakened, these corpuscles are found only in the deep subcutaneous tissue, scattered, with high receptive-field size. Obviously, the receptive field in this case has only one peak point at the central zone above the corpuscle.

2.2.4. The Ruffini organ

The last mechanoreceptor is the Ruffini organ, described by Ruffini (not surprisingly). It is oval or even more stretched in shape, and consists of strong connective-tissue sheaths, inside which the nerve fibers divide into numerous branches (Figure 2.7).
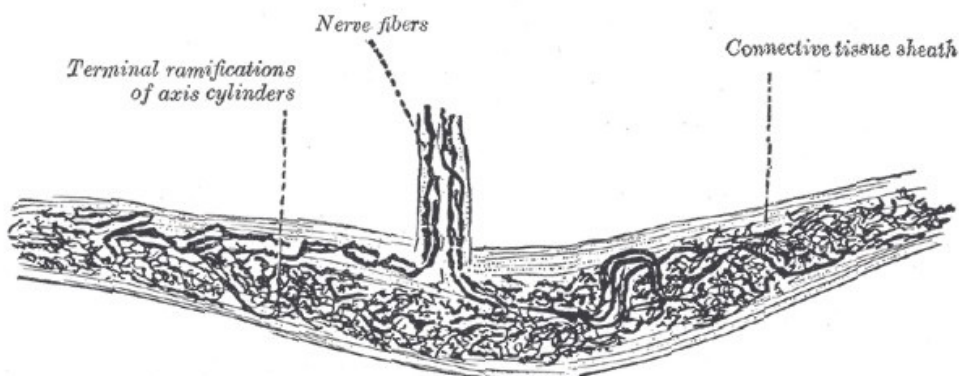
Figure 2.7. Drawing of Ruffini about the Ruffini organ;
image source: http://www.bartleby.com/107/illus937.html

Ruffini endings are principally situated at the junction of the corium with the subcutaneous tissue, and therefore respond to the movement of joints, bending of nails or the lateral stretch of the surrounding skin tissue. Like in the case of the Pacinian corpuscle, due to the deep location and one-to-one innervation, the receptive field of the Ruffini organ is again large and has a central zone of maximum sensitivity.

2.2.5. Comparison of the mechanoreceptor channels

As a quick overview, I summarized the main properties of the introduced four mechanoreceptive channels into Table 2.I.

TABLE 2.I. COMPARISON OF THE FOUR MECHANORECEPTOR CHANNELS

property	Merkel discs	Meissner's corpuscles	Pacinian corpuscles	Ruffini endings
afferent type	SA I	RA I (or RA)	RA II (or PC)	SA II
sensed features	constant or low-frequency (5–15 Hz) pressure, fine image of texture, contours or surface curvature	transient, phasic, vibratory stimuli; stroking, fluttering, rubbing, palpation, edge detection, microslip, (20–50 Hz)	high-frequency vibrations (60–400 Hz)	lateral skin-stretch, bending of fingernail, movements of joints
location	basal layer of epidermis, mostly under the center of the surface ridges	border of dermis and epidermis, mechanically coupled to papillary ridges	deep subcutaneous tissue	deep subcutaneous tissue (dermis), sometimes close to joints, nails
receptive field on fingertip	small (Ø 2 mm), highly localized with many peaks	small, (Ø 2-3 mm), with many peaks	large, with a central zone of maximal sensitivity	large, with a central zone of maximal sensitivity
innervation	10–25 receptors to one dorsal root ganglion cell	10–25 receptors to one dorsal root ganglion cell	one neuron to each receptor	one neuron to each receptor
stimulus coding	firing rate proportional to local peak stress (and therefore to surface curvature)	One action potential at the peak of sinusoidal stimulus. Firing rate proportional to speed of motion, intensity is coded in no. of active nerves	One action potential at every peak of the vibration. Therefore, motion speed on texture is coded in firing rate. Intensity is coded in no. of active fibers	firing rate is proportional to applied steady (lateral) force

In the above section we saw that there are two crucial parameters that define the characteristics of the receptors. Their *location* in the skin determines their receptive field size and envisages which physical properties are the most suitable for a given receptor to measure. Their *structure* is differentiated accordingly to make them more selective to these specific features. In the next section we will see how these aspects come together through the mechanical properties of the skin tissue itself.

2.3. Structure and behavior of the skin

The skin is a pretty complex multilayered elastic structure, showing inhomogeneous, nonlinear, viscoelastic, thermoelastic and many other types of evil properties. It consists of two main layers: the outer skin or *epidermis*, and the inner skin, the *dermis*. The epidermis is constantly being worn away and replaced by new tissue generated by an upper sub-layer of the dermis. The surface of the skin is often not smooth; it has fingerprint ridges, sweat glands and/or hair on it. In spite of (or due to) all its complexity, many researchers tried to analyze the behavior of the skin as a mechanical layer, having a central role in the processing of tactile signals traveling from the skin surface down to the receptor sites. In the following I will give a brief review of the presently available skin models concerning the mechanical behavior of the skin, in the hope that they can provide us with useful hints for the design of artificial covers.

2.3.1. The skin as an elastic half-space

The first mathematical skin model was described by Johnson and Phillips (1981) in a fantastic article trilogy ([14], [15], [16]). They deformed the fingertip of rhesus monkeys with differently shaped objects, and measured their neural response in the peripheral nerves, analyzing the output of the four different mechanoreceptive channels. In the meantime, they proposed that the skin should be treated as an information-coding layer and should be described by the theory of elasticity. They used the so called elastic half-space model with the solution of Boussinesq (1885 [39]) to describe the stress/strain distribution in an elastic material, caused by the indentation that was used on the monkey's fingers. They stated that the response of the mechanoreceptors is determined by the mechanical properties of the surrounding skin layer, and the shape of the measured neural response over the receptive field of each receptor (Figure 2.8) is similar

to the distribution of a specific stress/strain component of the half-space model loaded with the same indentation profiles.
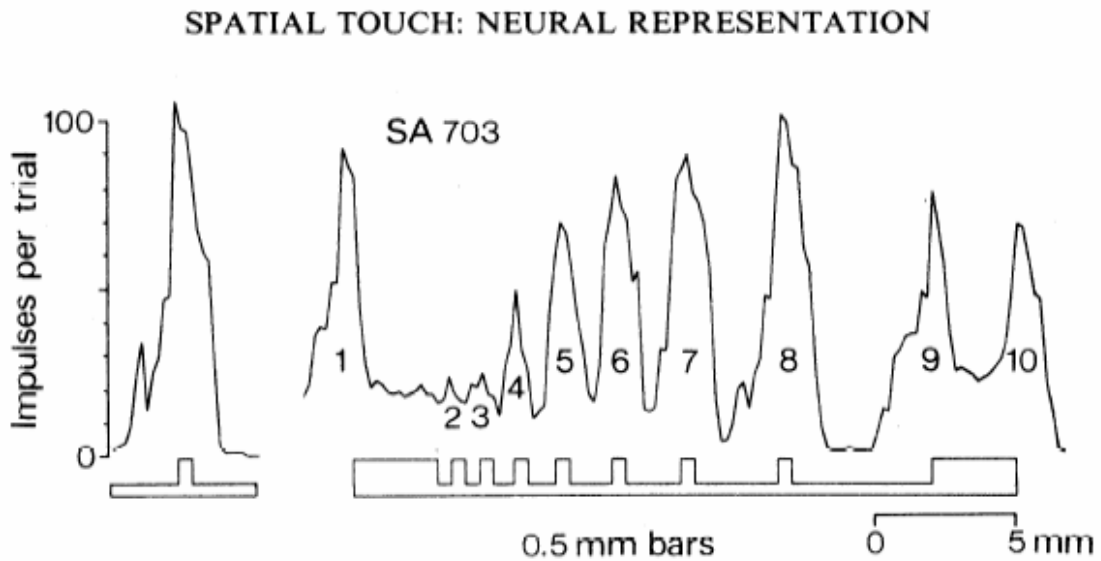
Figure 2.8. Neural response of a Merkel cell in the fingertip of a rhesus monkey, caused by the depicted bar as an indentation to the skin. The response amplitude is measured by the average number of action potentials over a short period of time after the specific indentation. The response profile follows the characteristics of the stress/strain distribution described by the elastic half-space model (Johnson and Phillips, 1981 [15])

According to the measurement results and the comparison with the different stress/strain components of the model, they stated that due to the characteristic edge-enhancing and surround-inhibition properties of the Merkel cell response, it most likely responds to the local maximum compressive strain. Furthermore, the best (but not good enough) approximation to the response of the Meissner's corpuscles is given by the maximum horizontal tensile strain.

Phillips and Johnson were the first to connect the response of the mechanoreceptors with the continuum-mechanics of the skin, hence starting a new and promising approach in the description of biological or artificial tactile sensors.

2.3.2. Finite-element model of the fingertip

Srinivasan and Dandekar (1996 [18]) built the first finite-element model of the primate fingertip. They created three models with different complexity (including bones, different layers, but no fingerprint ridges), and compared their behavior under load with the elastic half-space model of Phillips and Johnson. They found that there are no significant

differences in the overall results; however, more complex models obviously revealed more details about the exact stress/strain distribution. One of the main outcomes of their conclusions is that the elastic half-space model with its total simplicity is a fairly good first approximation of the real case. Another result is that instead of the maximum compressive strain, they gave the strain energy density as the best approximation to the signal of the Merkel receptors. Later on, they created an even more realistic but still linear, 3D model as well (Dandekar et al., 2003 [19]) (Figure 2.9), with more detailed analysis of the endless material properties of the skin, including the measurement of the Young-modulus of the several skin layers. They bring out no significant differences compared to the previous results but mention the possible effects of viscoelasticity and the finger ridges, without incorporating them into the finite-element simulations.
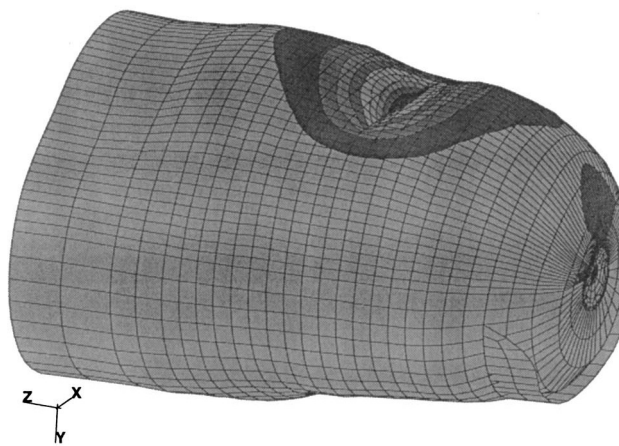
Figure 2.9. 3D finite-element model of the human fingertip indented by a sharp wedge (Dandekar et al., 2003 [19])

2.3.3. Viscoelasticity of the skin

As the skin models were developed, more and more important details could be included into them. One is the viscoelastic property of the skin, i.e. the effect of tactile after-images. Due to the material properties of the skin, after touching an object there are residual stresses in the material, disappearing only after a few seconds. Singh and Fearing (1998 [9]) and Moy et al. (1998 [10], 2000 [11]) (who all belong to the same tactile group at the M. I. T.) were the first to include this strange behavior in a skin model—they used their theory for a more appropriate design of tactile displays. Although viscoelasticity could be an important issue both in the description of the skin and the artificial covers, we will only treat it as a source of error and not include it in our model, as it implies higher complexity with relatively minor benefits.

2.3.4. The role of fingerprints

Another important feature of the skin is its raggedness, as already mentioned in section 2.2.1 discussing the location of Merkel receptors in the skin. Fingerprints appear naturally in our everyday life—often mentioned as personal identification clues—but their real evolutionary function is, in my opinion, even more intriguing. Papillary ridges or other types of surface undulations are usually present on high-resolution tactile sensory systems [such as the human's or primate's fingers (Figure 2.3), some ape's tail, the elephant's proboscis (Figure 2.10) or the nose of the star-nosed mole (Figure 2.4)]. Their function and nature is first described by Cauna (1954 [66]). He stated that the papillary ridges act as "magnifying levers" to the Meissner's corpuscles, thereby enhancing their sensitivity. Later, it was found that ridges have a dual function: frictional and tactile (Martin, 1990 [67]), namely, they prevent slippage and in the meantime serve as a mechanical amplification stage in the procedure of stress transduction in the skin.
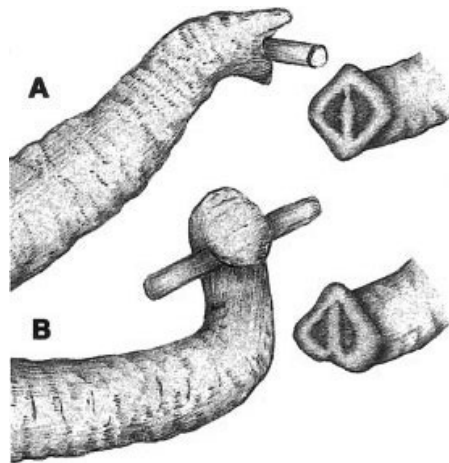
Figure 2.10. The trunk of the African (A) and Asian (B) elephant. The prehensile skill of African elephants is more refined, as they do not grasp but curl objects. Correspondingly, they have more mechanoreceptors and papillary ridges at the end of their proboscis (Hoffmann et al., 2004 [65])

From the mathematical point of view, Fearing and Hollerbach (1985 [6]) mention the possible stress-enhancing effect of a sinusoidal cover-surface first over artificial tactile sensors, and calculate the stress distribution analytically under the undulations. Maeno et al. (1998 [25]) investigate the role of fingerprints with a finite-element model of the fingertip, having different skin layers, the bone and realistic material properties included in the model. They try to use the simulation results to give an explanation for the location of the mechanoreceptors—in my opinion not very convincingly (without deep neurobiological knowledge). However, their initiative is quite courageous—later on, the

same group publishes the first artificial tactile-sensor having a ridged surface (Yamada et al., 2002 [26]), and they also create a special sensor for friction, softness and roughness detection, that emulates the function of nails, epidermal ridges, the layered structure of the skin and the different receptor sites (Mukaibo et al., 2005 [27]). Gerling and Thomas (2005 [45]) give another finite-element model of the fingertip, specializing in the effect of the fingerprints and also taking into account the ragged border of the dermis and the epidermis. They state that the ridges create a so-called "lensing effect" that concentrates the stress to the receptor sites. Later, we will not only support this property of the ridges with experimental data, but use them as a neuromorphic design element of our artificial cover.

2.3.5. The function of the hair

The last subject of our examination concerning the features of the skin is the hair. The role of the hair in the tactile system is obvious—it gives birth to a kind of tele-sensing by protruding from the surface of the skin and thus elongating the "force arm" of the receptors (Figure 2.11).
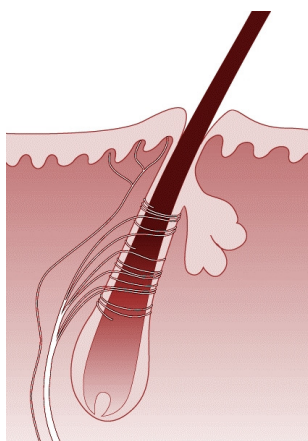
Figure 2.11. A single hair with different axons and nerve terminals around the hairshaft. The hair acts like a "mini-joystick" and converts the impact of distant forces into significant skin deformation around the receptors; image source: http://www.ilo.org/encyclopaedia

At the other end of the hairs or whiskers, inside the skin, the hair follicles are surrounded by the usual mechanoreceptors. However, they get an increased amount of input due to the enlarged skin deformation, as a consequence of the mostly shear motion of this long overhanging force arm. This structure is so efficient in sensing even the lightest distant impacts that some animals (e.g. mice and rats) rely more on this sensory arrangement then on vision. When creating artificial sensors, we can use this very idea of Mother Nature efficiently for sensitizing our structures to shear forces.

2.4. Conclusion

In the above chapter we took a thorough look at the skin and its components with the eye of an engineer. First, I introduced the different receptor types of the skin in order to see what physical properties a tactile sensor should have for an efficient functioning. Second, I showed that in tactile sensing the sensory structure itself is hardly enough for passing interpretable data on to the brain. A very important signal-processing layer in tactile sensation is the skin tissue itself, which codes the surface load on account of its pure mechanical, elastic structure. Besides this general stress-coding effect, the skin also has some special micro-features that enhance the sensitivity and efficiency of the high-resolution tactile surfaces. One of these features is the hair, which acts as a tele-sensing structure and converts the impact of distant forces into significant skin deformation around the receptors. Another feature is the ridged skin surface, which has a dual function. It increases the friction between the touched object and the skin and in the meantime concentrates the stress around the mechanoreceptors.

Later, we will use these ideas in the artificial sensor design as neuromorphic concepts. I will also support the assumptions of the anatomists and neurobiologists about the function of these elements of the skin with experimental data measured on the constructed tactile-sensor arrays. To achieve this, first of all, I give an introduction to the physics, development and characteristics of the MEMS device used in my work.

Chapter Three

TACTILE-SENSOR DESIGN

3.1. Introduction

In this chapter I introduce our artificial tactile-sensor array that is the key element of all my experimental work. First, I give a brief review about the tactile sensors available on the market nowadays, and then, as a comparison, I describe our sensor design in detail. I will go through the physical effects that are used in the sensing method, present the finite-element model of the structure with predictions to the performance of the sensor, explain some of the basics of the MEMS technology used during the technological steps and then show characterization results for the real sensors as well. Obviously, a detailed description of the experimental setup and the system-level integration of the sensors cannot be excluded either at this point. Get ready; it will be a long and multi-faceted chapter with lots of excitement!

3.2. Tactile sensors worldwide

There is a truly wide range of commercially-available tactile sensors, varying in many important parameters. Their most essential feature is the actual physical property they measure, which can be simple pressure (i.e. normal force), high-frequency vibration or three-axial forces and torques. Other fundamental parameters are the size of the structure, its element number, sensitivity, dynamic range, frequency range or its working concept. The state-of-the-art of tactile sensors is obviously found in nature—such high resolution, wide dynamic range and robustness that a biological tactile system has simultaneously is far from having been achieved yet. Just let us think about how differently we can treat a single feather and a heavy weight with the same hand, mapping the characteristic features, the texture or shape of both efficiently. Nevertheless, the artificial tactile sensors are developing also, getting closer and closer to these high requirements.

In the following we will not talk about torque and vibration sensors, since they are not truly relevant to my work. We will only consider one-axial pressure-, and three-axial force-sensor arrays, even though from the latter there are basically none on the market yet.

3.2.1. Capacitive pressure-sensor arrays

There are two basic physical effects that are used most often to measure the pressure applied to a surface. One is the change of capacitance between two pieces of metal getting closer to each other; the other is the piezoresistive effect that causes a resistivity change of a substance when mechanical stress is present inside it. Large size capacitive sensors usually consist of an arbitrary number of parallel wires attached to one side of a deformable elastic material, and the same arrangement of wires placed perpendicularly on the other side (Figure 3.1).
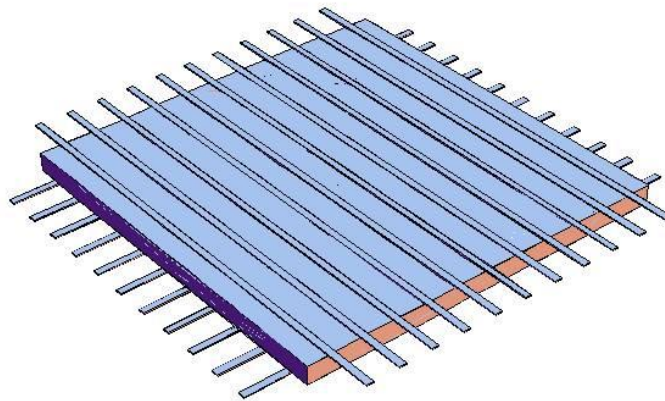
Figure 3.1. Schematic view of a capacitive tactile sensor, consisting of two perpendicular set of wires and an elastic material in between. When it is pressed, wires get closer locally and the capacitance between them changes

Each junction between these two sets represents a local capacitance between the corresponding two wires. If the array is pressed, the wires beneath the load get closer to each other and the capacitances change accordingly. The capacitance change between each two wires can be measured by the proper circuitry and sent to a computer in a serial, multiplexed way. Drawbacks of this arrangement are the nonlinear behavior and the cross-talk between the neighboring elements. Advantages are flat and flexible exterior, variable size, element number or resolution. In our lab we experimented on a commercially-available capacitive pressure-sensor toolkit, called *XSensor* (see http://www.xsensor.com). It contained pads of 9×9 and 21×21 taxels (from "touch pixels" or "tactile elements"), spaced 1.5 mm and 2.5 mm correspondingly (Figure 3.2). It measured the pressure in the range of 0−100 kPa, which lays somewhere between light touch and a very strong handshake. By now, lot more advanced arrays of this type are available, with a minimal spacing of 1 mm or less, maximal element number of around ten thousand, and dynamic range from the lightest touch up to a few MPa.

Figure 3.2. One of the four 9×9 element pads of the XSensor

The introduced capacitive principle can be used in smaller, micromachined capacitive sensors as well, where the two facing wires are represented by under-etched electrode plates. More details about these sensors will be presented soon in section 3.2.4, where the possibility of three-axial force sensing is discussed.

3.2.2. Piezoresistive strain gauges

The piezoresistive-type pressure sensors (strain gauges) are one of the first achievements of MEMS technology. They usually consist of an under-etched, suspended micro-membrane, bridge or cantilever and an embedded piezoresistor in the deformable part, at the location where the maximal stresses[2] arise (Figure 3.3). If the resistors are connected to a tiny voltage supply, the resistivity change caused by the forces acting on the suspended part can be measured easily. Basic advantages of these sensors come from the use of silicon as a structural material, with linear behavior, high sensitivity and small size; disadvantages are the rigidness and the complex technology it requires. Piezoresistive sensors usually have very good characteristics with high signal-to-noise ratio and high-frequency functioning, but they are in general sensitive to overloading and changes in the temperature. They might also have some offset caused by the residual stresses in the material due to packaging. The sensors of the MTA MFA are also based on the piezoresistive effect. They enclose four piezoresistors in one taxel, the three-axial force components are calculated from the combination of the four piezoresistive signals.

---

[2] Although strain-gauges are principally triggered by strain, as their name suggests, among engineers it is common to connect them with stress instead. The reason for this is simple. The describing physical models are mostly linear, therefore, stress and strain are easily exchangeable quantities in them; however, the characterizing equations usually have nicer form if they incorporate stress instead of strain. Since our piezoresistors are better described using stress, too, from now on, we will also use this simplification, without forgetting about the exact physical background.

More details about the piezoresistive effect and our sensors will be presented later in this chapter.
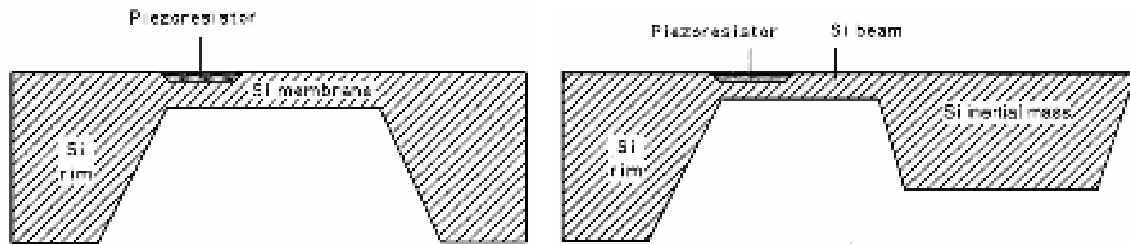
Figure 3.3. General structure of piezoresistive type pressure sensors, in which the deformable part containing the piezoresistor is either a membrane (left) or a cantilever (right) (Sze, 1994 [77])

3.2.3. Application of pressure-sensor arrays

Pressure sensors are used in a great variety of tasks. One general field is the pressure-map analysis, which is useful when designing new shoes, chairs, or investigating one's flat-feet or walking and running behavior. Pressure sensors are also used in industrial robotic applications when the precision grip and tactile feedback of a robotic arm is important. Medical applications also bring new perspectives in the application field of tactile sensors. Pressure sensors can be placed on small electrodes, endoscopes, virtual surgery gloves, etc.

In all the listed tasks shear forces are also present, but obviously not measured by pure pressure sensors. However, shear-force maps also provide valuable details about the touched surface or object, and are indispensable in slippage detection or friction estimation tasks. Therefore, many attempts have been made worldwide to efficiently measure shear forces as well.

3.2.4. Three-axial tactile arrays

A more advanced group of tactile sensors are the three-axial (or three-dimensional, three degree-of-freedom, 3-A, 3D, 3DOF, etc.)[3] arrays that measure the pressure (the normal load) at every taxel and also the two shear-force components present on their surface. Surprisingly, this very group is tiny, even though there is a definite need for 3D-force sensor arrays on the market. Single-element, 3 or even 6 degree-of-freedom (force and

---

[3] Since tactile sensors represent a relatively new field of sensing, there are no worldwide agreements on the names of their parts, groups, etc. yet. It is hard to be consistent—especially when one is citing many others—, but I will do my best.

torque) sensors have been made by many groups (Shinoda et al., 1995 [50]; Zhu and Spronck, 1992 [51]; etc.), some of them are also commercially available now (but not cheap yet). However, attempts to make three-axial sensor *arrays* are very limited in number, and the designs have not broken out of the boundaries of laboratories yet. The reason for this is quite simple: it is pretty hard to make three-axial tactile-sensor arrays. One has to use different approaches in treating the normal and the shear forces, and also has to deal with too much wiring, or alternatively, has to integrate the sensor technology with standard CMOS elements for on-chip evaluation. Therefore, all the structures aiming to produce three-dimensional tactile signals in an array end up at high complexity. Nevertheless, there are quite a few remarkable ideas to overcome these challenging obstacles.

One smart approach for measuring more than one surface-load component on an entire surface requires a huge, transparent, elastic material with lots of painted dots on it, a CCD camera below and some mathematics in between (Kamiyama et al., 2004 [52]) (Figure 3.4). If the surface is pressed, the elastic layer deforms and the dots on the CCD recording move. From this movement the three-components of the surface displacement can be calculated at discrete points with reasonable accuracy, using the continuum-mechanical equations of the elastic material. The only drawback is the large size and the need for the laboratory conditions: CCD camera, good lighting, transparent materials, etc.
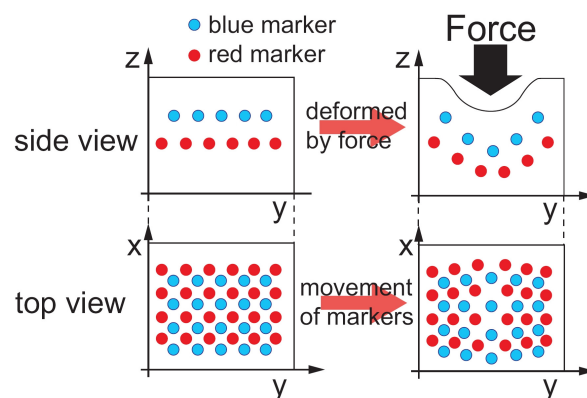
Figure 3.4. Overview of the image-based tactile sensing using a transparent elastic material painted with many dots (Kamiyama et al., 2004 [52])

Another optical approach (obviously suffering from the same drawbacks) is described by Ohka et al. (2004 [53], 2005 [54]). They use "conical feelers" instead of dots to mark the location and direction of the local displacement of a rubber (Figure 3.5). The feelers are

protruding from the bottom surface of the outermost rubber sheet and are precisely positioned so that their tip touches a flat acrylic surface below. If they are pressed against the rigid surface, the contact area between them grows. If shear forces are present, the contact area also deforms and moves. The rest of the setup is the same as before—a CCD camera records the shape of the contact areas and calculates the surface deformation from it.
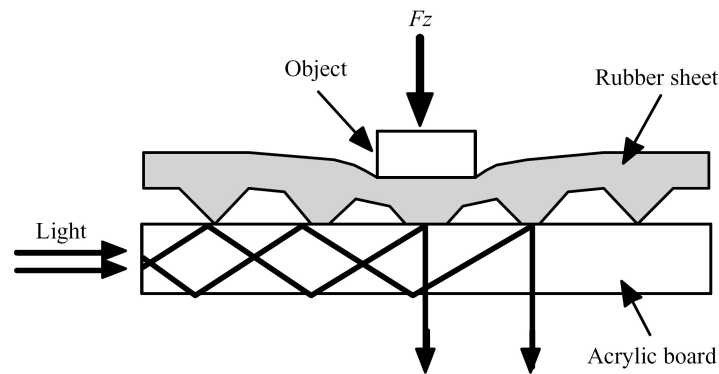
Figure 3.5. Another optical tactile sensor. When indentation is present, the conical feelers are pressed against the acrylic board. CCD camera records the size, location and shape of contact area from below (Ohka et al., 2005 [54])

Yet another optical solution is called a "fingernail sensor" (Mascaro and Asada, 2004 [55]). When the finger is pressed against an object, the blood flow in it changes, creating a colored pattern on the nail that is typical of that specific indentation type. A CCD camera records this two-dimensional pattern, and calculates the forces acting on different locations of the fingertip using trained neural-networks.

A piezoelectric approach for determining more than one force components in an array is showed by De Rossi et al. (1992 [30], 1993 [31], 1995 [32]). They use an array of synthetic polymer (PVDF) elements, where 6 polymeric crystals build up one six-degree-of-freedom taxel, measuring six components of the local stress tensor. The crystals of one taxel are arranged in a hexagonal manner. They are cut along the appropriate axis so that each of them is responding to the stress of a particular direction. Their largest published array consists of 42 sensing elements (7 taxels), but they admit that they have experimental problems of gaining data other than the normal stress. Nevertheless, this group will be mentioned later on again because of their extended theoretical work related to the mathematical description of the elastic cover of sensors, concerning the direct- and inverse-elastic problems.

Zee et al. (1997 [43]) use a conductive, silicon-based rubber layer to measure the three components of the applied force. The resistance of the rubber depends on the conductive particles in the rubber and the force applied to its surface. Their approach has two remarkable ideas that are used later by us, too. One is the method for the shear-force measurement: they estimate the shear force from the combination of four normal-force sensing taxels. The other is the exploited role of the rubber itself in the sensor design: they make cuts on the rubber surface around the sub-arrays of 2×2 taxels to separate the response of each three-axial taxel. Although they can make large three-axial arrays, the response of their sensors is highly non-linear and not accurate enough for a practical use.

Besides all these attempts, one can make use of the previously mentioned two basic pressure-sensor structures (capacitive and piezoresistive) and gain shear-load data from the combination of more than one neighboring normal force signal.

Chu et al. (1996 [56]) and Hakozaki and Shinoda (2002 [57]) use the capacitive principle to create three-axial arrays. One taxel of these sensors consist of a common conductor plate facing four capacitive electrodes, arranged tightly in a 2×2 array (Figure 3.6).
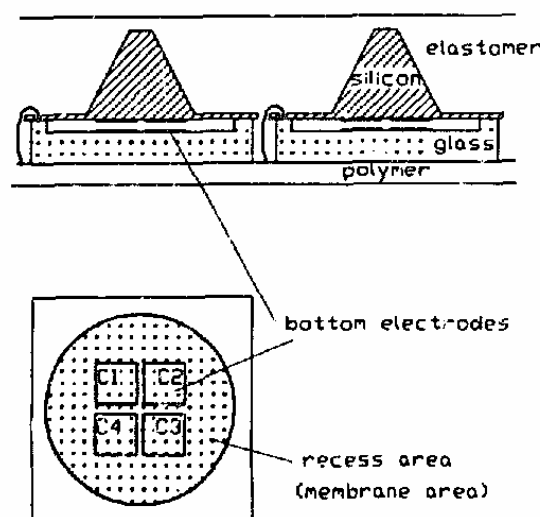
Figure 3.6. The structure of a capacitive type three-axial tactile sensor. The signal of four electrodes are combined to gain one three-axial taxel (Chu et al., 1996 [56])

In each measurement every capacitance is measured one after another. Since the capacitances are proportional to the distance of the electrodes from the plate, they are also correlated with the normal force they were pressed with. By calculating the sum and

the difference of the signal of the neighboring electrodes, one can bring out data proportional to the normal and shear forces, respectively. This idea is remarkable; the only problem here comes from the capacitive structure, which suffers from cross-talk, small signal-to-noise-ratio, small dynamic range and some nonlinearity again. Also, both authors mention large arrays of taxels but they present measurement results for only a single element.

The same basic idea is used for three-axial sensing in some silicon-type, piezoresistive MEMS devices. Here, instead of the four capacitive electrodes there are four embedded piezoresistors at the corners of a micromachined sensory structure, which consists of an etched cavity covered with either a membrane (Wang and Beebe, 2000 [58]) or four suspended bridges and a central shuttle plate (Kane et al., 1996 [59], 2000 [60]). The latter can be seen in Figure 3.7. The differences in these two structures lie mostly in the very details of the used micromachining technology.
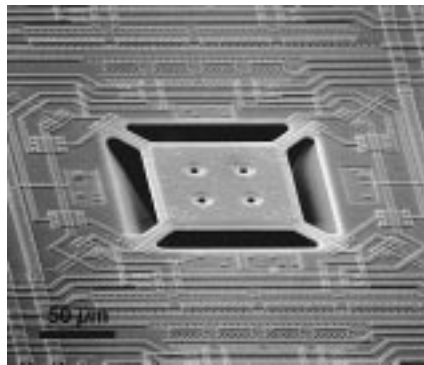
Figure 3.7. A piezoresistive three-axial tactile sensor element made by surface micromachining (Kane et al., 2000 [60])

The structure of Kane et al. (2000 [60]) is the largest three-axial array up to now, consisting of 64×64 taxels. In each one, the piezoresistors are formed of poly-crystalline silicon, embedded in deposited silicon-nitride layers. The bridges are released with front-side alkaline etching of the single-crystalline silicon underneath. Although this process is CMOS compatible, which is a crucial point in a large-array design, the structure suffers from the limited sensitivity of the poly-silicon structure and the mechanical stability of the multilayered membrane.

3.2.5. Discussion

In this section we introduced several types of one- and three-axial tactile sensors with different working principles. We saw that three-axial measurements are necessary in some dexterous manipulation tasks. From the many diverse attempts in order to make three-axial sensor arrays we can conclude that the method most generally used for shear-force measurement is based on a simple combination of the signal of four normal-force sensing elements. We can also state that one of the most severe difficulties in making large three-axial tactile arrays lays in the need for the extended wiring of the many elements, or, alternatively, the combination of the sensor technology with standard CMOS structures for on-chip evaluation. In the following we will see our novel approach for a three-axial, CMOS-compatible tactile-sensor array.

3.3. Three-axial arrays of the MTA MFA

Our approach to a three-axial tactile array also consists of suspended-bridge type piezoresistive taxels, fabricated from single-crystalline silicon (Figure 3.8). As a structural material, single-crystalline silicon provides excellent and controllable mechanical properties in all directions; moreover, its manufacturing process can be integrated into the microcircuit technology, too. The main advantage of our technological method lies in the freedom provided by the use of single-side porous silicon micromachining for the formation of the suspended n-type single-crystal bridges. This way, there is no orientation restriction in the design whatsoever; therefore, it also facilitates the formation of the optimum p+ piezoresistors.
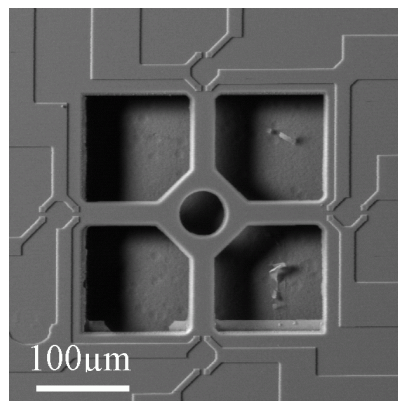
Figure 3.8. Scanning-electron micrograph of one taxel of the sensor array. Characteristic dimensions: bridge $80 \times 32 \times 10$ μm^3, plate $100 \times 100 \times 10$ μm^3, hole 50 μm diameter, cavity depth cc. 35 μm. The piezoresistors are embedded around the suspension points of the bridges

In this section I will go into some details of our sensory structure. I will present mechanical modeling results, some technological details illustrating the advantages of our design, and finally, I will show how our taxels are connected in an array.

3.3.1. Mechanical modeling

The geometry of the structure was designed first with finite-element method using the Cosmos/M 2.0 package. The aim was to find the optimum feasible sizes, the best locations for the piezoresistors and to reach the highest sensitivity without deteriorating the sensor. The working interval was defined in the force range of 0.1–10 mN.

The three-dimensional finite-element model was built using 8-noded brick elements (Figure 3.9). In the model a protrusion in the central hole of the membrane receives the load and leads to a magnification of the lateral-force components. We tested the finite-element structure with three different load cases:

- Pure normal force that is perpendicular to the plane of the membrane (F_z);
- shear force in the x direction, parallel to the suspending beams (F_x);
- shear force attacking at 45° with respect to both x and y directions (F_{xy}).
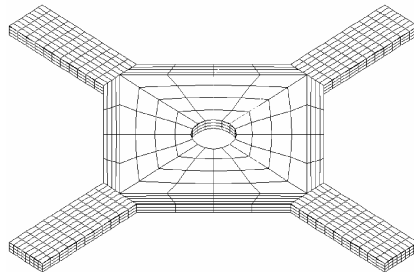
Figure 3.9. 3D meshing of the sensor, used in the finite-element calculations. We built up the model with 8-noded brick elements

The sensitivity of a p-type (110) oriented piezoresistor on a <100> chip can be calculated by the following equation (Sze, 1994 [77]):

$$\frac{\Delta R}{R} = \frac{\Delta V}{V} \cong \frac{\pi_{44}}{2}\left(\sigma_l - \sigma_t\right),$$

(3.1)

where R is the zero-stress resistance, ΔR is the resistance change when stress is present, π_{44} is the dominant piezoresistive coefficient of the material (π_{11} and π_{12} are relatively small, hence they are neglected), σ_l and σ_t are the longitudinal and transversal stress components, with respect to the current flow. We will get back to the piezoresistive effect and the piezoresistive coefficients in more detail later in this chapter, in section 3.4.1.

The stress must be as high as possible at the location of the piezoresistors, on the other hand it must never exceed the yield stress, which has a well-known value for single crystalline silicon (250 MPa). Since reliable yield stress values for silicon-nitride are hard to find, we chose the value of 250 MPa to limit the stresses in the sensor. We used the von Mises equivalent stress (3.2) to have a general estimate of the stress field:

$$\sigma_{vM} = \sqrt{\frac{1}{2}\left[\left(\sigma_1 - \sigma_2\right)^2 + \left(\sigma_2 - \sigma_3\right)^2 + \left(\sigma_3 - \sigma_1\right)^2\right]},$$

(3.2)

where σ_1, σ_2 and σ_3 are the principal stresses.

The results—calculated for a geometry shown in Figure 3.8— are listed in Table 3.I. The used materials are assumed to be homogeneous, isotropic and linearly elastic; therefore, the obtained stresses are proportional to the loads.

TABLE 3.I. CALCULATED STRESSES (MPA) AND SENSITIVITY AT THE UPPER END OF THE FORCE INTERVAL (10 MN) IN THE DIFFERENT LOAD CASES, FOR A GEOMETRY GIVEN IN FIGURE 3.8

Load	σ_{vM}	σ_l	σ_t	$\Delta R/R$
F_z	203.8	–203.5	–38.2	–0.114
F_x	293.2	290	55.6	0.162
F_{xy}	269.9	205	39.3	0.114

The stress field (σ_{vM}) for load F_z (10 mN force applied normally to the membrane) is presented in Figure 3.10. Another important result shows the x component of the general stress field in different loading cases (Figure 3.11). It is interesting to note that in the case of x directional shear loading (rightmost image on Figure 3.11), most of the stress appears in the bridges where the current is parallel with the load (there the x component of the stress is a longitudinal one). In the other two bridges, where the current and the

load are perpendicular to each other, the x directional (in this case transversal) stress is negligible. This result will enable us to neglect the transversal stresses later in the mathematical model of the sensor, thereby reducing its complexity. More detailed description about the finite-element modeling can be found in (Vízváry et al., 2003 [4]).
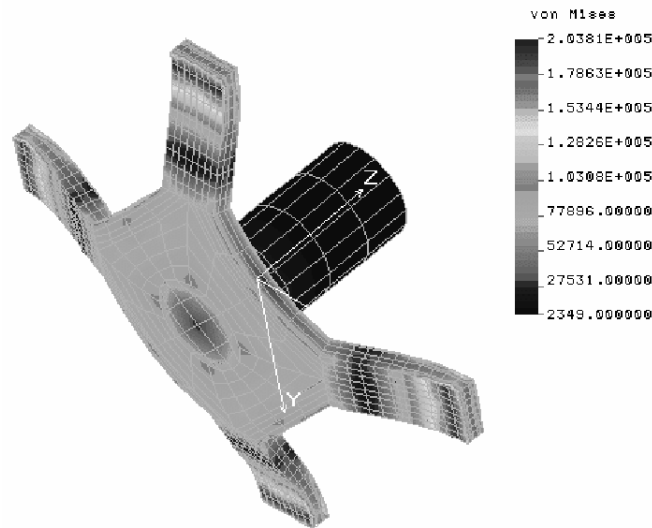
Figure 3.10. Stress field (σ_{vM}) of the sensor in response to 10 mN force applied in the z direction
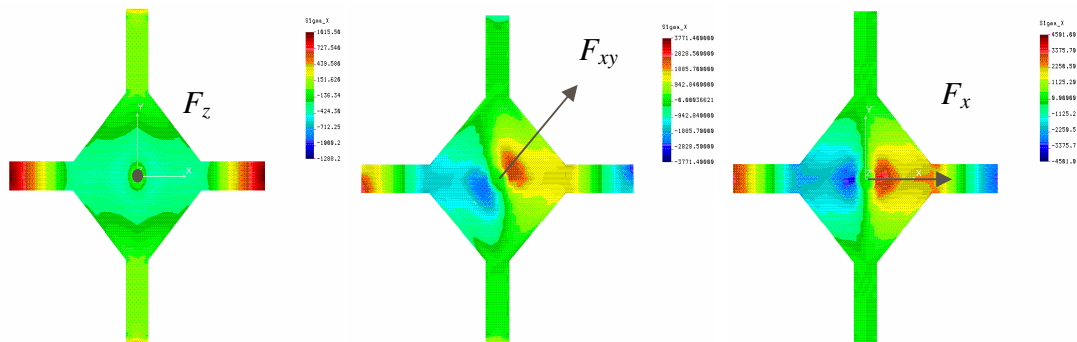
Figure 3.11. Component x of the stress field under loads of different directions. It can be seen that longitudinal stresses are much higher than transversal ones (rightmost image)

3.3.2. Wafer processing and packaging

Standard p-type 10–15 Ωcm (100) Si wafers were selectively doped with phosphorus by ion implantation. After annealing we obtained an n-type region, resulting in a total membrane thickness of 10 µm. We prepared the p+ piezoresistors in this layer by boron implantation followed by silicon-nitride masking pattern on the front side and depositing an aluminum layer on the back. Then we performed an 800 s electrochemical etching process in a galvanostatic regime, using a hydrofluoric acid and ethanol mixture at 7:3 ratio, with a current density of 60 mA/cm^2. The resulting porous layer was 34–36 µm in

thickness. In order to maintain the integrity of the suspended membranes, we dissolved the porous Si layer from the individually cut chips.

After processing, we die-bonded the chips onto a printed circuit board (PCB). We made electrical connections between the PCB and the sensor array using a standard Al wire ultrasonic technique. Then we coated the wire-bond connections and the wires with a two-component epoxy[4] to prevent mechanical damage.

3.3.3. Array assembly and system-level integration

The first generation chips were cut and bonded to a small PCB in 2×2 arrays, with 1.5 mm taxel spacing (Figure 3.12). In this arrangement the four taxels resulted in 16 individual signaling wires that is more or less the maximum one can treat with a parallel read-out circuitry.
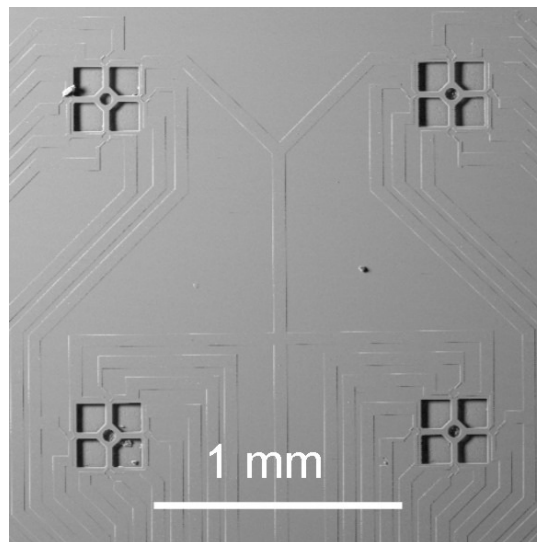
Figure 3.12. 2×2 array of taxels. Taxel spacing is 1.5 mm

At each taxel, the four piezoresistors were arranged in a half-bridge configuration with their reference pairs on the rigid substrate (Figure 3.13). This design provides a direct voltage reading proportional to the surface load. The bias voltage was 5 V in all the cases; hence, 2.5 V was each measured voltage signal in the unloaded case.

---

[4] Araldite D (Vantico Ltd.)
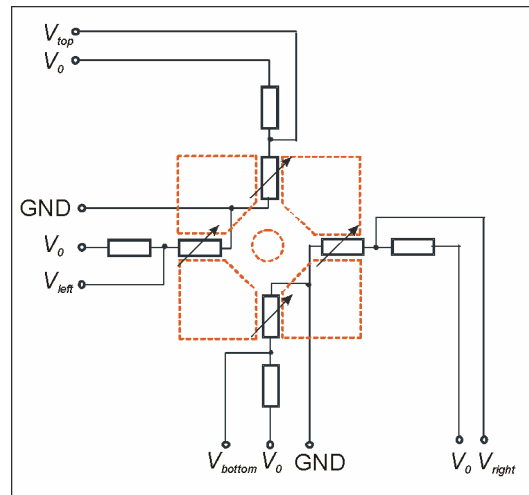
Figure 3.13. Read out circuitry of a single taxel. The four piezoresistors are connected in a half-bridge configuration with their constant reference pairs on the rigid substrate, outside the deformable area

In the first generation setup, we measured the node voltages with a Keithley 617 Programmable Electrometer across a Keithley 705 Scanner at each node. We used the LabView 6.0 package for control and data acquisition via the IEEE-488 bus. Later on, we developed a linear amplification stage with 32 parallel channels and an amplification factor of around 50–60 (Figure 3.14).
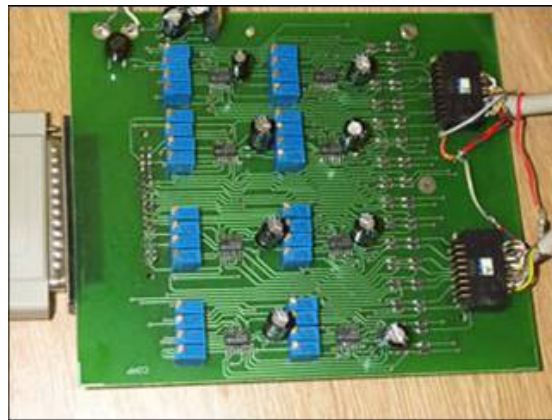
Figure 3.14. The 32-channel amplifier between the sensors and the PC

We used an Advantech PCI 1713 A/D converter card in a Pentium IV PC to achieve real-time measurement speed, necessary for high-precision experiments and further applications. Finally, we developed an evaluation software for professional data analysis (Figure 3.15).
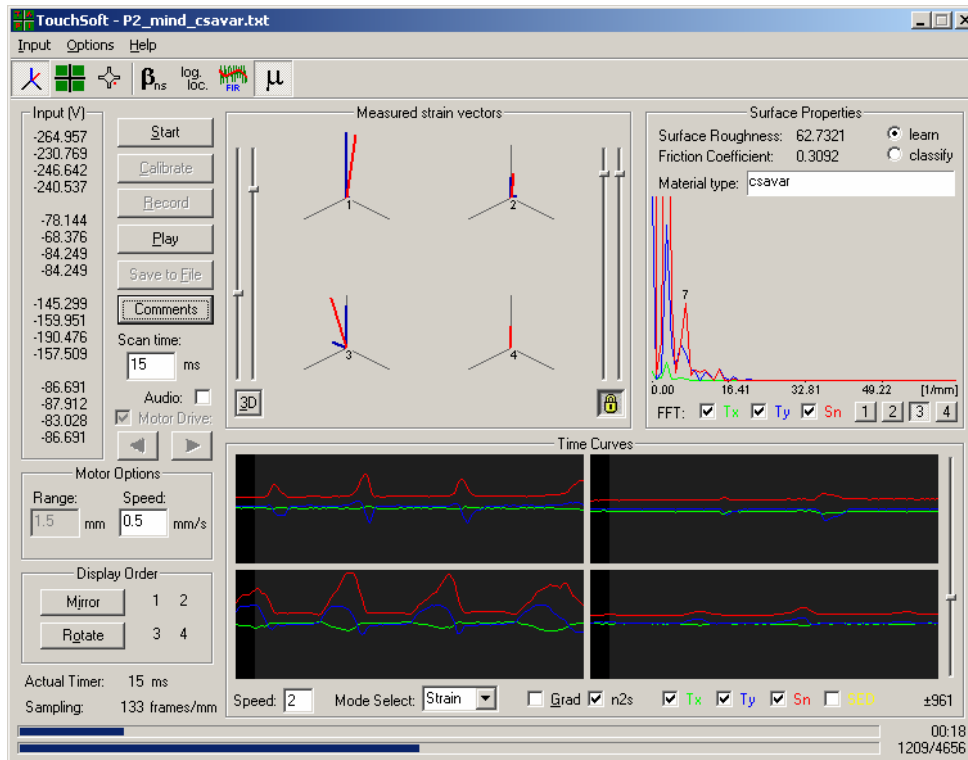
Figure 3.15. Screen shot of the software used for data analysis

3.4. Characterization of our three-axial sensors

In this section I will show the first experimental results concerning the characterization of the sensor structure. First, I will go through the physics involved in the sensing method and show the principle used for shear-data extraction. Then, I will present the experimental setup used for testing, and finally, I will show experimental characterization results and compare them with the preliminary finite-element model predictions.

3.4.1. Working principle

The physical background of the sensing procedure connecting the surface forces with the measured voltage change can be divided into the following five basic phases:

A) The forces act on the outer surface of the elastic cover, deform it, generate mechanical stress and strain inside the rubber and also at its contacting surface with the MEMS structure. The input—coded by the cover— thereby gets transferred to the solid sensory structure underneath.

B) The micro-bridges under the cover also deform, hence, generating mechanical stress/strain inside the solid silicon structure as well, hopefully with the highest values around the piezoresistors.

C) The presence of the mechanical strain in the bridge triggers the resistivity change of the piezoresistors.

D) If constant current is run through the resistors, their change can be measured in voltage change.

E) The combination of the signal of the four piezoresistors results in data that are related to the three surface-load components.

In the rest of this chapter we assume that there is no cover on the sensor yet, thus we will discuss only the points B to E in detail and assume that the input forces act on the bare sensor surface. For reference about the piezoresistive effect and the working principle of micro sensors, see (Sze, 1994 [77]).

B) Due to the very complex structure of the MEMS device we have to make basic simplifying assumptions to be able to create a descriptive model. These are the following: 1) We treat every input force as a point-like load acting on the center of the suspended structure; 2) We assume that the input forces are not too large, namely, they do not cause nonlinear changes in the structural material (due to the very good characteristics of the silicon, this is not a strict constraint at all up to the limit of overloading); 3) We assume that superposition holds for the different load components and for the stress they generate (if the size of the deformation is much smaller then the characteristic sizes of the sensor, it is a good assumption, too (Kane et al., 2000 [60]). If we stick ourselves to these constraints, the stress generated at the location of the piezoresistors can be described in the following way:

$$
\begin{aligned}
\sigma_{ln} &= \alpha_{ln} F_n, \\
\sigma_{ls} &= \alpha_{ls} F_s, \\
\sigma_{ts} &= \alpha_{ts} F_s,
\end{aligned}
\tag{3.3}
$$

where the index l denotes the longitudinal, t the transversal uniaxial stress field in a given bridge, with respect to the current flow in the corresponding piezoresistor (and so the local bridge orientation, which is parallel to it in our structure), as a result of a normal (*n*)

or shear (*s*) force (*F*) acting on the taxel. The *α* linear coefficients connect the force and the generated stress, and can be analyzed further, involving geometrical parameters and the theory of bridges and membranes. In our model their only truly important feature is the assumed linearity. Equation (3.3) shows that normal forces generate only longitudinal stress in the piezoresistors, namely, they only elongate bridges. In contrast, shear loads generate both longitudinal and transversal stresses—they also rotate some bridges a little bit around the long axis. These results are in accordance with the mechanical modeling results shown in Figure 3.11.

C) Piezoresistivity is a very interesting feature of some semiconductors: when mechanical strain is present inside them, their resistivity changes accordingly. The connection between the strain (or better the stress) and the resistivity in the most general case is the following:

$$\frac{\Delta \rho_{ij}}{\rho_{ij}} = \pi_{ijkl} \sigma_{kl} , \qquad (3.4)$$

where ρ is the local resistivity tensor, π is the fourth-order, 81-element tensor of piezoresistivity, and σ is the stress tensor. Luckily, due to the crystal symmetries, this complex connection can be simplified efficiently. In our case (p-type silicon) there are only three independent components of the piezoresistivity tensor, as will be seen in Equation (3.6). The stress tensor can also be simplified if we introduce the longitudinal and transversal components that were used in (3.3). After this (3.4) reduces to the following form:

$$\frac{\Delta R}{R} = \sigma_l \pi_l + \sigma_t \pi_t , \qquad (3.5)$$

where *R* is the total resistivity, *l* and *t* still denote transversal and longitudinal components of the stress tensor and now also those of the piezoresistivite tensor, with respect to the actual bridge orientation. The equation means that the resistivity change is basically caused by the sum of the longitudinal and transversal piezoresistive effects. With the knowledge of the actual directions of the elements in the crystal, (3.5) can be simplified further. The surface of the silicon wafer is in the <100> plane, the direction of

the piezoresistors (and the bridges) in our case is (110). Therefore, the longitudinal and transversal piezoresistive coefficients can be expressed with the concrete tensor-elements:

$$\pi_l = \frac{1}{2}\left(\pi_{11} + \pi_{12} + \pi_{44}\right),$$
$$\pi_t = \frac{1}{2}\left(\pi_{11} + \pi_{12} - \pi_{44}\right). \tag{3.6}$$

The actual piezoresistive coefficients can be determined from measurements. In our case they have the following values: $\pi_{11} = 6.6 \ Pa^{-1}$, $\pi_{12} = -1.1 \ Pa^{-1}$, $\pi_{44} = 138.1 \ Pa^{-1}$. It means that we can basically calculate with π_{44} and neglect the effect of the other two. Therefore, for p-type resistors we get:

$$\frac{\Delta R}{R} = \frac{\pi_{44}}{2}\left(\sigma_l - \sigma_t\right), \tag{3.7}$$

which has been introduced already in the mechanical modeling section as Equation (3.1).

D−E) In the following we will use the notation of Figure 3.16. The axis *z* is normal to the surface and points towards the sensor, while *x* and *y* are tangential directions, pointing from left to right and from bottom to top in a top view, respectively. The four voltages and resistivities are named according to the relative position of their bridges in a top view.
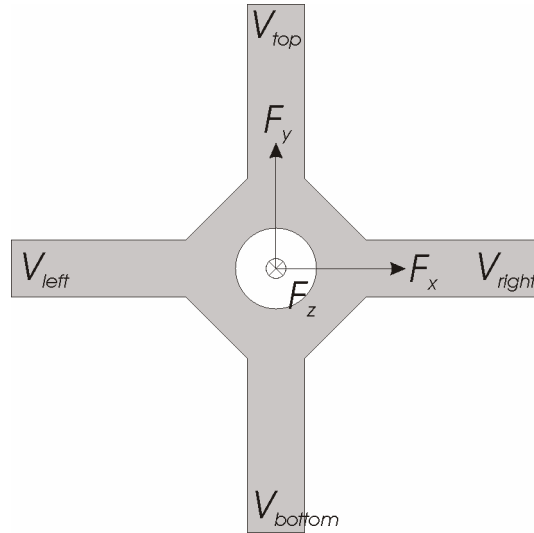
Figure 3.16. Schematic top view of the sensor structure with the used notation

Equation (3.7) shows that there is a quite simple relation between the local stress and the resistivity change of the piezoresistors. Now, all we need to do is to put (3.3) into (3.7) and sum the effect of all the possible forces:

$$\frac{\Delta R_{left}}{R_{left}} = \frac{\pi_{44}}{2}\left(F_z\alpha_{ln} - F_x\alpha_{ls} + F_y\alpha_{ts}\right), \quad \frac{\Delta R_{right}}{R_{right}} = \frac{\pi_{44}}{2}\left(F_z\alpha_{ln} + F_x\alpha_{ls} - F_y\alpha_{ts}\right),$$

$$\frac{\Delta R_{top}}{R_{top}} = \frac{\pi_{44}}{2}\left(F_z\alpha_{ln} + F_y\alpha_{ls} - F_x\alpha_{ts}\right), \quad \frac{\Delta R_{bottom}}{R_{bottom}} = \frac{\pi_{44}}{2}\left(F_z\alpha_{ln} - F_y\alpha_{ls} + F_x\alpha_{ts}\right). \tag{3.8}$$

The force components can be expressed now from the combination of the resistivity changes, if we assume that the transversal stresses are negligible, namely, $\alpha_{ts} = 0$. This is a good approximation, as already shown in Figure 3.11. For expressing the *normal force* we need to sum the four resistivity changes:

$$F_z = \frac{1}{2\alpha_{ln}\pi_{44}}\left(\frac{\Delta R_{left}}{R_{left}} + \frac{\Delta R_{right}}{R_{right}} + \frac{\Delta R_{top}}{R_{top}} + \frac{\Delta R_{bottom}}{R_{bottom}}\right). \tag{3.9}$$

To get the *shear force* components, the difference of the resistivities is needed:

$$F_x = \frac{1}{\alpha_{ls}\pi_{44}}\left(\frac{\Delta R_{right}}{R_{right}} - \frac{\Delta R_{left}}{R_{left}}\right),$$

$$F_y = \frac{1}{\alpha_{ls}\pi_{44}}\left(\frac{\Delta R_{top}}{R_{top}} - \frac{\Delta R_{bottom}}{R_{bottom}}\right). \tag{3.10}$$

Equations (3.9) and (3.10) show that the normal load only generates equal longitudinal stresses in the four bridges by elongating all of them; in the meantime, each component of the shear force shortens the bridge "in front of it" and elongates the one "behind", and also rotates the perpendicular ones but with negligible generated stress.

The task is very simple now. Assuming that all the non-loaded resistors have the same value ($R_{left} = R_{right} = R_{top} = R_{bottom} = R$), we can run direct current through the resistors and use Ohm's rule to convert the resistivity change into voltage change. Thereby, we get the final form of the equation connecting the force components and the generated voltage change:

$$F_x = \frac{1}{V_0\alpha_{ls}\pi_{44}}\left(\Delta V_{right} - \Delta V_{left}\right),$$

$$F_y = \frac{1}{V_0\alpha_{ls}\pi_{44}}\left(\Delta V_{top} - \Delta V_{bottom}\right), \tag{3.11}$$

$$F_z = \frac{1}{V_0\alpha_{ln}\pi_{44}}\frac{\left(\Delta V_{left} + \Delta V_{right} + \Delta V_{top} + \Delta V_{bottom}\right)}{2}.$$

A more practical form of the above equation is the following:

$$F_x = -\frac{1}{kV_0\alpha_{ls}\pi_{44}}T_x = -C_sT_x,$$

$$F_y = -\frac{1}{kV_0\alpha_{ls}\pi_{44}}T_y = -C_sT_y, \tag{3.12}$$

$$F_z = -\frac{1}{kV_0\alpha_{ln}\pi_{44}}S_n = -C_nS_n,$$

where k is the amplification factor of a linear amplifier connected to the output of the sensors, T_x, T_y and S_n are the amplified relative force components that are actually

measured by the PC and appear in the software, C_s and C_n are shear and normal linear coefficients, respectively, connecting the real, and the measured, relative force components. They contain all the information about the geometry, the piezoresistive coefficient, the amplification and the bias voltage. To have positive measured response on positive forces, a multiplier of −1 is also added everywhere. Our next task now is to check if this model really works.

3.4.2. Experimental setup

The data acquisition and processing system of the experimental setup has already been introduced in section 3.3.3. Here we concentrate on the details of the loading instrument and the measurement setup itself.

For examining the sensors we built a mechanical test station, where the sensors were fixed on a precision x–y table that could also be tilted. The accurate position of the table in the x–y plane could be adjusted mechanically, and later on we also installed a high-precision stepper motor along one axis (1 mm = 320 steps, with further micro-stepper circuitry, resulting in submicron step size, with a finely adjustable speed range of 0–2 mm/s). For applying load on the sensors we used several constructions, all fixed over the sensor array with an adjustable vertical position. The most sensitive one was an electromagnetic force transducer mounted on the table. Its loading tip was a tiny needle pointing towards the sensor. The exact force applied by the tip could be set by a current source. First, we characterized the tip itself with a high-precision Saltorius scale. According to the measurements, this force transducer had linear response with a sensitivity of around −20 mg/mA (Figure 3.17), and could be used for forces in the range of 0.01−3 mN.
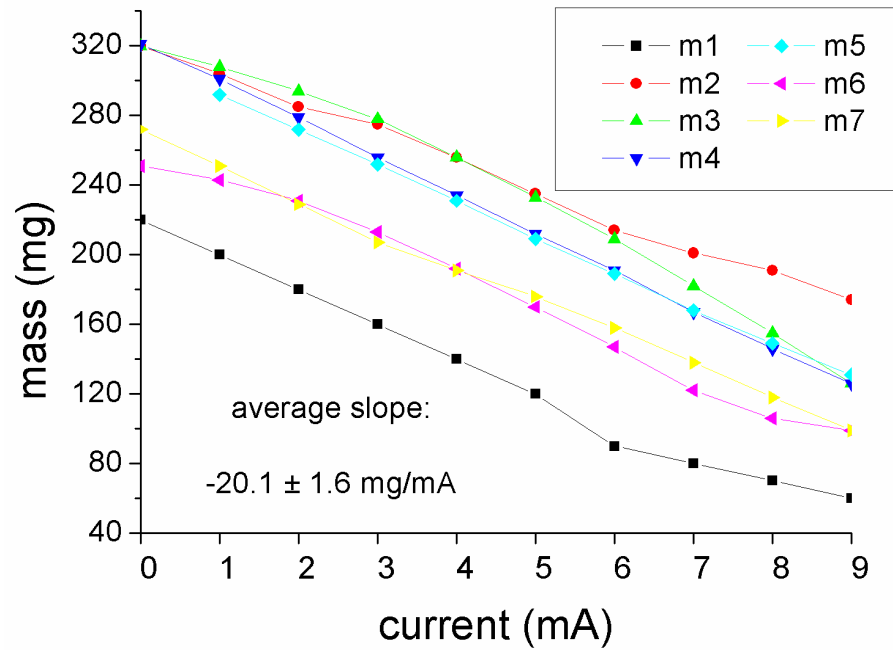
Figure 3.17. Response of the electromagnetic force transducer. Different colors represent subsequent measurements. The offset is only a result of the initial positioning and does not count. The sensitivity of the transducer is around −20 mg/mA

The second, less sensitive (and less precise) loading instrument was a mechanical one, in which different weights were put on top of the inner part of a rollerpoint pen, which could be moved freely in the vertical direction inside a tube (Figure 3.18). The weight was concentrated to the bottom tip of the inner part when it was pressed against the sensor. The force range of this transducer was 10–200 mN, which is two orders of magnitude larger than the previous one. This instrument was only used for some preliminary experiments, and I mostly describe it because of the smart and cheap idea it is based on.
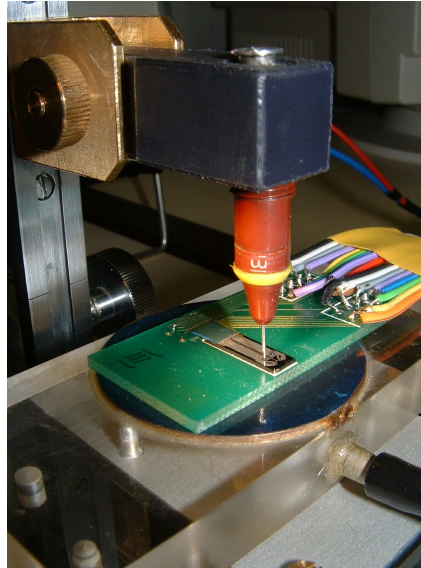
Figure 3.18. The 2×2 sensor array fixed on the measurement table with vacuum, and the first, mechanical loading instrument

The third loading instrument was a needle with a built-in strain gauge, measuring the total loading force of the loading tip. The signal of the strain gauge was calibrated and displayed in grams with a special device made for this purpose (Figure 3.19). The force range of this transducer was 0−1000 mN with an accuracy of 5 mN.
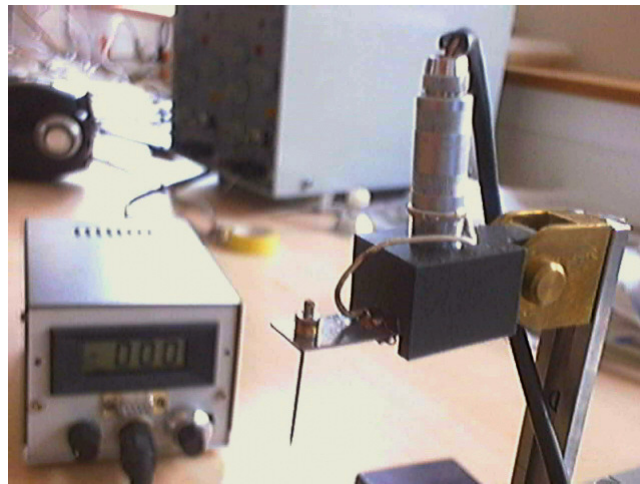
Figure 3.19. The third loading instrument with a built-in strain gauge and a digital display

The tip of all the loading instruments was more or less spherical, with a diameter of 100 μm. This size is comparable to the characteristic sizes of the sensor structure, therefore, the precise positioning of the tip was a crucial moment in the experiments, and some error due to it was generated in spite of all our attempts. To minimize the positioning error, we observed the tip and the sensor through a stereo microscope, which was also

fixed on the measurement table. The whole measurement setup can be seen in Figure 3.20.
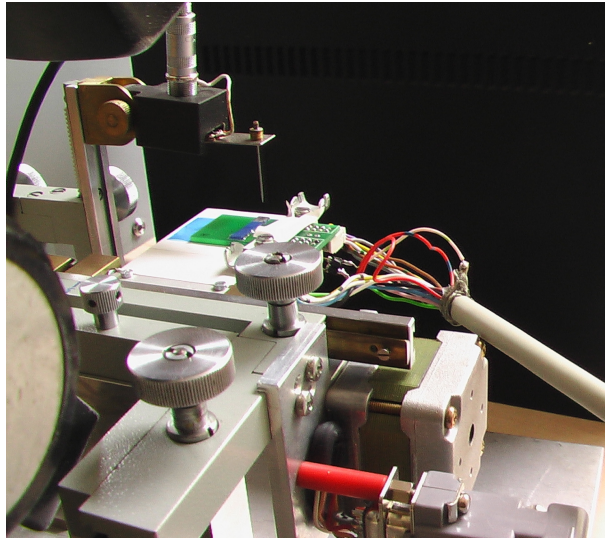
Figure 3.20. The experimental setup with the measurement table, the stepper motor, the loading needle and the fixed sensor array underneath

3.4.3. Characterization results

The first measurement results show the behavior of an unloaded sensor from the first generation, after switching the current on the four piezoresistors of one taxel (Figure 3.21).
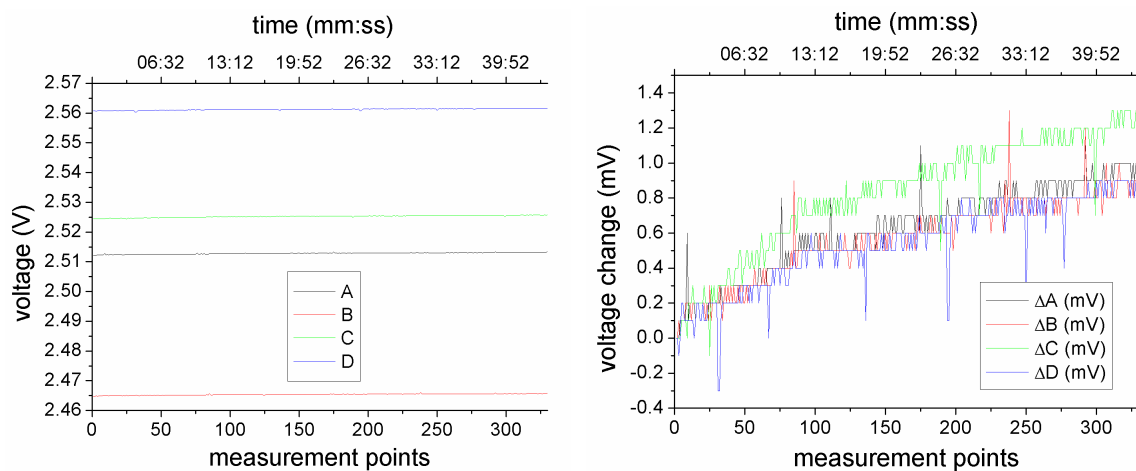
Figure 3.21. Behavior of the four piezoresistors of one taxel in the unloaded case, after switching the current on. The response is constant, with high offset and a little bit of heat transient (chip No.: ts39n1)

As can be seen, the signals have truly minimal fluctuation just over the measurement limit, resulting in a constant behavior in the unloaded case. There is quite a bit of offset in the data, which is a result of the difference between the implanted resistors. Luckily, it affects neither the sensitivity nor the linearity of the sensors, and can be compensated in

the software easily by a quick calibration. The signals also have some heat transient, which is a result of the thermally-isolated suspended structure. Unfortunately, this transient gets even larger when the sensors are covered with an elastic layer. Since the characteristics of the transient are the same for all the elements and can be measured precisely, this effect can be compensated by software, too. In practice, it is more useful to wait a quarter of an hour before working with the sensors. Alternatively, in future designs a signal of a thermometer should also be included for real time thermal compensation purposes.

The next experiments aim to measure the sensitivity of the structure by applying normal load at its center. I can tell that this is absolutely not an easy task! A minimal positioning error can result in huge changes in the response of each element, or even the destruction of the micro-bridges. However, quite promising experimental results could be achieved at the price of breaking some bridges (or shall we say, testing the limit of overloading). Measured characteristics can be seen in Figure 3.22.
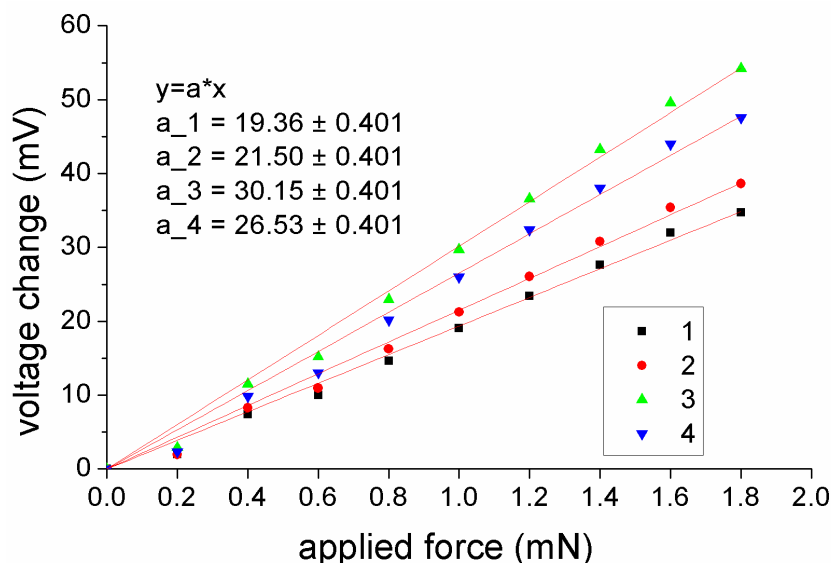
Figure 3.22. Linear response of the four piezoresistive bridges of one taxel. The difference in the slopes is mainly the result of the indefinite positioning of the loading tip (chip No.: ts39n1)

Although the response of the sensory elements is linear (as predicted by the finite-element model and the theoretical calculations, too) and has small noise in every single measurement, the uncertainty in the manual positioning of typically ±30 μm resulted in a relatively large variation of the sensitivities. Unfortunately, the rigid and undefined contact between the membrane and the needle prevented the total repeatability of the measurements. Nevertheless, the calculated sensitivity from experimental data (4–6

mV/mN/V) is close to the finite-element result for the same sensor (2.9 mV/mN/V). The sensors can be loaded with up to about 5−10 mN before they break, but if is safer to stay in the force range of 0−2 mN.

We also made some attempts to test the shear-force measuring capabilities of the pure silicon structures, but it was even harder to carry out. However, we will see in the next chapter that by putting an elastic cover over the sensor, even a pure normal load creates shear forces at the border of the sensor and the cover and thus shear measurements will be much easier to accomplish. The experiments with covers will also prove that the difference between the sensitivities of the piezoresistors is coming only from the positioning error or other inaccuracy during the measurement.

One final thing worth mentioning is that these preliminary experiments were accomplished on the first-generation sensors, at the beginning of my work. Since then, the technology has been improved in some details and the features of the sensors have become more homogeneous with less malfunctioning, resulting in even higher signal-to-noise ratio and more utility.

3.5. Conclusion

In this long and diverse chapter we got to know the sensory structure that is the basis of basically all my later important results. I showed that the MEMS devices of the MFA represent a good starting point for three-axial tactile sensing tasks, which, by itself is kind of a novelty. Our sensors have nice linear characteristics with the approximate sensitivity that was predicted by its finite-element model. The sensors are assembled in 2×2 arrays for later sophisticated tactile applications. As a short review of the introduced features, the characteristics of the sensor and the measurement conditions are summarized in Table 3.II.

TABLE 3.II. MEASUREMENT CONDITIONS AND SENSOR CHARACTERISTICS

parameter	value	comment
PC	Pentium 4	with measurement software developed by us
A/D converter	Advantech PCI 1713	in the PC
Scanning frequency	up to 60 Hz	could be enhanced even more, but higher values not needed yet
Voltage supply	5V	for the sensor chip
Taxel size	300×300 μm	with 1.5 mm spacing in the array
Array size	2×2	a new, 8×8 size design is coming soon...
Sensor sensitivity	4–6 mV/mN/V	without cover and amplification; cover reduces sensitivity by a factor between 5–30, depending on thickness
Load range	0–3 mN	maximum applicable load can be much higher if covered with an elastic layer
Loading needle diameter	100 μm	round shape, normal to the surface
Amplification factor	50–60	linear
Output range	1–1500 mV	after the amplification stage
Noise	2–3 mV	on the latest sensors, mostly from the amplifier itself

As can be seen from the results, the sensors in their pure form are practically too sensitive for a general tactile manipulation task. However, this is not a disadvantage, because as soon as we protect the sensors with a shielding elastic layer, their sensitivity also decreases apparently, and their whole characteristics change fundamentally. The topic of the next chapter will be basically this phenomenon. I will show how the elastic cover affects the performance of the sensor through its pure mechanical behavior.

Chapter Four

CONTINUUM-MECHANICS AND THE ELASTIC COVER

4.1. Introduction

In Chapter Two we already saw that the tactile signals of the somatosensory system are determined by the structure of the mechanoreceptors and, importantly, by the surrounding tissues as well. The skin is the layer that is in contact with the touched objects, and its behavior profoundly influences the overall sensation. In this chapter we will mimic this feature of our tactile system. We attach artificial elastic covers to our sensors and observe in detail how they alter the behavior of the devices.

The artificial elastic cover can be treated as the first spatial-temporal information-coding layer of the tactile-sensor structure. It converts the forces acting on its outer surface into distributed stress/strain inside the material and surface stress/strain at the bottom, which is transferred to the sensory structure underneath. Hence, the behavior of the cover is most efficiently described by the theory of elasticity in the framework of continuum-mechanics. In the following I will present the simplest model that acceptably approximates the behavior of the cover as an elastic layer. This model is used for two decades now, but only for pressure sensors. Since we have three-axial sensors, we can be the first to check the validity of the model with high spatial-resolution, three-axial measurements. Therefore, we have two main goals: first of all, to characterize our three-axial sensors again, now equipped with different elastic layers on top; secondly, to compare the theoretical model with the experimental results and check if they have anything to do with each other. To achieve that, I will also introduce some useful new parameters that describe the characteristics of the multi-component stress and strain distribution in the cover well.

4.2. The elastic half-space model

I will start this section initially with some basic issues of the theory of elasticity. First, I will introduce some fundamental physical quantities and rules that are necessary for understanding later discussions, and I will present the elastic half-space model itself with its solutions to special cases afterwards. For a very deep understanding of continuum-

mechanics and contact mechanics, see (H. Hertz, 1899, [73]), (Landau and Lifsic VII., 1974 [76]) or (K. L. Johnson, 1985 [74]).

4.2.1. Basics of the theory of elasticity

In the following we will introduce a linear theory and talk about homogeneous, isotropic solids that are deformed by external forces. The deformation of each point of the solid in general can be described by the three-component *deformation vector*:

$$u_i = x_i^{'} - x_i.$$
(4.1)

By taking derivatives of the deformation vector we can compose the symmetric *strain tensor*[5]:

$$u_{ik} = \frac{1}{2}\left(\frac{\partial u_i}{\partial x_k} + \frac{\partial u_k}{\partial x_i} \right).$$
(4.2)

The nine components of the strain tensor describe the different forms of relative deformation of infinitesimal volumes of the solid. The diagonal elements show relative elongations in the three directions, while the off-diagonal elements are related to the shear deformations. Therefore, the strain tensor is used to describe e.g. the modified distance between two points of the solid, or the local volume change (in the followings Einstein's convention holds for the double indexes):

$$dl^{'2} - dl^2 = 2u_{ik}dx_i dx_k,$$
$$dV^{'} = dV\left(1 + u_{ii}\right).$$
(4.3)

The next variable is the *stress tensor*, which describes the forces acting on a given infinitesimal volume of the solid:

---

[5] Another common notation of the strain tensor is ε_{ij}. Our notation follows the one in (Landau and Lifsic VII., 1974 [76])

$$\int F dV = \oint \sigma_{ik} dA_k,$$

$$F_i = \frac{\partial \sigma_{ik}}{\partial x_k},$$

(4.4)

where $\sigma_{ik} dA_k$ is the *i*-eth component of the force acting on the dA_k infinitesimal surface element. In the case of equilibrium, without volumetric forces, all the forces in an arbitrary volume of the body arising from the inner stresses compensate each other, namely, $F_i = 0$. The forces acting on the surface appear in the boundary conditions of the equilibrium equation.

External forces generate stress inside the material and also deform it. The connection between the stress and the deformation (strain) is determined by the properties of the material itself and described by the fourth-order *elasticity tensor*:

$$\sigma_{ij} = C_{ijkl} u_{kl}.$$

(4.5)

Our first assumptions were to treat the solid as homogeneous and isotropic. The reason for that is the complexity of the above equation. The elasticity tensor has 81 components in general, but with these two basic constraints it can be expressed with only two independent ones, hence (4.5) reduces to the following longer but much simpler form:

$$\sigma_{ij} = \frac{E}{1+\nu}\left(u_{ij} + \frac{\nu}{1-2\nu} u_{ll}\delta_{ij} \right),$$

(4.6)

where ν is the *Poisson's ratio,* which describes the compressibility of the material. It can take values between 0 and 0.5, where the latter indicates total incompressibility in volume (like rubbers). *E* is the *Young modulus*, which is related to the overall hardness of the material. The equation (4.6) is called Hooke's law.

There is only one more important parameter left that is used frequently: the *strain energy density* (SED), which is basically the local energy stored in the material when deformed:

$$SED = \frac{1}{2}\sigma_{ij}u_{ij}\,.\tag{4.7}$$

4.2.2. Postulation of the elastic half-space model

When external forces act on the surface of an elastic solid, the material gets into a deformed equilibrium state very soon. Using the definition of the strain tensor (4.2), Newton's second law (4.4), and Hooke's law (4.6), we can easily construct the equilibrium equation of isotropic bodies, expressed as the fundamental equation for the deformation vector:

$$\left(1-2\nu\right)\Delta u + graddivu = 0\,.\tag{4.8}$$

The solution of this good-looking equation is only possible in some special cases, with lots of constraints. From now on we will talk about the so-called *elastic half-space model*, which is based on the following assumptions: 1) the elastic solid is treated as a semi-infinite half-space, with coordinates *x* and *y* on the only surface and *z* pointing into the material; 2) the deformation of the solid is small enough to let us stay in the range of a linear theory; 3) far away from the indentation all stresses and deformations disappear; 4) at the beginning we take the solution of a point load at *(0, 0, 0)*, with components *(F, Q, R)*. Since superposition holds, all further solutions of extended indentation profiles can be derived from this one with integration.
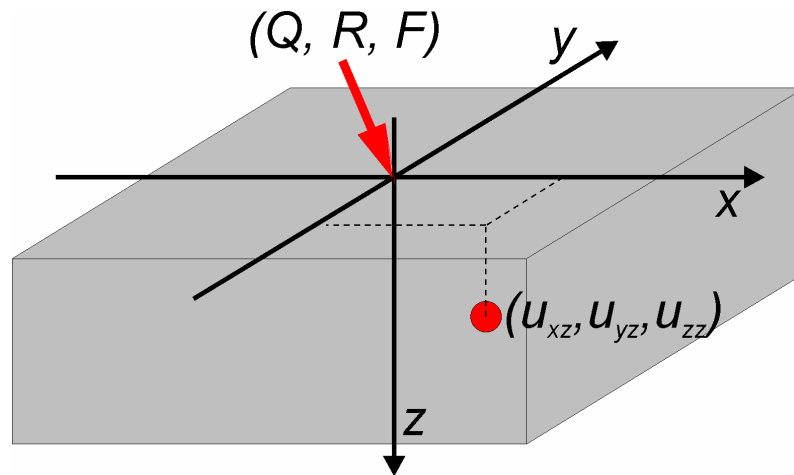
Figure 4.1. The coordinate system of the model. The point load is acting on the surface of the half space, at the point (0, 0, 0), while we are interested in the strain/stress/deformation components at an arbitrary point (x, y, z). Later, the sensor will also be imagined to the location (x, y, z), where z is the fixed rubber thickness, x and y are relative to the load. The sensor will measure three components of the strain tensor at (x,y,z), as will be shown later on

When applying the theory to the real covers, we will have one more assumption to overcome the discrepancy between the infinite model and the finite real structure. We will predict the stress and the strain arising at the bottom of the cover with the infinite model by taking values from the fixed depth of the cover thickness (Figure 4.1). Since stresses decay rapidly with space away from the surface load, this approximation is also reasonable, as will be confirmed experimentally later in this chapter.

With the above constraints Boussinesq found the first solution to (4.8) in 1885, without the slightest knowledge about the fact, that his name will be mentioned hundred years later in connection with tactile sensors. Since then, his solution has become generalized to extended indentation profiles with different shape and force distribution (Flamant, 1892 [40]; Timoshenko and Goodier, 1951 [41]; Love, 1952 [42]; etc.), still for the sake of improving the elastic theory itself.

The idea that this theory should be used to describe parts of a tactile system was first mentioned in detail by Phillips and Johnson (1981 [16]). They used the model to describe the behavior of the skin, but soon many other papers followed them with the same concept used for artificial tactile sensors. Fearing and Hollerbach (1985 [6]) and Fearing (1990 [7]) were the first of these, with detailed analysis of some previous solutions applied to elastic covers with finite thickness—all in theory, without any experimental

results. Shimojo (1994 [22], 1997 [23]) followed them with the thorough investigation of the low-pass filtering effect in the normal stress component of the point-load solution. Using finite-element simulations of the half-space model, he analyzed its characteristics as functions of the Poisson's ratio and the Young modulus. He found in addition that even a 0.2 mm thick cover has a substantial filtering effect that has to be taken into account. He was also the first to show some low spatial-resolution measurements. However, since three-axial sensors did not exist that time, his results and experiments were only applicable on simple pressure sensors. Since then, the model has been used by basically everybody in the field as a reference. However, high spatial-resolution three-axial measurements, which would really confirm the soundness of the model, have not yet been provided by any groups.

In the following we will investigate in detail the reference of further research, the point-load solution.

4.2.3. Point-load solution of the elastic half-space

The complete solution of Boussinesq is long and painstaking, and can be found in many books related to the theory of elasticity. Here we have to be satisfied with the knowledge of his assumptions (which have already been listed) and the surprising solution itself, which is presented in the following marvelous equations:

$$u_x = \frac{1+\nu}{2\pi E}\left\{\left[\frac{xz}{r^3}-\frac{(1-2\nu)x}{r(r+z)}\right]F + \frac{2(1-\nu)r+z}{r(r+z)}Q + \frac{\left[2r(\nu r+z)+z^2\right]x}{r^3(r+z)^2}(xQ+yR)\right\},$$

$$u_y = \frac{1+\nu}{2\pi E}\left\{\left[\frac{yz}{r^3}-\frac{(1-2\nu)y}{r(r+z)}\right]F + \frac{2(1-\nu)r+z}{r(r+z)}R + \frac{\left[2r(\nu r+z)+z^2\right]y}{r^3(r+z)^2}(xQ+yR)\right\},$$

(4.9)

$$u_z = \frac{1+\nu}{2\pi E}\left\{\left[\frac{2(1-\nu)}{r}+\frac{z^2}{r^3}\right]F + \left[\frac{1-2\nu}{r(r+z)}+\frac{z}{r^3}\right](xQ+yR)\right\},$$

where $r = \sqrt{x^2+y^2+z^2}$.

The solution in this very form is kind of hard to analyze. Luckily, on tactile sensors we can make a further simplifying assumption (which is used by everybody else in the literature, too). Since the cover is a rubber, its Poisson's ratio approximates the singular value of 0.5. This value causes trouble if we put it into the original equations, but in the

solution we can use it without consequences. The solution thereby reduces to the following, much trouble-free form:

$$
\begin{pmatrix} u_x \\ u_y \\ u_z \end{pmatrix} = \frac{3}{4\pi r^3 E} \begin{pmatrix} xz & r^2 + x^2 & xy \\ yz & xy & r^2 + y^2 \\ r^2 + z^2 & xz & yz \end{pmatrix} \begin{pmatrix} F \\ Q \\ R \end{pmatrix}.
\tag{4.10}
$$

The components of the other used variables can be deduced now using their definitions introduced before. For the stress tensor we get:

$$
\underline{\underline{\sigma}} = -\frac{3}{2\pi r^5} \begin{pmatrix} x^2 & xy & xz \\ xy & y^2 & yz \\ xz & yz & z^2 \end{pmatrix} (Qx + Ry + Fz).
\tag{4.11}
$$

The components of the strain tensor will be:

$$
\underline{\underline{u}} = \frac{3}{4\pi E r^5} \begin{pmatrix} r^2 - 3x^2 & -3xy & -3xz \\ -3xy & r^2 - 3y^2 & -3yz \\ -3xz & -3yz & r^2 - 3z^2 \end{pmatrix} (Qx + Ry + Fz).
\tag{4.12}
$$

And finally, for the strain energy density we get:

$$
SED = \frac{9(Qx + Ry + Fz)^2}{8E\pi^2 r^6}.
\tag{4.13}
$$

4.2.4. Characteristics of the solution

To make friends with these strange distributions generated by the simplest form of load, I carried out some simulations using *Mathematica 5.0*. From now on, for a while we will use only F, the normal load ($Q = R = 0$), with an amplitude of 1 N. Since F creates the same type of indentation in e.g. the x components, as Q does in component z [check out the symmetry of (4.11) and (4.12)], this constraint will still enable us to observe the solution in all its details.

Also, we will concentrate on the tensor elements acting on the z plane (the last row in the stress and strain tensors), since these will be the ones that create the three-component input force for the sensor structure underneath the cover. The dilemma whether we should use the stress or the strain tensor elements to describe the connection between the cover and the sensor remains open for a while; at this time, we analyze both distributions analytically and will get back to the question after the first real measurement results.

The basic shape of the solution for the three stress tensor components acting on the z plane, as a function of depth (σ_{xz}, σ_{yz} and σ_{zz}) is depicted in Figure 4.2. In the following simulations the Young modulus was assumed to be 0.87 MPa, as the hardness of one of the used real silicon rubbers. The exact value has no importance—it appears only as a linear factor in the equations.
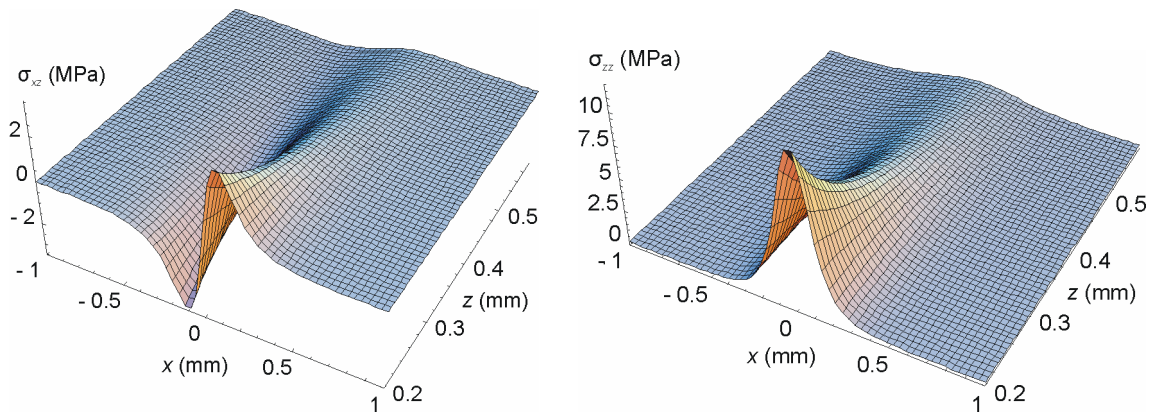
Figure 4.2. Stress distribution in the rubber, generated by a pure normal load. The two stress tensor components acting on the plane z are depicted as a function of distance from the load on the surface along the x axis, and also perpendicularly to it along z

The above distributions encompass various characteristic features that call for discussion:

- First of all, this simplest form of load has a quite complex resultant effect already. For example, the pure normal load generates normal *and* also shear stress inside the material (and obviously the shear load, too). This feature envisages the enormous difficulty of the procedure of decoding the surface load from finite measurements of stress/strain.

- Fortunately, all the stress components rapidly fade away with distance, as assumed before (Figure 4.3). This fact also signifies that the sensitivity of a sensor underneath the cover can be reduced by thickening the cover. An inversely proportional linear factor that also contributes to the amplitude of the strain and

deformation at a given location is the Young modulus. Thus, with softer materials we can gain back some of the sensitivity on thicker shielding layers, too.
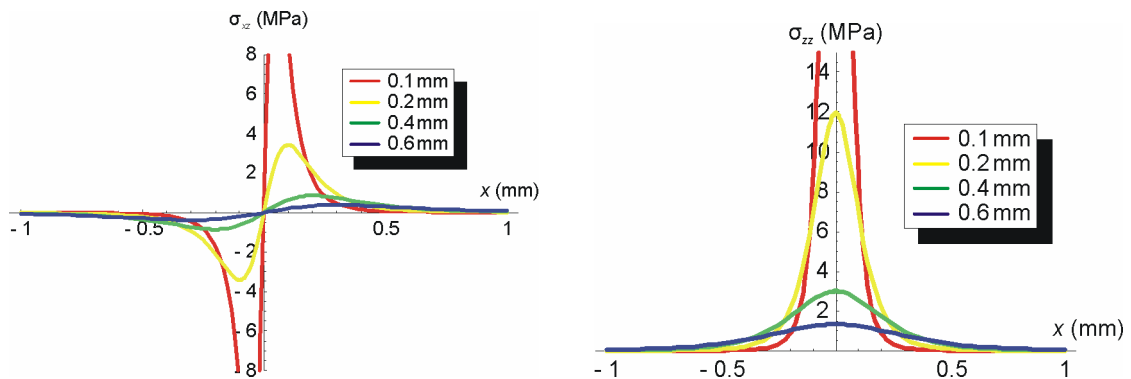
Figure 4.3. Two components of the stress tensor along the x axis, as a function of depth (z). As we go deeper into the material, the stresses rapidly fade away and distributions also widen a bit

- The shape of the distribution at constant depth also widens with z, thereby producing the low-pass filtering effect described by Shimojo (1997 [23]) (Figure 4.4).
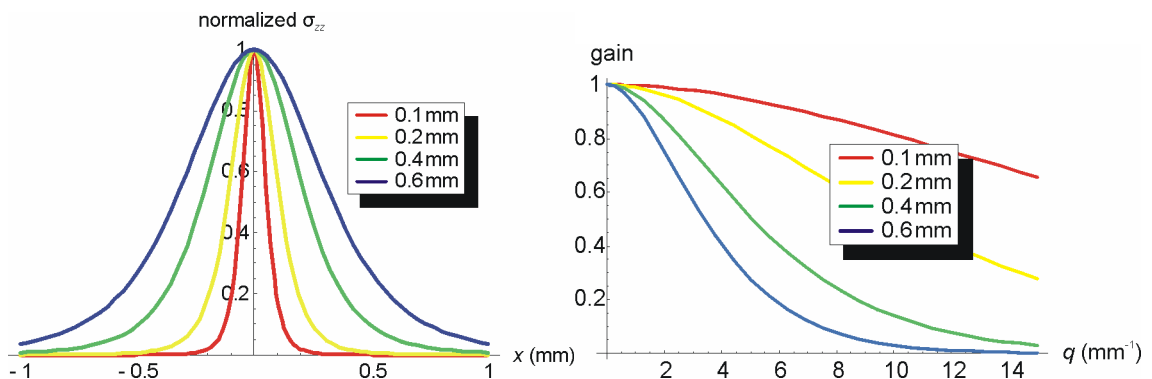
Figure 4.4. The normal stress component widens with depth. On the left image normalized distributions can be seen, while the right one shows normalized Fourier components. As can be seen, the transfer function of the cover highly reduces with depth, thereby producing a low-pass filtering effect in the normal stress component

In the following we will reflect on the stress/strain/deformation/SED distributions at a constant depth of 0.2 mm, where the sensors are assumed to be located later. As a result, we can take a simulated look at what the sensors might measure under the cover. The first figure represents the three strain tensor components acting on the z plane, around the point load at a depth of 0.2 mm (Figure 4.5). Later, we will see that the signal of our three-axial sensors will approximate these components the most.
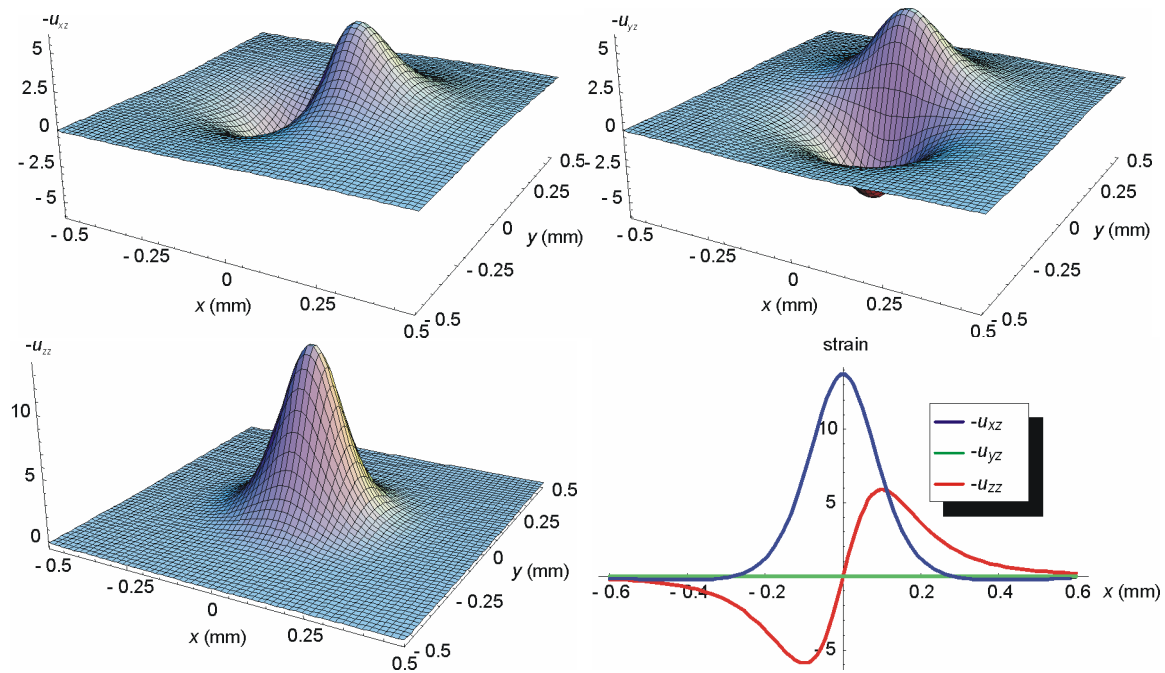
Figure 4.5. Three strain tensor components around the point load, at a depth of 0.2 mm. Bottom right image is a cross section at y = 0 with all three components

As can be seen from these images, using an elastic cover, the sensors will gain an extended receptive field, with highly nonlinear sensitivity within its borders. In other words, if the rubber is pressed even by the simplest, normal point load somewhere above the sensor, its three measured components will be highly dependent on the accurate position of the load. Let alone any other, more general case, when the indentation is far from a constant normal point load. Nonetheless, right now we do not bother about the horrifying consequences this issue brings into view, when one wants to decode the surface indentation profile from the measured signals. This topic deserves a separate chapter, which will be presented right after this one. Now, our only task is to get used to the fact that the cover kind of messes up our nice linear behavior; we need to characterize the sensors again and find out which physical quantities approximate their new signals best. Therefore, our last image about the point load will be the comparison of the shape of the different candidates in question (Figure 4.6).
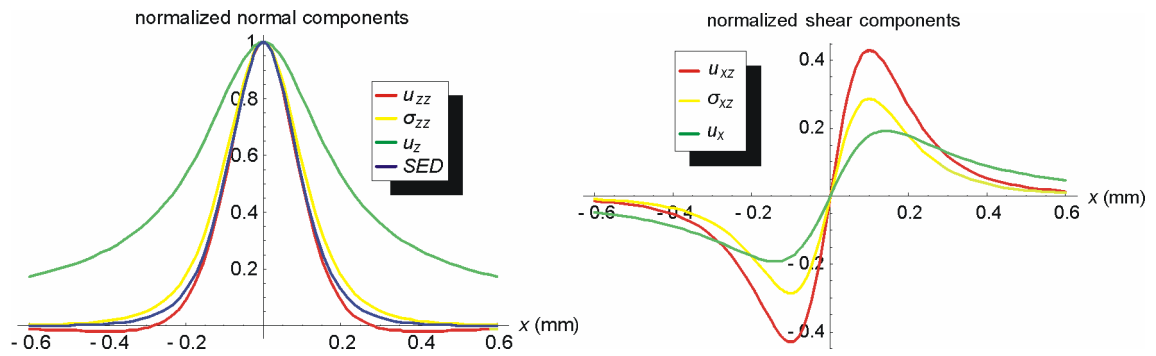
Figure 4.6. Comparison of the deformation vector, the stress and strain tensor components and the strain energy density. In the right figure the shear amplitudes are relative to the corresponding normalized normal component

At this time, we only need to keep these shapes in mind for a later comparison, when we will have the characterizing measurements on the real sensors. Nevertheless, one feature of the normal strain tensor distribution as a receptive field calls for discussion: it infers a so-called *surround inhibition* property, which is the neurobiologist's name for the Mexican hat[6]-like shape, i.e. the reduced or negative values around the positive center. Surround inhibition is also present in e.g. the strain energy distribution when a series of point loads or edges are indenting the elastic surface close to each other. In this case, the overall effect will be less strong than the local effect of a single edge alone. This is, for example, one property of the strain energy density, why Srinivasan and Dandekar (1996 [18]) voted on this quantity as the best approximation of the Merkel-cell response (Figure 2.8), as discussed already in section 2.3.2. Other properties of the stress and strain fields can be revealed only by extended indentation profiles, which are presented in the next subsection.

4.2.5. Solutions to more general indentation profiles

Once we are familiar with the basic point load solution, we can use this one to superpose any solution for extended indentation profiles. This can still be done analytically for a series of special cases (like constant pressure over an area, or constant indentation depth on a circular region, etc.), but in a general case it requires lots of numerical integrations and computer power. We will not go into mathematical details now, only depict some solutions that are, in my opinion, important to see. For those, who are deeply interested, I

---

[6] The real Mexican hat distribution is the second derivative of the Gaussian function. In its simplest form it is as follows: $(1-r^2)\exp\{-r^2/2\}$.

can suggest studying the book of K. L. Johnson (1985 [74]), where all solutions can be found in detail.

The normal stress field created by many different indentation profiles can be seen in Figure 4.7.

Point load   *Uniform deformation*

Uniform pressure   *Circular deformation*
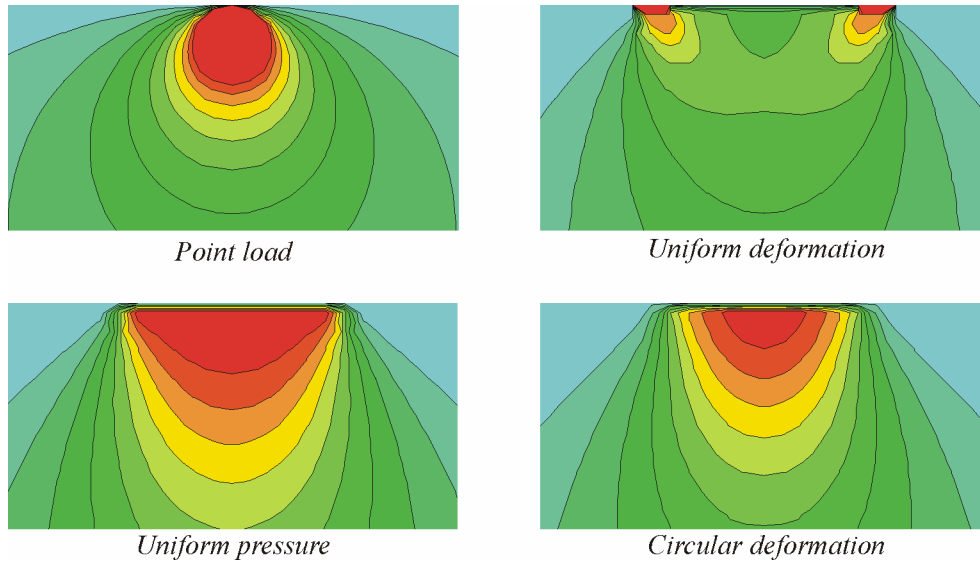
Figure 4.7. Contour plots of the generated normal stress field of a point load, and three different extended indentation profiles integrated from a line load solution. Note that the stress is concentrated around the edges of the indenting object in the top-right image

One important feature of the stress field generated by any indentation with edges is its *edge-enhancing* behavior near the surface. In the visual system, edge-enhancement (and the previously mentioned surround inhibition, too) is created by the receptive field arrangements and the structure of the neuronal system. Here, these are the outcomes of the pure mechanical properties of the elastic cover itself. Also note that if we go deeper into the material, the local effects decay and the stress field gets smoother, similarly to e.g. propagating surface waves on water. In the biological tactile systems, these features are used by the selective localization of the sensor types. The receptors that lie in the superficial layers of the skin are denser, more sensitive to edges[7] and local features with high spatial resolution, while the ones in the deep subcutaneous tissue are rarer and have an averaged response with a larger receptive field.

---

[7] The reader can try the edge-enhancing effect on his/her own finger by pressing a rigid and flat small object against it and carefully observing the characteristics of the sensation.

After being familiarized with the effects an elastic cover might bring about, our next task is to see how the characteristics of the real sensors change by attaching different elastic layers onto them.

4.3. Characterization of sensors with flat elastic covers

In this section we will check whether the previously introduced elastic half-space model really describes the behavior of the artificial covers well. We will equip our three-axial sensors with covers made of silicon rubber and measure their characteristics and simplest receptive-field properties using a point load indentation.

4.3.1. Cover molding and sensor assembly

Many different materials, even multilayered structures were investigated as possible candidates for the elastic cover. The final choice was not an easy one, because there are several crucial aspects that had to be taken into account at once. The most important features of interest are the following:

- The material's mechanical behavior must be as homogeneous and isotropic as possible. Its response should be linearly dependent on the load amplitude;
- The cover must have well-defined material properties (e.g. hardness);
- Its surface should be smooth, with small friction and no stick, in the meantime it must be highly adhesive on the other side to be able to fix it to the sensor surface reliably;
- It must be durable, robust, long-lasting, must not deteriorate when deformed (with high tensile strength);
- It should be transparent for easy handling and positioning;
- It must be in a viscous state before molding, with no air bubbles inside;
- After loading it should have minimal residual stresses or viscoelastic behavior;
- It must show no temperature dependence and preferably no thermal insulation.

The final choice was a commercially-available silicon rubber[8], with a Young modulus of approximately 2.4 MPa, calculated from its Shore A hardness of 45. This material fulfills

---

[8] Elastosil® RT-601 (Wacker-Chemie GmbH)

all the listed requirements, except for the last two. The viscoelasticity can be a huge problem in some applications and nothing really can be done against it. However, if the indentations are not too large in general, this effect does not cause a noticeable error. The thermal insulation property of the silicon rubber cannot be avoided either, since they are designed originally for this purpose. The sensory structure itself had some temperature dependence in its offset—this effect will be enlarged now even more, as the produced heat is insulated under the cover. As mentioned before, the simplest solution to this problem is a 10 minute coffee break between the switch on and the measurements.

There are two options for attaching a cover to the sensor. If the material itself is a kind of silicon glue, it must be poured on the sensor first and cured right at its final place. One big problem with this solution is the relatively large volume change silicon glues go through during curing, since it can pull the sensitive structure and create "a priori" stress inside it even in the unloaded case (in an extreme case the structure can even break). Therefore, we rather molded the cover separately, using the above-mentioned simple silicon rubber, and glued the prepared cover to the sensor with a very thin pre-cured layer of the same material around the sensitive area and also below the bridges. Some stronger silicon glue[9] was also used at the outer regions around the chip for better adhesion (Figure 4.8). The used silicon rubber does not go through a big volume change when drying, and adheres fairly to the silicon substrate. This procedure also facilitates the precise a priori design of the cover.
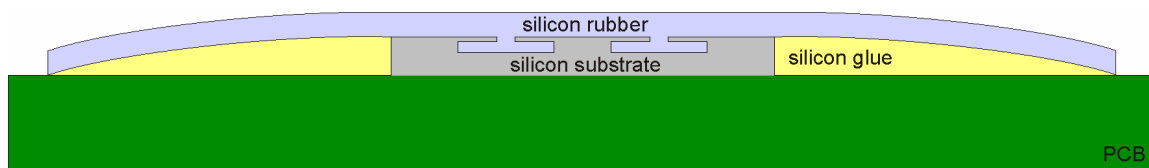
Figure 4.8. Schematic side view of the 2×2 sensor-array structure with the silicon rubber on top

The thickness of the cover can be set in the molding phase. The viscous, bubble-free silicon rubber is poured on a clean and smooth glass, and a second glass is placed on top, with spacers in between them. The height of the spacer determines the final thickness of the cover. When dried, the rubber layer can be detached from the glass and cut in pieces

---

[9] Elastosil® N10 or N199 (Wacker-Chemie GmbH)

as required. The practical minimum of the cover thickness is 0.2 mm. Under that the layer gets quite delicate and its handling calls for too much dexterity. Also, the infinite theoretical approximation gets kind of weak in that case. The maximal cover thickness is not determined; however, above 1 mm the layer gets so thick that the sensor will hardly feel anything unless it is deformed way too hard to have linear response. In general, the range of 0.2–0.5 mm is practical to use for achieving the best performance on our sensors.

4.3.2. Measurement results with flat covers

Again, the first experimental result shows the unloaded characteristics of the sensory elements after switching them on (Figure 4.9). Compared to the uncovered case (Figure 3.21), the time of the transient has not changed significantly but its amplitude (without amplification) has grown from around 1 mV to 10 mV, which is quite a large increase. The reason for this is the good thermal insulation of the silicon rubber, as discussed earlier. Once we want to have a commercial product, we need to integrate a thermometer into the design for on-chip (or "in-software") thermal compensation. Under laboratory conditions the preliminary transient is not an obstacle to further experiments.
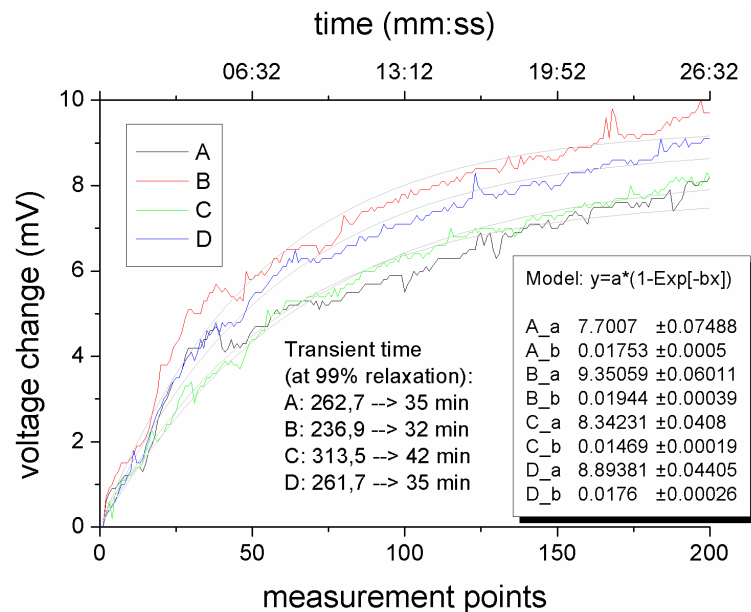
Figure 4.9. Switch transient of the four piezoresistors of one sensor under the elastic cover

(chip No.: 29)

The goal of our first real experiment was to check whether the response vs. load amplitude remains linear in the covered case. We used a simple normal load positioned above the center of the bridges, and tested two sensor chips with elastic covers of

different thickness. The load was applied through a Ø 100 µm needle with forces in the range of 0–70 mN. The first sensor was covered with a 220 µm silicon rubber, which, in general, substantially decreased the sensor's original sensitivity, but did not change its linear characteristics. The second sensor was covered with a thicker, 500 µm rubber layer. This cover reduced the sensor's sensitivity even more—by around a factor of 30. With the reduced sensitivity, higher force values had to be used for getting nice signals; hence, the force concentrated on the small region of the needle tip resulted in a non-linear behavior of the rubber, creating an overall higher order, exponential-like response (Figure 4.10).
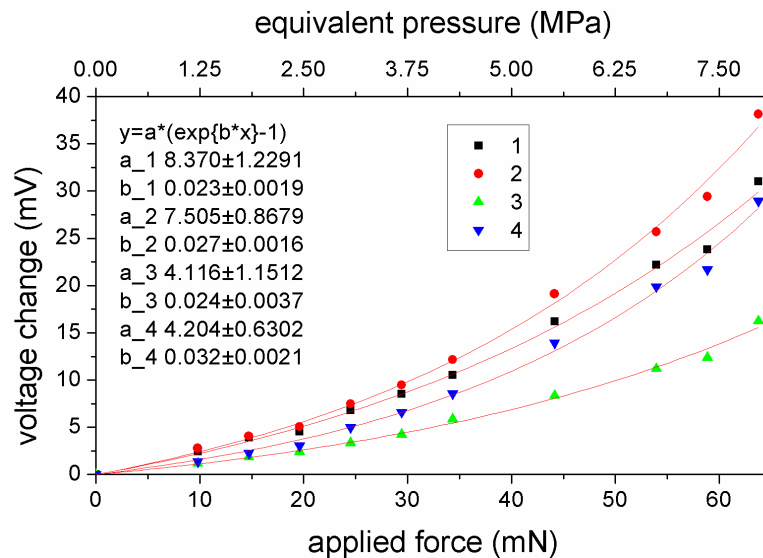
Figure 4.10. Exponential-like response of the four bridges (denoted as 1, 2, 3, 4) of one sensory element, covered with a thick rubber (500 µm). The high local pressure causes the non-linear behavior of the rubber (chip No.: 29)

In further experiments with point loads I used either small loads (up to only about 3 g, i.e. 30 mN) or thinner rubber layers (around 200 µm in thickness) to be able to test the sensors with small deformations on the rubber surface, thus staying in the range of linear behavior.

As described in detail in the first section of this chapter, due to the stress transduction in the rubber, the covered sensors should react to loads applied not only to the center of the bridges but also around it or even outside the sensor area. The following results are about the shape and distribution of this extended receptive field of one taxel, under a constant normal load. In the first experiment we combined results from unique measurements over the sensitive area to create an image of the two dimensional receptive fields of the four

sensor elements of one taxel (Figure 4.11). Three-axial components are not calculated yet. The highest achieved spatial resolution of this type of positioning was 75 ± 20 μm in both spatial directions, therefore generating relatively low precision data.
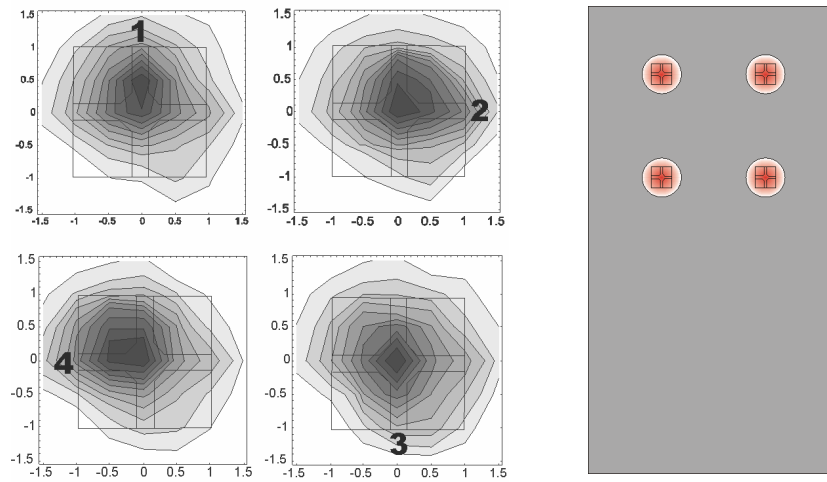
Figure 4.11. The receptive field of the four indicated bridges of a single taxel (left); size and position of the receptive fields of four taxels in the 2×2 tactile array (right). Rubber thickness is 500 μm. The darker areas represent higher response. (chip No.: 29)

In the above arrangement the taxel size is 300×300 μm^2, which corresponds to a sensitive area of around 500×500 μm^2. Since the spacing of the sensors in the test structure is 1.5 mm, we can provide overlapping receptive fields either by modifying the sensor coverage (i.e. changing the thickness and hardness of the rubber), or by increasing the resolution of the taxels in a close-packaged new design.

In order to gain information about the high-resolution shape of the receptive field, we saved the output of the sensor in real time (at a maximum of 60 Hz), and used the stepper-motor to move the loading tip slowly across one axis at a known constant speed. After each scan we finely increased the position of the tip along the other axis to cover the whole receptive field with the load in close parallel lines. Results from the *x* axis of a sensor with 180 μm rubber on top can be seen in Figure 4.12.
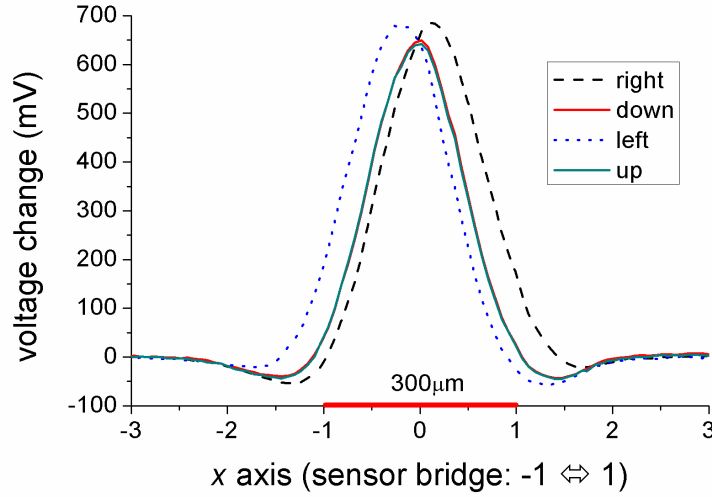
*Figure 4.12. The 1D receptive field of a single taxel across the axis of one sensor bridge in the "left"-
"right" direction. The four curves indicate the amplified signal of the four piezoresistors. The "down" and
"up" elements show perfect overlapping, as it is predicted by symmetry. Rubber thickness was 180 μm.
For a better view, all signals are multiplied by −1 (chip No.: D)*

To better catch the meaning of these curves, we have to get back to the working principle
of the sensory element and convert the four signals to the three-axial load components.
However, as the sensor is covered now with an elastic layer, the forces acting on the
center of the taxel will not be surface forces any more, but will correspond somehow to
the stress/strain/deformation state of the bottom surface of the cover. For the time being,
we assume that (3.12) can be supplemented with pure linear constants to have signals
relative to one of these listed quantities. Our new working equation thus develops into
the following final form:

$$
\begin{aligned}
\gamma_x &= \alpha_s T_x = -\alpha_s \left(\Delta V_{right} - \Delta V_{left} \right), \\
\gamma_y &= \alpha_s T_y = -\alpha_s \left(\Delta V_{up} - \Delta V_{down} \right), \\
\varepsilon_z &= \alpha_n S_n = -\alpha_n \frac{\left(\Delta V_{left} + \Delta V_{right} + \Delta V_{down} + \Delta V_{up} \right)}{2},
\end{aligned}
\tag{4.14}
$$

where γ_x, γ_y and ε_z are the three components of a physical quantity which is not known
yet, but will be revealed soon; ΔV_i ($i = top,\ bottom,\ right,\ left$) represents now the
measured, *amplified* voltage change; the α linear constants (shear and normal) are similar
to C_s and C_n in (3.12), but they are supplemented now to describe the force transmitting
connection between the solid silicon surface and the attached rubber.

Kane et al. (1996 [59], 2000 [60]) assume that the three new measured signals are relative to the three local *stress tensor* components in the rubber, acting on the *z* plane. However, if we convert the four signals of Figure 4.12 into our three new components using (4.14), we can soon make certain that the three-axial components resemble the *strain tensor* components much more[10]. Results can be seen in Figure 4.13.
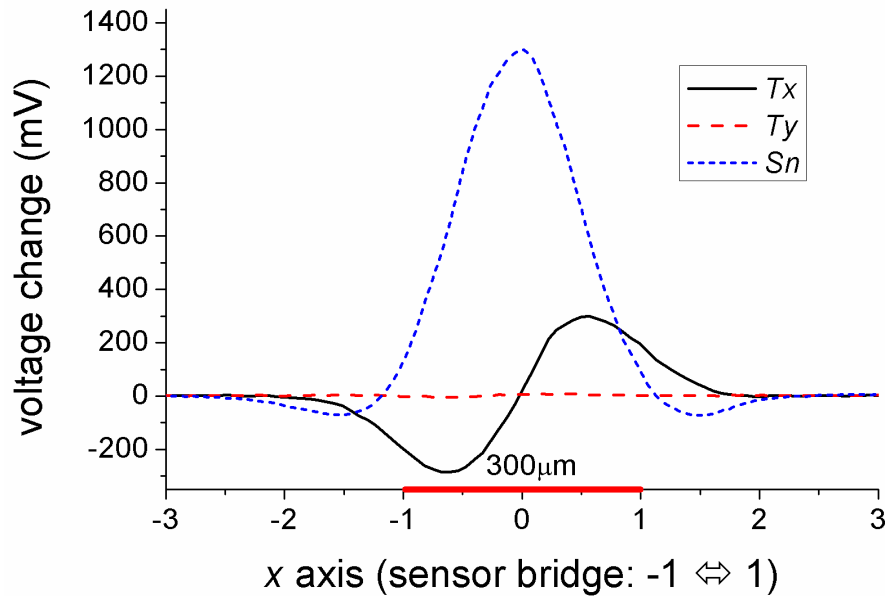
Figure 4.13. Reconstructed, relative strain components under the elastic cover, along one sensor bridge. Taxel size and position are marked on the x axis (chip No.: D)

One evident proof that excludes both the deformation vector and the stress tensor as a candidate for the measured quantity is the definite negative range in the Mexican hat-like distribution of the normal component. For a first comparison with the theoretical strain distribution (Figure 4.5), the measured two-dimensional, three-axial receptive fields are presented below (Figure 4.14). The feasibility of the approximation with the strain tensor components is investigated in the next subsection; however, from now on we assume that the strain tensor components acting on the *z* plane will be the ones that are relative to the sensor's signal, namely:

$$-\begin{pmatrix} u_{xz} \\ u_{yz} \\ u_{zz} \end{pmatrix} = \begin{pmatrix} \alpha_s \\ \alpha_s \\ \alpha_n \end{pmatrix} \circ \begin{pmatrix} T_x \\ T_y \\ S_n \end{pmatrix}. \tag{4.15}$$

---

[10] [Kane et. al, 2000] would have known this too, if they had had high spatial resolution experiments. Without spatial details the stress and strain distributions are quite similar.
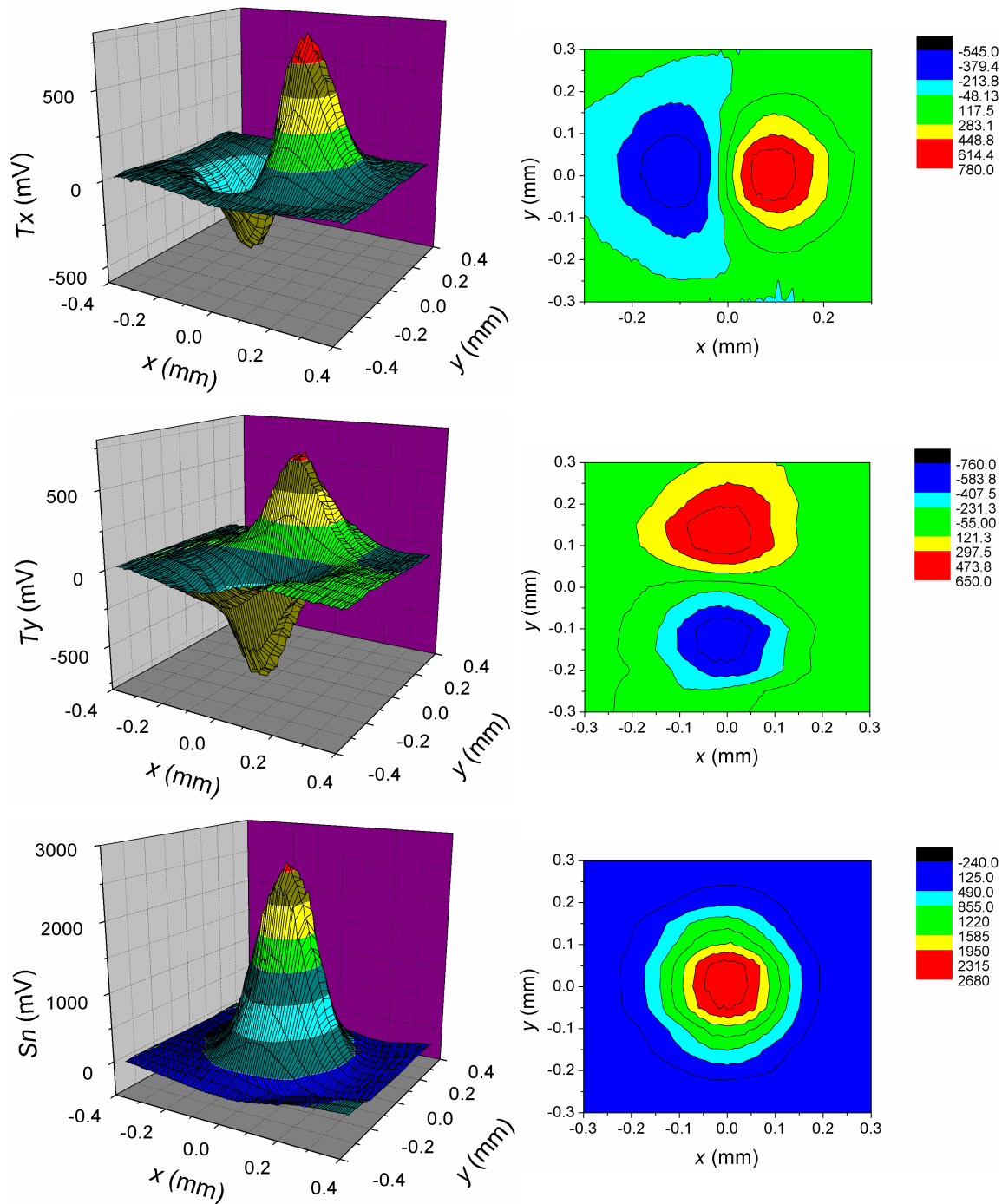
Figure 4.14. Two dimensional, three-axial measured response of a taxel under a constant normal load (and also under an elastic cover, with a thickness of 200 μm). Three dimensional graphs (left) and contour plots (right) can be seen (chip No.: P3)

4.3.3. Comparison between theory and measurements

In order to characterize the sensor's modified behavior and in the meantime check the feasibility of the semi-infinite model, I deduced some new parameters from the half-space solution and used them to estimate the similarity between the theoretical strain

distribution and the presented measurement results. I used the last row of equation (4.12) as a reference for the strain-tensor components in question:

$$\begin{pmatrix} u_{xz} \\ u_{yz} \\ u_{zz} \end{pmatrix} = \frac{3(Qx+Ry+Fz)}{4\pi E \left(x^2+y^2+z^2\right)^{5/2}} \begin{pmatrix} -3xz \\ -3yz \\ x^2+y^2-2z^2 \end{pmatrix}. \tag{4.16}$$

In the first run I analyzed the normal strain (u_{zz}) distribution, and calculated the followings from the above equation, using only normal force in accordance with the experimental testing:

- $-u_{zz} = max,$ where $x = 0$;
- $-u_{zz} = min,$ where $|x| = 2z$;
- $u_{zz} = 0,$ where $|x| = \sqrt{2}z$;
- $|(-u_{zz})_{max}/(-u_{zz})_{min}| = 5^{5/2} \approx 56.$

$$\tag{4.17}$$

In the measurement shown in Figure 4.13 $|(-u_{zz})_{max}/(-u_{zz})_{min}| \approx 19$, which indicates a much stronger lateral-inhibition effect than predicted. This is probably the result of the finite cover thickness, contrary to the infinite model.

There are two more easily measurable parameters that can be extracted from (4.16), which characterize the *width* and *amplitude* of the normal strain distribution as a function of rubber thickness:

$$W = 2\sqrt{2}z,$$
$$A = \frac{3F}{2\pi E}\frac{1}{z^2}, \tag{4.18}$$

where W is defined as the length between the two intersections of the normal strain curve and the x axis, A is defined as the absolute maximum value of the u_{zz} curve at $x = y = 0$. To measure these parameters on the real sensors, I attached elastic layers of different thickness onto the same sensor, and compared the modified strain profiles (Figure 4.15).
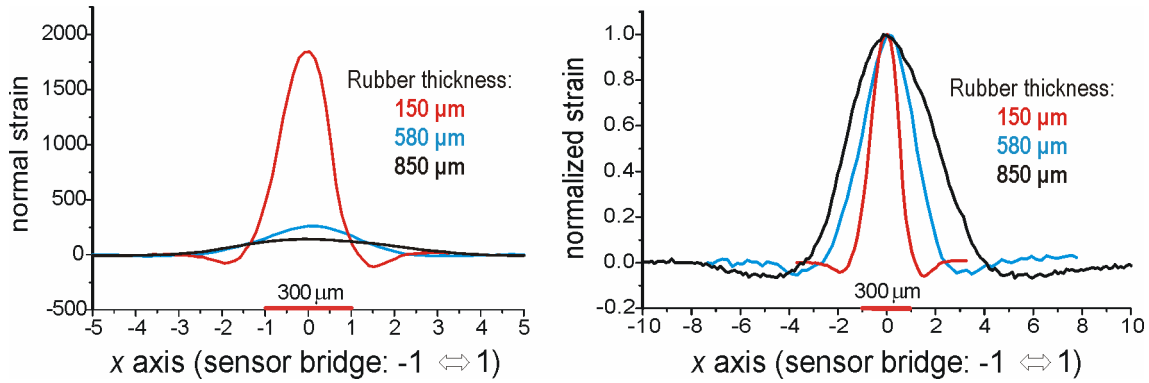
Figure 4.15. Normal strain distribution as a function of rubber thickness (left), with normalized curves also (right). The width increases, the amplitude decreases with thickness (chip No.: 5b)

To compare these measured shapes with the theoretical ones, see Figure 4.3 and Figure 4.4[11] The value of the two extracted parameters can also be seen below, in Figure 4.16.
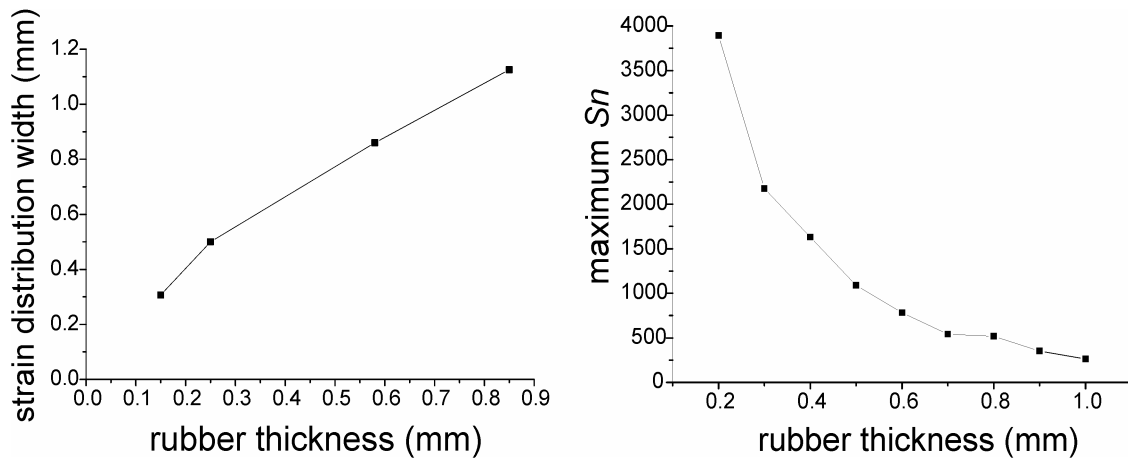
Figure 4.16. As rubber thickness grows, the strain distribution flares and declines – the sensor loses sensitivity and acts more as a low-pass filter [chip No.: 5b (left), 8b (right)]

Although the shape of the measurements resembles the theoretical curves, we are far from a perfect match. The measured *W* curve is linear, but its slope, 1.14 is different from the predicted 2.82. Also, the *A* curve can be fitted better with a $1/z^{1.45}$ function instead of the theoretical $1/z^2$. In other words, according to the measurements the u_{zz} curves are narrower than the prediction and their amplitude declines less as rubber thickness grows. In general, the normal strain distribution resembles more the theoretical response of a thinner rubber layer, which is also in accordance with the increased lateral inhibition property. The difference between the theory and the measurements is probably a result of

---

[11] the mentioned figures represent the stress field, not the strain, however, the character of the stress and strain distributions as a function of rubber thickness are quite similar

the discrepancy between the idealized infinite geometry and the real finite structure. Nevertheless, the half-space model is still the most efficient one to give explanation to the behavior of the covered sensor.

Extending our investigations from the normal strain component to the shear one as well (still concerning only the values along $y = 0$, and the shear component that is not zero in that cross-section), our first task is to compare the relative amplitudes of these two curves, which basically determine the sensor's relative sensitivity to normal and shear forces. This ratio will be named the *normal-to-shear sensitivity* correspondingly, and will be defined as follows:

$$\beta_{ns} = \frac{\alpha_s}{\alpha_n}. \tag{4.19}$$

The value of β_{ns} is obviously not one—it depends on the sensor design and the adhesive properties of the elastic cover. However, it can be determined from the previous measurement results, based on the following simple calculation. Let us take a look at (4.16) again, along the line $y = 0$. Here u_{zz} has a minimum at $x = 0$, while u_{xz} has an extremum at $x = \pm z/2$. From these extrema we get:

$$\left| \frac{u_{zz}\big|_{x=0;y=0}}{u_{xz}\big|_{x=\pm z/2;y=0}} \right| = \frac{1}{\beta_{ns}} \frac{|S_n|_{\max}}{|T_x|_{\max}} = \frac{25\sqrt{5}}{24}. \tag{4.20}$$

Now all we have to do is measure the absolute maximum values in the normal and shear strain components along $y = 0$ in Figure 4.13, and determine how much their ratio differs from the calculated theoretical value of β_{ns}. Performing multiple measurements on a sensor with rubber thickness of 200 μm, after six trials on the same taxel we got $\beta_{ns} = 1.46 \pm 0.04$, which means that the sensor is more sensitive to normal forces than to shear ones. This is what we would expect taking a look at the flat sensor design. Note that there exist several methods aiming to enhance the shear-strain transmission. It can be done by changing the sensor design, at the price of losing the described analytical characteristics, as we will show in detail in the next chapters.

On different sensors the value for the normal-to-shear ratio differs a bit, which can be the outcome of the difficulty in the experimental testing. In general, an average value of 1.5 is used as a good approximation. The absolute value of the α linear constants is not known. It could be measured experimentally with precise force-feedback testing, but we do not need it for the time being.

Before the final conclusions, a "visual summary" of the proceeding investigations is given in Figure 4.17, where the theoretical strain distribution and the measurement results (adapted from Figure 4.5 and Figure 4.13, correspondingly) are compared. The relative amplitudes of the measurements are additionally compensated here with the value of β_{ns}.
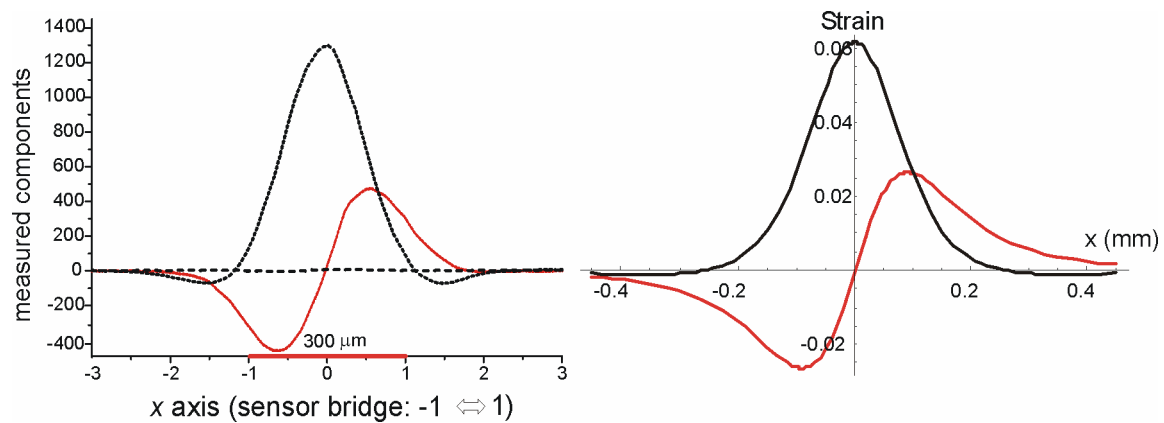
*Figure 4.17. Comparison between the measured three-axial components under a cover of 200 μm (left)
and the strain distribution of the elastic half-space model at the same depth (right) (chip No.: D)*

4.4. Conclusion

In this chapter we analyzed the effects of the elastic cover of the tactile sensors. The cover is treated as an a priori information coding layer in the sensor design, with spatially continuous input and discrete output at the sensor location. We used the elastic half-space model to describe the behavior of the cover in theory. With high spatial resolution measurements on our real three-axial sensors and using some new characterizing parameters we showed that the model gives a fairly accurate picture of the receptive field properties of the covered sensor for a point load. We concluded that using flat elastic covers, the signal of our sensors can be approximated by a linear function of three strain tensor components in the rubber. Although there is some mismatch between the theoretical strain distribution and the measurements due to the necessary constraints in

the solution of the theoretical model, the used half-space model is still the most feasible approximation we can use.

Besides all the success in the characterization, there is still one quite furious obstacle that inhibits the efficient operation of the sensors. We could see in this chapter that even the simplest point load creates a very complex strain distribution in the rubber. However, in practical use, we are never interested in the generated local strain components under the cover—we need only its source, the spatially continuous surface indentation. The procedure of decoding the real surface indentation from the measured strain components is an inverse problem that always gives a lot of headache to its challengers. The solution to this dilemma will be the topic of the next chapter.

Chapter Five

THE INVERSE PROBLEM OF THE ELASTIC COVER

5.1. Introduction

In the previous chapter we saw that the skin-like elastic cover of a tactile-sensor array plays a fundamental role in determining how the sensor responds to an arbitrary surface stimulus. Indeed, this cover is the first spatial-temporal sensory instruction in a tactile cellular wave-computer, or in living, neural-tactile signal processing organs.

The behavior of the cover was described by the elastic half-space model, which gave a picture of the stress/strain distribution deep inside the rubber—generated by the surface indentation during physical contact with the environment. We saw that even this direct problem needs special care and thus can be solved analytically only in restricted cases. Moreover, even the simplest solution has a very complex form.

Unfortunately, when we use the sensors in an arbitrary tactile application for mapping features of the environment, we cannot be satisfied at all with the success of this descriptive model. Using the measured strain tensor components that are available at limited discrete points at the bottom of the cover, we have to determine the real surface indentation, which can be a spatially-continuous, two-dimensional arbitrary function. Without any hesitation I can declare that any closed-form solution to this inverse problem in a general case does not exist. Fortunately, there is still some hope for a quite good approximation, known by anybody with at least one hand…

In the remaining part of the dissertation this inverse problem will be treated from many different aspects. In this chapter we will stay with mathematics and the elastic half-space model, and investigate the possibilities of analytical solutions. In the next chapters we will seek motivation from nature, and change the sensor design in neuromorphic ways to overcome the difficulties of the inverse problem.

5.1.1. Inverse problem in the literature

The inverse problem of the elastic cover on top of a tactile sensor has been attracting the attention of scientific groups for decades now, but it still remains an interesting and difficult task to deal with. The reason for this is that most of the groups had sensors measuring solely the normal stress/strain component; therefore, their approaches had different starting points and thus they constructed incomplete methods using scarce information.

For the simplest case, the static point load, Fearing and Hollerbach (1985 [6]) described an analytical but not practical and not completely solved method. The same group used linear (Fearing, 1990 [7]) and non-linear (Fearing and Binford, 1991 [8]) inverse-filter processes to determine the curvature and location of objects, but their methods are far from real-time. They also work in a different spatial domain—their characteristic sizes are about one order of magnitude larger then ours.

Numerical solutions using neural network training to determine object shapes can be found in (Caiti et al., 1995 [32]), however, reliable experimental data are not provided. Chen et al. (1995 [44]) investigate the inverse problem using moments and iterative algorithms, but they need to combine signals from more than one sensor at once, and lack good experimental data again. Many other groups were trying to extract different features from tactile data, but all of them missed to have a reliable and small enough tactile sensor, measuring at least three components of the strain/stress tensor[12]. Having developed these sensors, we can first concentrate on the basic solutions again.

In this chapter we remain in the static case, and investigate what we can extract from measurements on *one single three-axial taxel* and a *flat cover*. We invert the direct solution of the normal point load, namely, we determine the exact location and the amplitude of the normal load by measuring three local strain components at one point

---

[12] It is very interesting that without three-axial sensors, when one uses the signal of three independent taxels measuring only the normal stress/strain, the inverse problem in any arrangement of the taxels is reduced to the solution of high-order equations, which are hard to solve and where the smallest measurement error generates ambiguous solutions. With three-axial sensors the course of the solution is completely different, as we will see soon.

under the cover, thereby creating a kind of tactile hyper-accuracy. We support our results with real-time experimental data, and also extend the analytical solution to a three-component point load, using more than one taxel.

5.2. Inverse solution for a point load

The frame of reference is the same as in the previous chapter. We use the coordinate system of Figure 4.1 and the point load solution of (4.16).

Our goal is now to express Q, R, F, x and y with the three strain components. We introduce polar variables α and ρ on the surface, where α can be derived simply from the strain components:

$$\tan \alpha = \frac{y}{x} = \frac{u_{yz}}{u_{xz}},$$

$$\rho^2 = x^2 + y^2. \tag{5.1}$$

We also introduce a dimensionless variable A, which can be calculated from the three measured strain components, too:

$$A^2 = \frac{u_{xz}^2 + u_{yz}^2}{u_{zz}^2} = \frac{9z^2\rho^2}{\left(\rho^2 - 2z^2\right)^2}. \tag{5.2}$$

Since A is a measured value and z is known from the sensor design, (5.2) becomes a simple second-order equation for ρ^2, with the two solutions:

$$\rho_{1,2}^{\ 2} = z^2 \left(2 + \frac{9 \pm \sqrt{81 + 72A^2}}{2A^2} \right). \tag{5.3}$$

5.2.1. Partial solution for a normal load

From now on we take $Q = R = 0$ for a while (i.e. only the normal load component is present), in order to analyze the solution more precisely. In that case three distinct regions for ρ can be separated depending on the u_{zz} distribution (Figure 5.1).
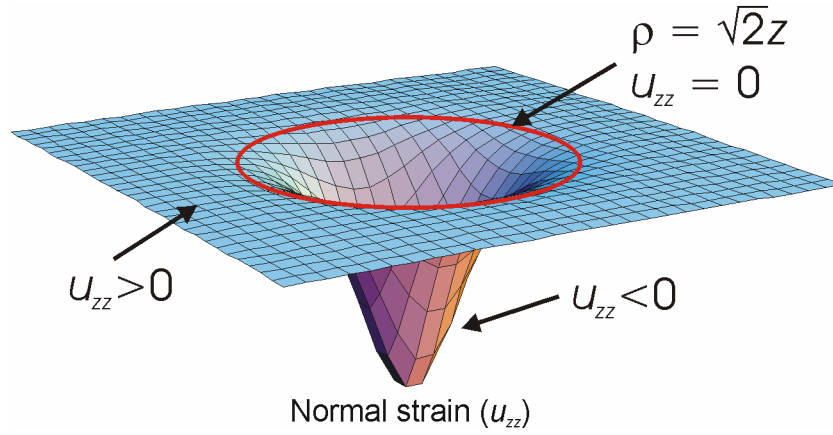
Figure 5.1. Strain distribution (u_{zz}) under a normal point load. The main region of interest—within a radius of $\sqrt{2}z$ around the load—is when the normal strain takes negative values. In this case the inverse method can be based on reliable experimental data with high SNR

When $\rho < \sqrt{2}z$, the normal strain component (u_{zz}) becomes negative—basically this is the region where u_{zz} is accurately measurable. In this case for ρ^2 we get the value:

$$\rho^2 = z^2 \left(2 - \frac{12}{\sqrt{9+8A^2}+3} \right). \tag{5.4}$$

If $\rho = \sqrt{2}z$, u_{zz} becomes zero and A goes to infinity. With $\rho > \sqrt{2}z$, u_{zz} becomes positive, and we get:

$$\rho^2 = z^2 \left(2 + \frac{12}{\sqrt{9+8A^2}-3} \right). \tag{5.5}$$

It is exciting to see that with the thickness of the rubber we can adjust the radius of the region where u_{zz} is negative and where the properties of the force can be recovered with high precision. However, by thickening the rubber, we need higher force values to give high enough strain in the rubber for the measurement.

After determining ρ and α, we can calculate x and y easily:

$$x = \rho \cos \alpha,$$
$$y = \rho \sin \alpha. \tag{5.6}$$

The amplitude of the force is extracted from any component of (4.16) now (e.g. from u_{zz}):

$$F = u_{zz}\frac{4\pi E\left(\rho^2 + z^2\right)^{5/2}}{3\left(\rho^2 - 2z^2\right)z}.$$

(5.7)

From one point of measurement these are all the data we can reconstruct analytically. If the loading force has more than one component, (5.7) takes the following form:

$$Qx + Ry + Fz = u_{zz}\frac{4\pi E\left(\rho^2 + z^2\right)^{5/2}}{3\left(\rho^2 - 2z^2\right)}.$$

(5.8)

In this case we need more restricting assumptions for determining the force components. For example, if we know the friction coefficient (μ), Q and R can be expressed with F, and hence the normal and tangential components can be separated.

Note that if we had sensors measuring the *stress* in the material, and not the *strain*, the equations would become even more simple, and we would avoid the singularity at $\rho = \sqrt{2}z$. Substituting strain for stress in the definition of A and α, instead of (4.16) and (5.3) now we write:

$$\begin{pmatrix}\sigma_{xz}\\\sigma_{yz}\\\sigma_{zz}\end{pmatrix} = \frac{3\left(Qx + Ry + Fz\right)}{2\pi\left(x^2 + y^2 + z^2\right)^{5/2}}\begin{pmatrix}-xz\\-yz\\-z^2\end{pmatrix}$$

(5.9)

and

$$\rho = zA_{\sigma}.$$

(5.10)

5.2.2. Full solution using a sensor array

Having a rectangular array of strain sensors at a depth of z, with a given d distance between the neighboring sensors, we need to fulfill the following constraint to have at least three sensors close enough to the point load at all times:

$$d < \frac{1+\sqrt{2}}{2} z \approx 1.2z. \tag{5.11}$$

This has not yet been achieved in our sensor-array design; hence this subsection so far remains a theoretical assumption. With three sensors we have three equations similar to (5.8). We calculate their right side and name it M:

$$Qx_i + Ry_i + Fz = u_{zzi} \frac{4\pi E\left(\rho_i^2 + z^2\right)^{5/2}}{3\left(\rho_i^2 - 2z^2\right)} = M_i \quad (i = 1, 2, 3). \tag{5.12}$$

From this the general solution can be deduced using simple algebraic calculations:

$$
\begin{aligned}
Q &= \frac{\left(M_2 - M_3\right) y_1 + \left(M_3 - M_1\right) y_2 + \left(M_1 - M_2\right) y_3}{\left(x_2 - x_3\right) y_1 + \left(x_3 - x_1\right) y_2 + \left(x_1 - x_2\right) y_3}, \\
R &= \frac{\left(M_2 - M_3\right) x_1 + \left(M_3 - M_1\right) x_2 + \left(M_1 - M_2\right) x_3}{\left(x_3 - x_2\right) y_1 + \left(x_1 - x_3\right) y_2 + \left(x_2 - x_1\right) y_3}, \\
F &= \frac{\left(M_3 x_2 - M_2 x_3\right) y_1 + \left(M_1 x_3 - M_3 x_1\right) y_2 + \left(M_2 x_1 - M_1 x_2\right) y_3}{\left[\left(y_2 - y_1\right) x_3 + \left(y_1 - y_3\right) x_2 + \left(y_3 - y_2\right) x_1\right] z}.
\end{aligned}
\tag{5.13}
$$

5.2.3. Considerations with real sensors

When checking the validity of our theory on real sensors, we need to take into account that their signals are not the exact strain tensor components but their linear functions with different slope in the normal and shear directions, as described in (4.15). Therefore, we need to change the definition of A slightly. Let us define A_m (from $A_{measured}$) in the following way:

$$A_m{}^2 = \frac{T_x{}^2 + T_y{}^2}{S_n{}^2} = \left(\frac{\alpha_n}{\alpha_s}\right)^2 A^2 = \frac{1}{\beta_{ns}{}^2} A^2 , \tag{5.14}$$

where we the previously defined normal-to-shear sensitivity (β_{ns}) is also taken into account. Substituting (5.14) into (5.4) we get:

$$\rho^2 = z^2 \left(2 - \frac{12}{\sqrt{9 + 8\left(\beta_{ns} A_m\right)^2} + 3} \right). \tag{5.15}$$

5.3. Measuring tactile hyper-accuracy with a flat cover

In the following we validate the theory of the previous section with measurements on the real three-axial sensors. In addition to showing the feasibility of our model, we measure the rate of tactile hyper-accuracy, achieved by only utilizing the flat cover and its previously introduced mathematical description. We also investigate the boundaries of our theory by giving a list of the possible sources of error.

I used the measurement results of the whole two-dimensional receptive field, presented in Figure 4.14, and transformed the measured three-axial data on the whole plane into coordinates and force amplitude, using the deduced inverse equations. One critical point that alters the final arrangement of the calculated coordinates is the proper setting for the normal-to-shear value. To see the pure effects of the changes in β_{ns} we modeled the results first on a rectangular grid of points with errorless theoretical data (Figure 5.2).
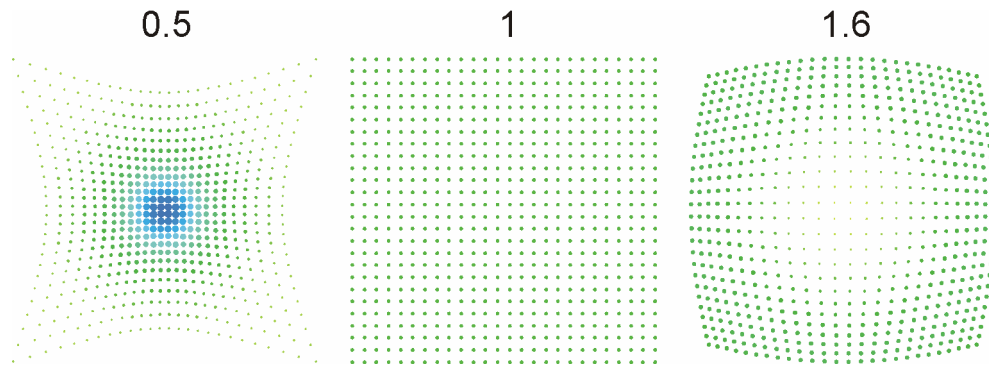
Figure 5.2. Modeled results of the 2D point-load location-reconstruction experiment on a rectangular grid of points. The numbers above each plot represent the value of the normal-to-shear ratio chosen for the location and amplitude reconstruction. Amplitude is represented by the size of each point. Altering the normal-to-shear ratio changes the homogeneous mapping of the calculated locations and load amplitudes

Similar results can be seen in Figure 5.3 reconstructed from the measurement data, using β_{ns} = 1.5, as an approximately feasible value.
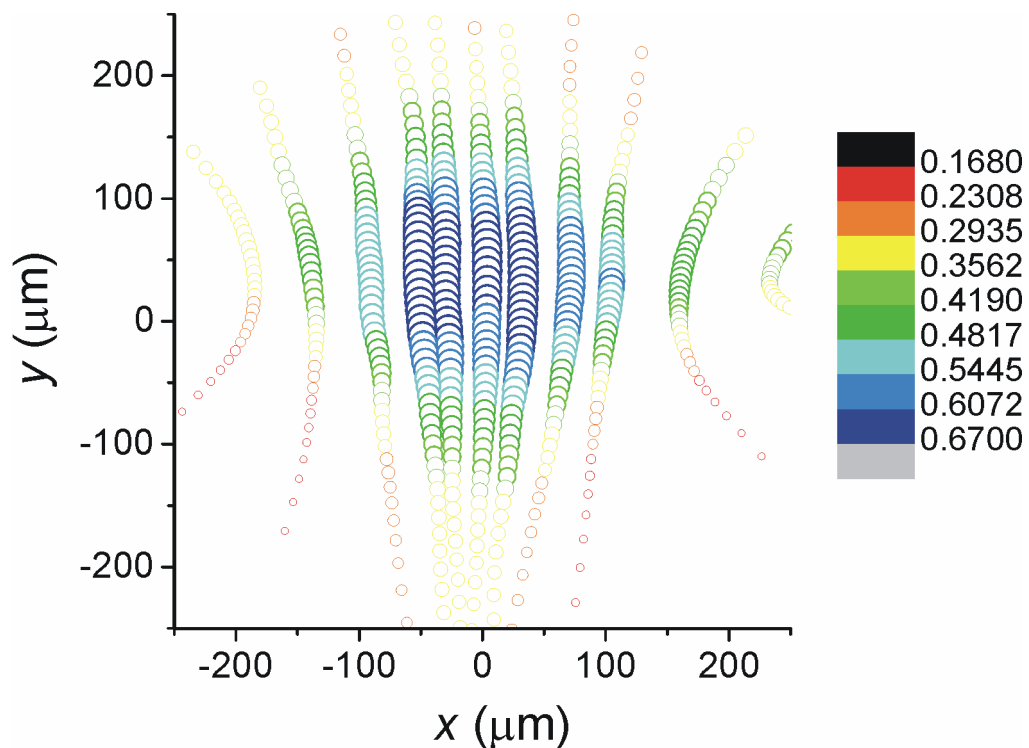
Figure 5.3. Location and amplitude reconstruction of a point load, moved by a stepper motor over one taxel, along parallel lines. Each circle is one data acquisition point, measured by our software at 50 Hz. The two axes show the plane of the reconstructed surface coordinates, while both the size and color of the circles represent the local reconstructed load amplitude

The experimental result in Figure 5.3 shows that our model is fully functional. There is quite a bit of error far from the center of the taxel, and the mapping of the reconstructed

locations there resembles the underestimation of β_{ns}. In other words, the deviation between the measured strain distributions and the model is not constant; it is a function of distance from the center of the taxel. This function is not known theoretically, but aiming at better results it can be measured point by point as calibration data. Nevertheless, within a radius of approximately 150 μm this is not needed, because reconstructed locations and amplitudes are reliably calculated there. Here we achieve kind of a tactile hyper-accuracy with an approximate precision of 3–5 μm.

The absolute value for the normal and shear coefficients can be determined by comparing the known load amplitude and the calculated one. However, the feedback from our current strain-gauge in the loading needle is not reliable enough for precise calibration.

Knowing the exact speed of the stepper motor and the data acquisition rate, we were also able to give quantitative results. We took only those measurement points that correspond to the middle line of Figure 5.3, and measured its slope in time (Figure 5.4).

Figure 5.4. Stepper motor speed calibration on the reconstructed locations along the center measurement
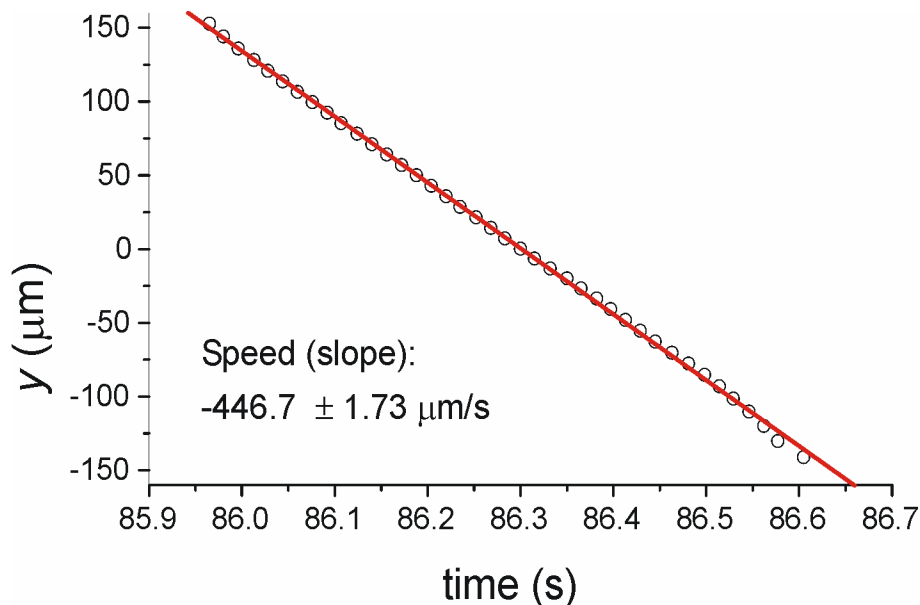*line (y = 0)*

The calculated speed (0.45 mm/s) is a bit less than the real value (0.5 mm/s), but it can be compensated with a linear constant again, which is kind of the same as raising the cover thickness a bit in the model.

5.3.1. Error estimation

This section is only a qualitative enumeration of the facts that have a possible effect on the results. There are quite a lot of things that could be taken into account. Here I only present the most significant ones. According to my knowledge, the sources of error could be the following:

- Our model is infinite, with homogeneous and isotropic behavior and with a Poisson's ratio of 0.5. The real sensor design is finite, with some non-linearity at high strain values. Since modifying the model is quite a bit of a challenge, we take this source of error as a fact, and treat the results accordingly.
- The point load is a needle with finite diameter. However, the tip of the needle was treated to be hemispheric to cause similar strain distribution to the point load. (The similarity is getting more profound anyway with increasing distance in the material away from the indentation point).
- The sensor itself is not point-like, it has finite size, too.
- The experimental testing is very delicate, because the loaded sensor is quite sensitive to mechanical vibrations. A few microns of dislocation in the loading needle causes huge changes in the loading force and, therefore, in the measured strain values, too. The deviation of the rubber surface from a perfect plane, hence, causes the same effect.
- The stepper motor's magnetic field sometimes creates high frequency noise in the measured data.

5.4. Conclusion

In this chapter I solved the inverse problem of a *flat* elastic cover in the case of the most basic indentation type, the static point load. In other words, I gave an analytical model for reconstructing the location and the amplitude of an arbitrary point load over the surface of the elastic cover. Although there are many a priori simplifying assumptions in the model, experimental qualifications prove its feasibility. With only one taxel I were able to achieve a kind of tactile hyper-accuracy, and reconstruct the location of a normal, point-like load with around 3 μm accuracy over an area of 300×300 μm, with reliable amplitude values, too. Without experimental validation I gave the inverse solution to 3D point-loads, too, using the signal of three three-axial taxels.

Continuing this mathematical approach, our next task should be to find nice solutions for more general cases, too. However, if the indentation is more complex (as in any general tactile manipulation task) and its spatial resolution is below the receptive field size of the taxels, this inverse problem becomes enormously difficult to solve, and our attempts would most probably lead us only to other special cases and no general treatment of the problem. Therefore, we should observe this whole phenomenon from a totally different point of view.

First and foremost, we should keep in mind that the signal of human mechanoreceptors are also coded by the skin, consequently, we are blessed with the same intriguing inverse problem during tactile perception. Good news is that, despite this, we can still use our hands to measure all surface properties of grabbed objects efficiently. Hence, mimicking nature would be a good idea, and could be done in two different ways in our case. We can either treat the inverse problem as a direct one by taking only the useful information from the measurements, finding features that we can detect and training e.g. neural networks or any software to "understand" data. The success of this version depends on the software we design, which is analogous to the function of the brain in tactile perception. Alternatively, we can find ways through the "hardware" of the sensor to ease our problem.

In the next chapter, instead of generalizing our solution to more complex indentation profiles, we rather try to simply abolish the need for the complex inverse solution by changing parts of the sensor design using new neuromorphic features. In other words, we will change the sensor's functionality to be more straightforward and to have a more direct connection between the real surface load and the measured signals.

Chapter Six

NEUROMORPHIC ELEMENTS IN THE TACTILE-SENSOR DESIGN

6.1. Introduction

In Chapter Two we saw that nature uses several interesting components for enhancing the efficiency of tactile sensing. In this chapter we will mimic two of these features: the *hair* and the *fingerprints*. We will equip our sensor design with neuromorphic elements that resemble these parts, and investigate how they alter the overall signal coding mechanism of the system. Besides providing real measurement data for the neurobiologists on the stress-coding behavior of these natural structures, we can also benefit from their presence by enhancing different capabilities of our own sensors, too.

The application of fingerprints will also lead us to the need for a similar, but non direction-selective structure. Therefore, we will also equip our covers with *elastic hemispheres* and use a finite-element simulation to model the behavior of these bumps over two different sensor types. First, we attach the bumps to the usual three-axial sensors to simplify the inverse problem of their cover. We will see that with these simple structures we can localize the otherwise continuous input over the taxels and detect normal and shear force components independently. Secondly, I will also show a truly simple and efficient method for extracting shear-load data from a general pressure-sensor array. Finally, I confirm the theoretical results with real-time experimental data and use the measurements for texture classification, as an application example.

We will start our investigation with shear-force enhancement, using artificial hair.

6.2. Artificial hair

In the preceding receptive field measurements (e.g. in Figure 4.13) we saw that the shear sensitivity of our sensors is less than the normal one (with a normal-to-shear sensitivity of around 1.5). Shear sensitivity can be increased efficiently by attaching hair-like elements to the sensor design.

6.2.1. Novel design with alkaline etching

We experimented with different sensor structures with rigid load-transmitting rods in the middle of the sensor membrane. One approach is based on a totally new MEMS technique using alkaline etching instead of the HF-based porous silicon etching (Vázsonyi et al., 2005 [5]). In this structure the shear-load transmitting element is fabricated out of the silicon itself, together with the deformable membrane (Figure 6.1).
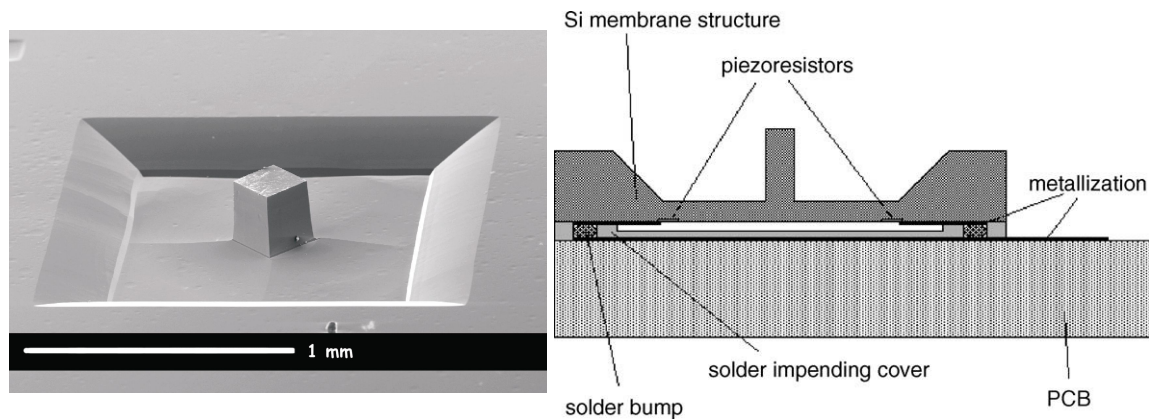
Figure 6.1. The novel sensor design with a load transmitting rod at the center of the deformable membrane (left); schematic side view of the structure with the separately prepared read-out circuitry below is also given (Vázsonyi et al., 2005 [5]) (right)

One unique feature of this structure is that there is no read-out circuitry on the chip itself, but the piezoresistors and the contact pads are located at the bottom surface of the wafer. This way, the MEMS process has more freedom, and the read-out circuitry can also be designed separately, on a different chip. The two structures are attached together using flip-chip technique. This idea is remarkable and enables the construction of arbitrary sized chips with sophisticated read-out and signal-processing on board. The only drawback is the sad fact that so far we have not been able to connect the MEMS structure with any read-out chip efficiently; however, measurements on a single taxel show the feasibility of the structure as a new three-axial tactile sensor (Figure 6.2).
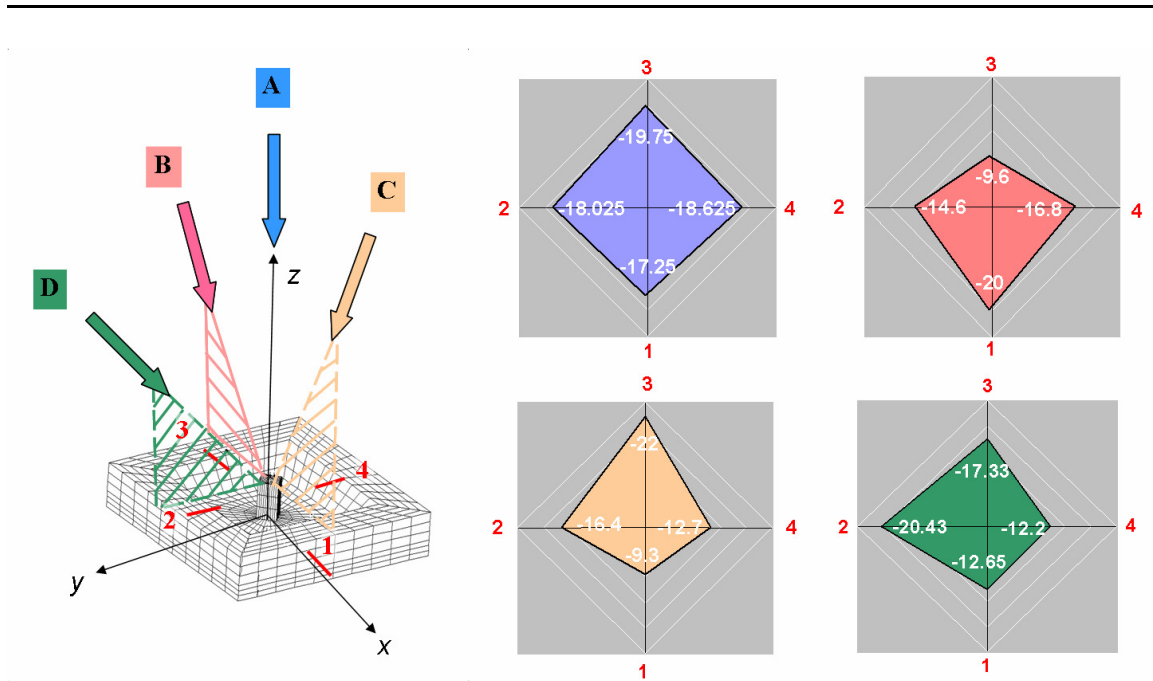
Figure 6.2. Measurement results with loads of different direction. Normal loading creates symmetrical response in the four piezoresistors, slanted loading shows asymmetric response, in accordance with the loading direction

6.2.2. Artificial hair in the old sensor design

Using the well-known old sensing elements we were also able to attach hair-like elements to the center of the bridges, explaining the meaning of the central hole in the deformable part of the taxels shown in Figure 3.8. In this structure the shear-load transmitting elements were attached to the sensors one by one after all the technological processes had been finished. The hair-like rigid rods were either made of epoxy[13], or were cut from a simple silicon wafer (Figure 6.3). They both protrude through the center hole of the membrane and sit on another elastic epoxy[14] layer, which fills the cavity to the half of its depth.

---

[13] Araldite 2014 (Vantico Ltd.)

[14] Araldite DY022 (CIBA)
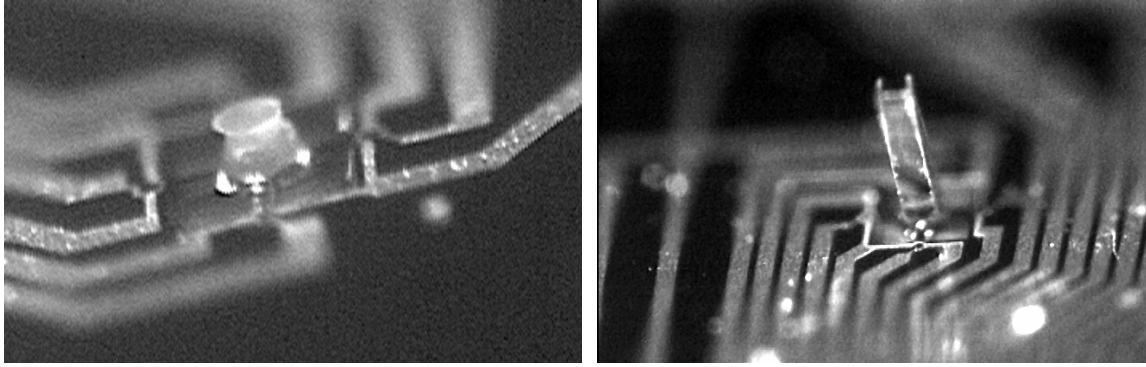
Figure 6.3. Photographs of taxels with shear-load enhancing rods made of epoxy (left) or silicon (right)

After the rods were fixed to the structure, we prefabricated a layer of Elastomer A[15] (with a thickness of 150–500 µm, as before) and glued it to the top of the rod with Elastomer B[16]. For precise positioning we temporarily placed a spacer tool outside the active area. During this procedure the silicon rubber filled up the remainder of the cavity. In the final step we injected viscous silicon rubber (of type Elastomer A) into the space between the top elastomer and the Si surface around the taxel, thereby providing robust, compact coverage[17]. A scheme of the cross-section of the complete sensor is presented in Figure 6.4.
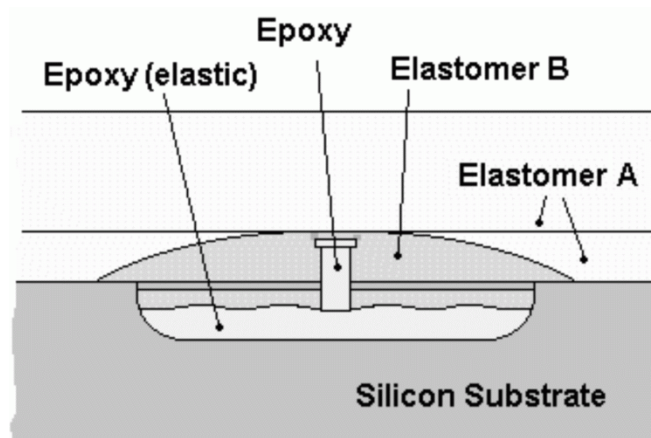
Figure 6.4. Cross-section of the sensing structure after the completion of the covering process. In this
version a load-transmitting rigid bump is attached to the membrane to enhance shear sensitivity

---

[15] Either OXAM DC (T-Silox Ltd.), or the previously used Elastosil® RT-601 (Wacker-Chemie GmbH)

[16] Elastosil® E41 (Wacker-Chemie GmbH)

[17] We also experimented on sensors, where the rods were not totally covered with rubber (like on the hairy skin), but it resulted in too much sensitivity and the sensors broke soon. Less rigid structures—like the hair itself—should work fine and could be used in many further interesting applications...

This extra element in the sensor design acts the same way as a single hair in our skin—it elongates the force arm and sensitizes the structure to shear forces. Accordingly, the characteristics of the measured signals change fundamentally, lateral force components arising even at normal loading become dominant (Figure 6.5).
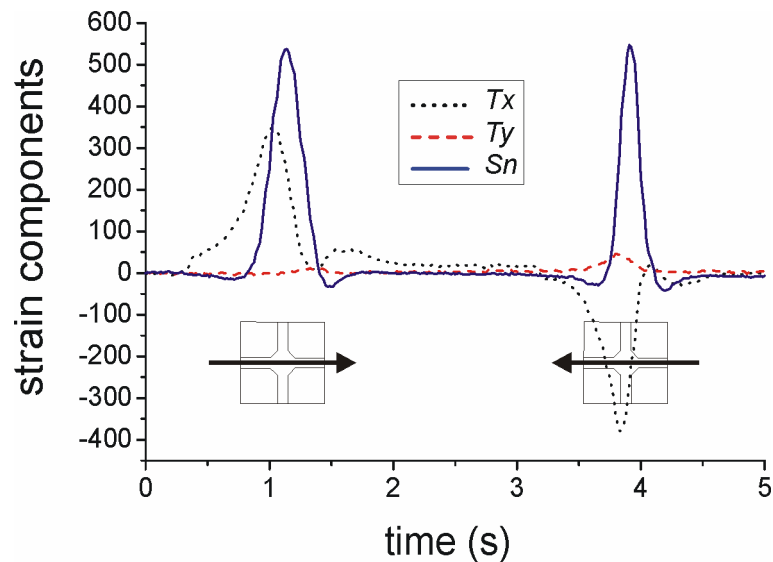
Figure 6.5. Response of a hair-like sensor. Indentation moves from left to right and back along the x axis, as depicted by the arrows below. the normal component (Sn) is positive, one shear component (Ty) is nearly zero, the other (Tx) reflects motion direction (chip No.: 2j)

As friction pushes the shielding rubber in the motion direction of the indentation, it evokes a greater response in the corresponding shear-strain component through the attached "mini-joystick." Therefore, indentation motion direction and friction coefficient can be measured reliably by the two shear components, while indentation amplitude is still effectively marked by the normal one. When the indentation is not a point load, but a larger object with characteristic sizes greater than the sensor size (e.g. when the sensor is pressed by a finger), the overall shear response in general shows reliably the direction and amplitude of the shear force acting on the surface. As a conclusion, receptive-field shapes can be modified essentially by the application of a rigid rod. In that case, sensors become highly sensitive to shear stress, while the sensitivity to normal load is not affected considerably. The value of the shear sensitivity can be set by the length of the rod.

The only disadvantage of this element is the need for the manual installation, which encumbers the production of many perfectly similar taxels. Therefore, in the next

sections we will leave the sensor structure as it is, and try to alter the *geometry of the cover* to enhance the capabilities of the sensors.

6.3. Fingerprints

In Chapter Two we saw that another important feature of our skin (and e.g. the star-nosed mole's star-nose) is its raggedness, which results in special filtering effects in the skin tissue. Consequently, the emerging parts of any elastic cover should also modify the properties of the overall sensory structure. First of all, if two materials contact, the location of the highest stress values is always around the first contact points. Secondly, due to the complex behavior of the elastic material, some components of the stress and strain distribution reach their peak value right below the highest and lowest points of a modulated surface. Therefore, with a well-chosen location for the sensors in the rubber, the sensitivity of the structure can be maximized without losing its protection, not to mention the enhanced gripping properties of the surface. Finally, we concluded before that the spatially-continuous input on a flat elastic surface makes it enormously difficult to decode the surface-load distribution from the measured stress/strain. Having a ridged surface, the input forces are also localized to some extent, and thereby, the inverse problem becomes simpler, too.

Benefiting from all the above advantages of the fingerprints, we molded elastic covers with ridged surface and checked the modified behavior of our neuromorphic structures.

6.3.1. Modified receptive fields with fingerprints

The novel elastic covers were made from the same materials as used for their flat "brothers," but the formers were cured in a negative mold with a flat glass on top, spaced 200 μm above. Hence, the original 200 μm thick flat cover got extended with a ridge on top. The negative mold was made from a simple silicon wafer by homogeneous etching. The ridge was 250–280 μm high. We varied the width of the ridge between 360 and 760 μm to find the optimal size. The ridge was placed over the sensor so that it lay parallel to one sensory bridge, right over its center. The final structure can be seen in Figure 6.6.
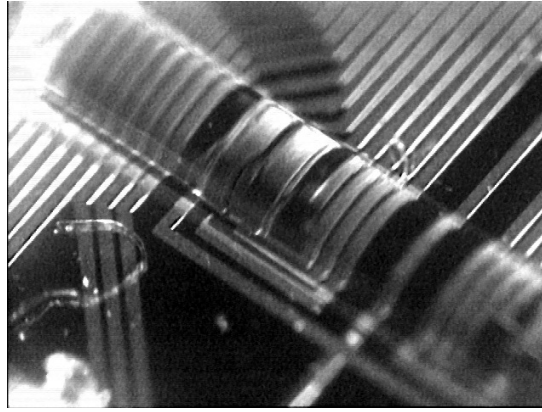
Figure 6.6. The fingerprint-like elastic ridge over the sensor structure

For testing the receptive field of the new structures I used a simple screw, moved over the sensors laterally, creating mainly the same effect as a series of point loads. I compared the shape of the measured strain distributions in three cases: 1) sensor with a flat elastic surface, 2) sensor with a ridge, indentation moving parallel with the ridge, 3) same sensor, but with indentation motion perpendicular to ridge orientation. Results can be seen in Figure 6.7.
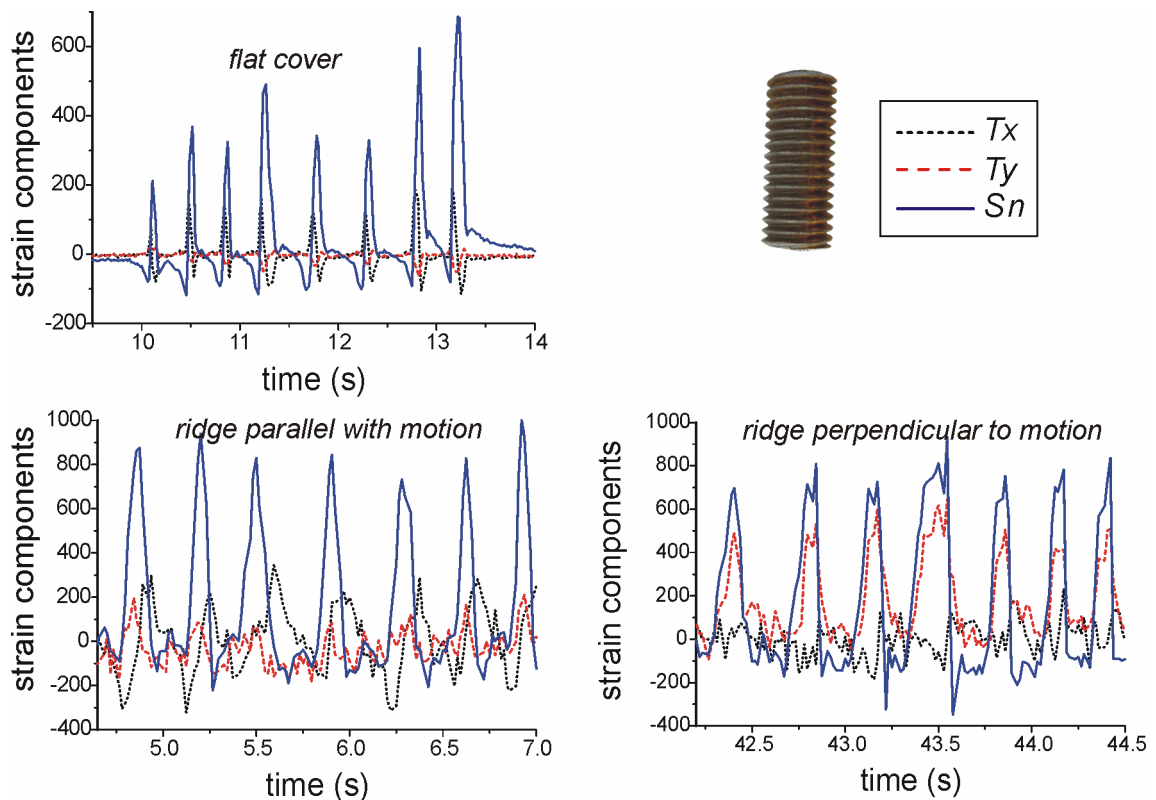
Figure 6.7. Three different responses when the depicted screw was pulled over the differently covered sensors. When the ridge is parallel with the motion, it acts the same way as a flat cover. When the motion is perpendicular to the ridge orientation, the receptive field is changed substantially (chip No.: flat 8b, ridged ts471)

The above measurement illustrates the *direction selectivity* of the ridge. When it is parallel with the indentation-motion direction, it represents the same complicated strain distribution as the flat cover. When the ridge is perpendicular to the indentation motion, it changes the original point-load characteristics into a more direct function of the surface load. It integrates the load from its entire surface and responds to the amplitude of the load and the shear-force direction, which corresponds to the indentation-motion direction. Note that the amplitude of the shear signal is highly increased; moreover, the friction coefficient can also be calculated from the relative amplitudes of the normal and shear components.

Unfortunately, the chip that was equipped with the ridge was an old one with a relatively high level of noise; therefore, the results are not that nice now. However, the responses show the expected characteristics, and that is enough for now. We can conclude that, besides enhancing the sensitivity, the modified geometry efficiently and directly codes different properties of the indentation. Moreover, I could demonstrate the direction selectivity of the fingerprint-like ridges, which can also be used to prove the direction selectivity of human mechanoreceptors under real fingerprints.

In the following section I will analyze the state of the art geometry for the elastic cover, the one which is the artificial version of the star-nosed mole's Eimer's organ. Thus, instead of ridges, in the final sensor design we will use *elastic hemispheres*, which are not direction selective. Details and all the other advantages of this geometry will be presented in the next, final sections.

6.4. The elastic hemisphere

Our last (and most efficient) neuromorphic element in the sensor design is the *elastic hemisphere*. Tremblay and Cutkosky (1993 [46]) describe in detail how hemispheres on the elastic cover enhance gripping properties of a sensor. They use these bumps to transfer vibrations to accelerometers when released by the grip. Here, we follow a different strategy: our goal is to design a cover geometry that enhances the capability and sensitivity of the entire tactile system.

Having hemispheres on the surface, we step over the boundaries of the elastic half-space model. Therefore, for a detailed analysis we create a finite-element (FE) model with the new geometry, and describe the behavior of our newly-shaped cover under different indentations. I will show that the application of elastic hemispheres provides a chance to avoid the solution of the inverse problem of the cover on our three-axial sensors. With measurements on the proper cover—designed according to the finite-element model—I will confirm that the bumps can be used efficiently to localize the load over the taxels and code the three local indentation components independently. Finally, I will use our new sensor design for a tactile-texture classification example, too.

In the meantime, the elastic bumps will be applied to simple pressure sensor arrays as well. I will show that the bumps can also be used to generate *shear* information on an arbitrary one-axial pressure-sensor array by combining the signal of four independent neighboring taxels.

6.4.1. Finite-element model of the elastic hemisphere

Our model is an extension of the well-described elastic half-space, with a hemispherical bump on its surface. In the model we calculate with infinite size once again, and take strain/stress/deformation values from a given depth, at the points where the sensors are to be located. The elastic material is the same—it is assumed to be homogeneous and isotropic, with a Young modulus of 0.87 MPa and Poisson's ratio of 0.499. The value of the Young modulus is only a linear constant in the equations and smaller values for the Poisson's ratio do not change the FE results substantially either. We used the Cosmos Geostar 2.8 (128K version) FE package, with a total number of 1060 elements in the structure (Figure 6.8).
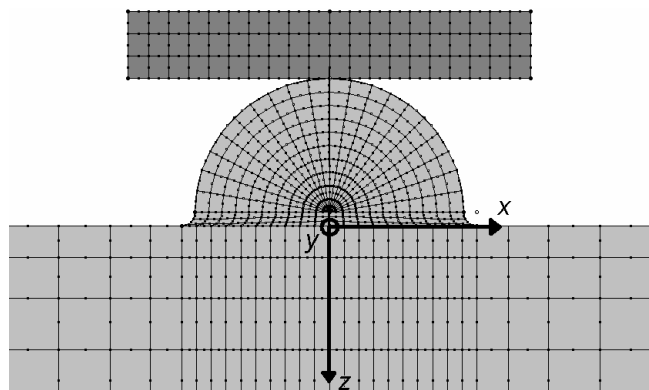

Figure 6.8.   The finite-element model of the bump over the elastic half-space. The flat and rigid indentation touches the top of the hemisphere

In the first run the structure was only two dimensional, with plain-stress approximation along the infinite third dimension (perpendicularly to the plane of this paper). This infinite size was obviously approximated by finite thickness—large enough to cause no change in the results (2 mm). Since the hemisphere and the half-space are both axi-symmetric, this plane-stress approximation is only a slight simplification of the real case—analogous to the 2D projections of a more realistic 3D model. Later, if needed, we will expand the model to three dimensional.

The diameter of the hemisphere is 0.4 mm. The infinite half-space is approximated by a large enough finite size (one order of magnitude greater than the size of the bump, namely 4×2 mm), with zero deformation at the bottom and free edges at the sides. Note that the absolute size of the system is not crucial, only relative distances are important.

The indentation is a flat and rigid object, touching the top of the bump with infinite friction. The high surface-curvature at the junction between the half-space and the hemisphere is effectively reduced with an additional element (linear, inclined at 45 degrees) to avoid high local stress and error. The hemisphere is approximated with linear elements.

In the model we used two independent loads, both applied with the same perfectly rigid object. One acts purely in the x, the other in the z direction. We assume that deformations are small, thus in a general case the final deformation can be calculated from the superposition of the two basic indentation types. A general deformation profile caused by an indentation of 50 μm in the two directions can be seen in Figure 6.9.
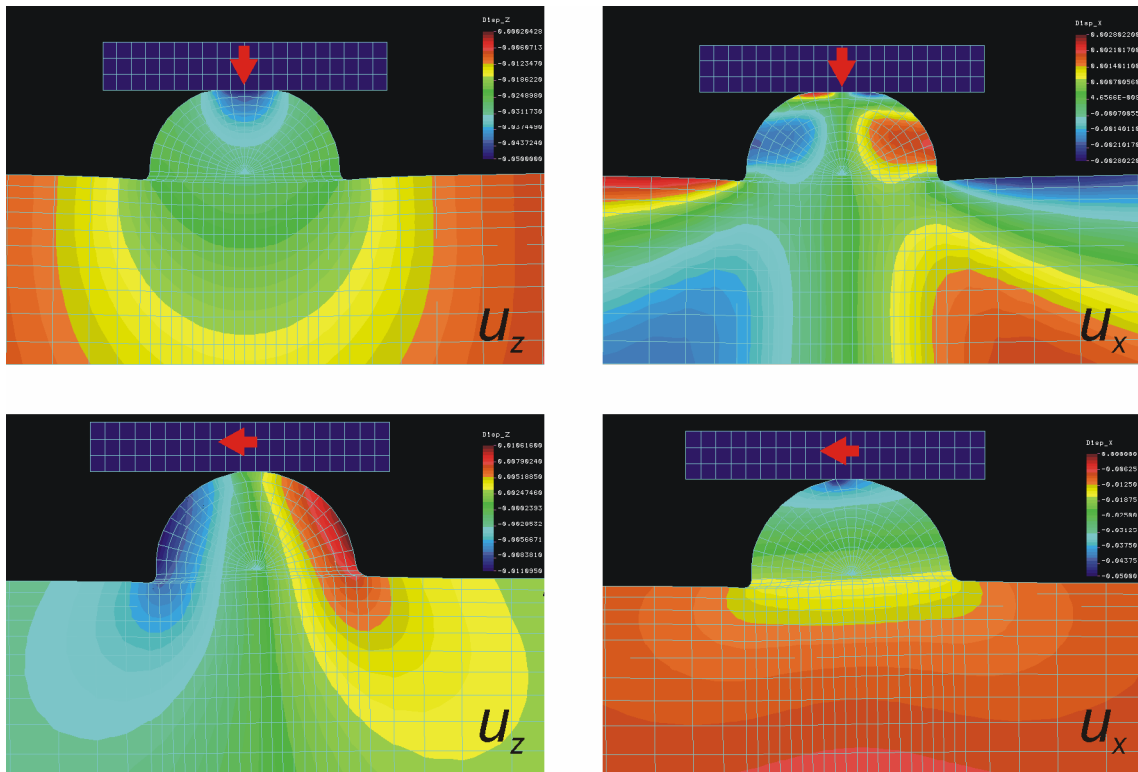
Figure 6.9.   Finite-element results—deformation vector components in the rubber, caused by loads of different direction. The vector component is shown in the bottom right corner of each image, while the force direction is depicted by the red arrows on the indentation

6.4.2. FE results for the three-axial sensors

The three-axial sensor is positioned at a given depth at $x = 0$. Note that along the line $x = 0$ in the presented cross-section, neither the z nor the x directional load causes deformation in the other direction (see the vertical lines at the center of the top-right and bottom-left segments of Figure 6.9). Therefore, if we position our three-axial sensor at a given depth along $x = 0$, the response to the two directions will remain independent.
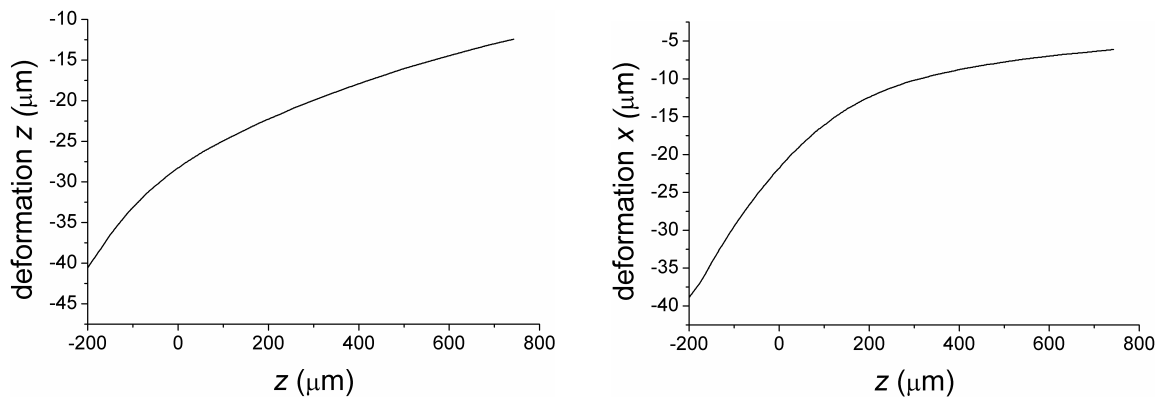
Figure 6.10.   Deformation values along the axis perpendicular to the surface ($x = 0$), at an indentation of 50 μm. Load: z, deformation: z (left); Load: x, deformation: x (right)

For determining the proper depth of the sensor we need to take a look at the deformation values along $x = 0$ (Figure 6.10), and consider that a minimal thickness of 200 μm is needed below the bump for applicability reasons. Obviously, the thicker the rubber, the more we lose from the sensor's sensitivity for both loading types. As a result, in the experiments the minimal 200 μm thin layer is used.

Having determined the exact position of the taxel, the last thing needed is the characteristics of the response as a function of the load (Figure 6.11).
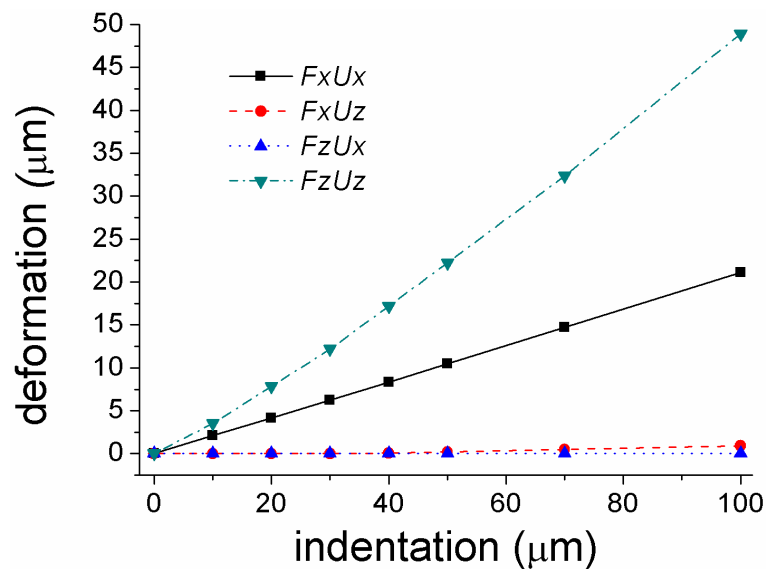
Figure 6.11.   Deformation values at the three-axial sensor location (x = 0; z = 200 μm) as a function of indentation amplitude. FiUj represents the deformation component j under a load in the i direction

(i = x, z; j = x, z)

As can be seen in Figure 6.11, up to a deformation of 100 μm—which is quite a high value for these feature sizes—all characteristics are close to linear. The response to a normal load is steeper, therefore, the overall normal-to-shear sensitivity of the sensor will differ from one (it is about two now). Since the curves *FxUz* and *FzUx* are constant zero, the *x* and *z* components will remain independent, with no cross-talk. Note that our sensors measure the strain, not the deformation. However, characteristics of the strain distribution are similar, thus these results can be used efficiently to predict the functionality of the sensors.

6.4.3. Shear-load measurement with pressure-sensor arrays

If we take a thorough look at the bottom-left section of Figure 6.9, we can note that at a given depth along the line z = const, the deformation z caused by the tangential load is not zero. Instead, it has a maximum somewhere below one edge of the hemisphere and a minimum at the opposite side. This observation also refers to the stress distribution (Figure 6.12), which is measured by any general pressure-sensor array.
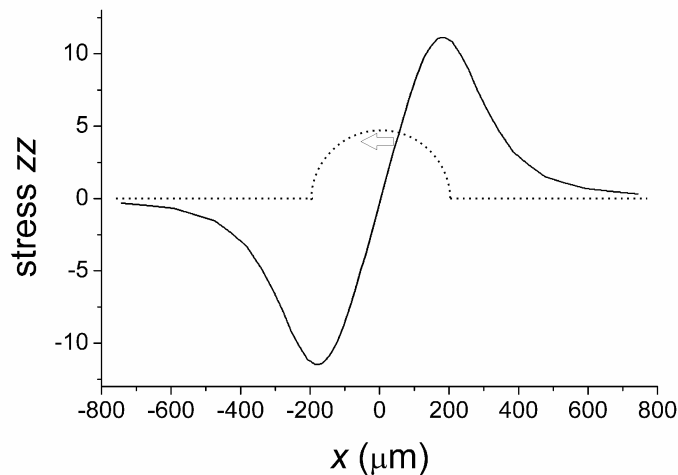
Figure 6.12.   Anti-symmetric stress distribution (solid curve) at a depth of 200 μm under the surface of the half-space and the bump (dotted curve), caused by a tangential load. If two taxels of simple pressure sensors are located at these stationary points, the difference between their signals will code the shear-load efficiently

This observation will be the basis of our following hypothesis. If we put two simple pressure sensors at these stationary points symmetrically, measuring only the normal stress component, the *difference* between the two signals will correspond to the shear load. In the meantime, a possible normal load causes an axi-symmetric stress and deformation distribution (top-left section of Figure 6.9), which can be measured independently with the *sum* of the two signals.

This basic idea of shear sensing is present in (Yamada et al., 2002 [26]). They create a huge artificial finger skin with ridges and use it to extract some shear information from the underlying sensors to prevent slippage during grasping tasks. However, their analysis is not that detailed and their characteristic sizes are much larger then ours. Moreover, using bumps instead of ridges we can also generalize our assumption to the second tangential dimension, all together joining four neighboring pressure-sensor elements from an array to retrieve both shear components of one three-axial taxel (Figure 6.13).
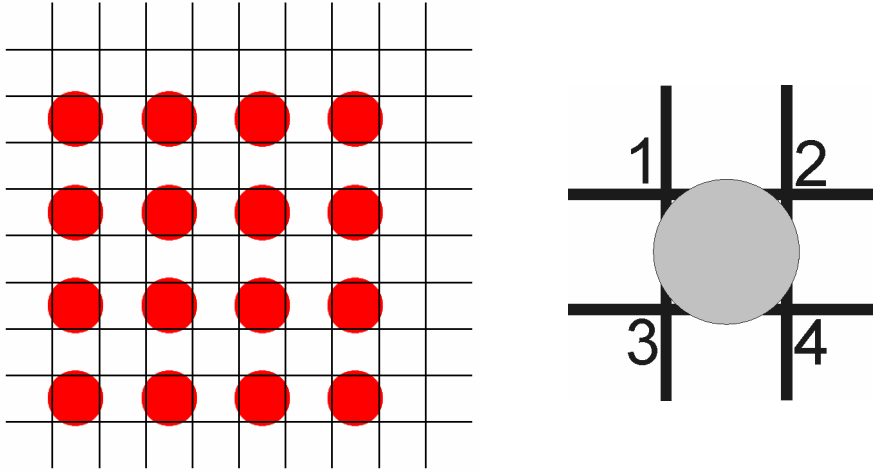
Figure 6.13.   Location of the bumps (circles) over an arbitrary pressure-sensor array (with taxels at the junction of the lines) in top view; on the left part a 9×9 sensor array of 1D taxels can be seen, with bumps creating 4×4 three-axial taxels; on the right part only one novel three-axial taxel is shown, consisting of four 1D elements

To calculate the three new components of one novel three-axial taxel we use the following simple equations (with the notation of Figure 6.13):

$$
\begin{aligned}
\tilde{T}_x &= S_4 - S_1, \\
\tilde{T}_y &= S_2 - S_3, \\
\tilde{T}_z &= \frac{1}{2}\left(S_1 + S_2 + S_3 + S_4\right),
\end{aligned}
\tag{6.1}
$$

where S_i ($i = 1, 2, 3, 4$) denotes the four signals of the four 1D taxels. We need to rotate the two shear components of (6.1) with 45 degrees counterclockwise to have components parallel to the sensor grid. Thereby we get:

$$
\begin{aligned}
T_x &= \frac{\sqrt{2}}{2}\left(-S_1 + S_2 - S_3 + S_4\right), \\
T_y &= \frac{\sqrt{2}}{2}\left(S_1 - S_2 - S_3 - S_4\right), \\
T_z &= \frac{1}{2}\left(S_1 + S_2 + S_3 + S_4\right).
\end{aligned}
\tag{6.2}
$$

With the described method the number of taxels will be reduced by a factor of 4 and the sensor spacing will be doubled, but we will gain shear information, which is a comparable advantage.

Finally, using the FE results we can calculate the hypothetical response of our new sensors as a function of load amplitude. Results can be seen in Figure 6.14.
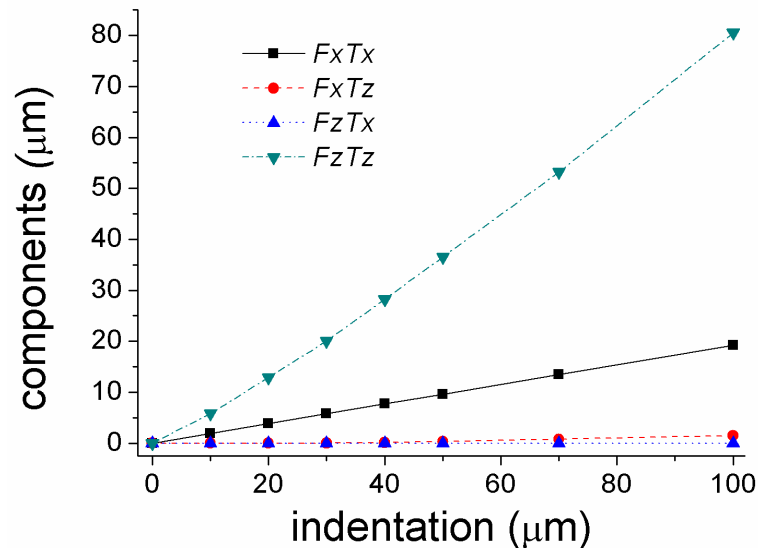
Figure 6.14.   Calculated components of the novel three-axial sensor (for explanation of the legend, see Figure 6.11)

The calculated components are again proved to be independent, with linear response to each load type. This sensor's normal-to-shear sensitivity is around 4, and gets even bigger if we count with the fact that most pressure sensors measure only compressive stress/deformation. Nevertheless, this constraint does not affect the overall functionality of the sensors.

6.4.4. Preliminary experiments on the two novel sensor types with bumps

We created the novel elastic covers for both mentioned sensor types (the used three-axial and a simple pressure sensor array), using the same materials[18] again. On the MFA sensors the diameter of the bumps is 400 μm, as in the FE model. The sensor-to-sensor distance of the taxels and, therefore, that of the bumps is 1.5 mm. The mold for the rubber was made by a silicon wafer. The negative bumps were constructed with simple

---

[18] Elastosil® RT-601 (Wacker Chemie GmbH)

isotropic etching, like the ridges. Our three-axial sensors are arranged in a 2×2 array hence four bumps were created with the mold (left side of Figure 6.15).

The other cover was made for a previously mentioned, commercially-available pressure sensor array, the XSensor. On this device we had bumps with a diameter of 2 mm, which roughly fits the calculated size of the FE model for this type of sensor (1.5 mm sensor spacing). This rubber was made in an aluminum mold. The negative bumps were created using an array of finely-positioned steel bearing-balls extruded into the aluminum. The pressure-sensor array had 9×9 1D taxels; thereby we got a 4×4 array of bumps, spaced 3 mm (right side of Figure 6.15).
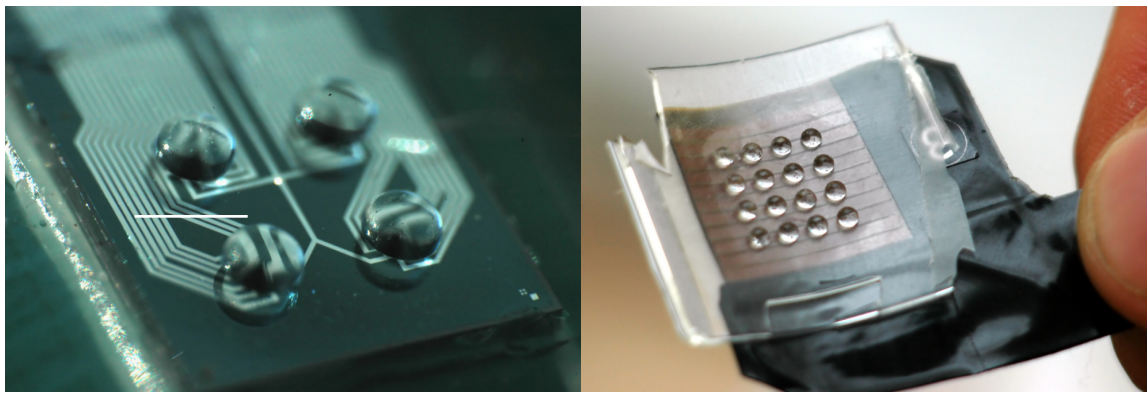
Figure 6.15.   The two sensor arrays with the elastic bumps: 2×2 array of the three-axial sensors (left);
9×9 element 1D XSensor covered by the 4×4 sized array of bumps (right)

The two covers had a flat layer of 200 and 500 µm under the bumps, consequently, representing the finite approximation of the half space. The elastic layers were finely positioned and fixed over the sensors.

As an initial quantitative measurement of the function of the hemispheres on the MFA sensors, I simply attached a second special cover over an array with a thin flat cover, in a way that one taxel obtained a bump above it and another one did not. Then my finger (as an arbitrary load) was moved around many times concentrically over the sensors. This experiment is rather a real tactile scene than a precise measurement, but results in Figure 6.16 clearly prove that sensors with elastic bumps on top have increased lateral sensitivity, they react more vigorously to arbitrary forces.
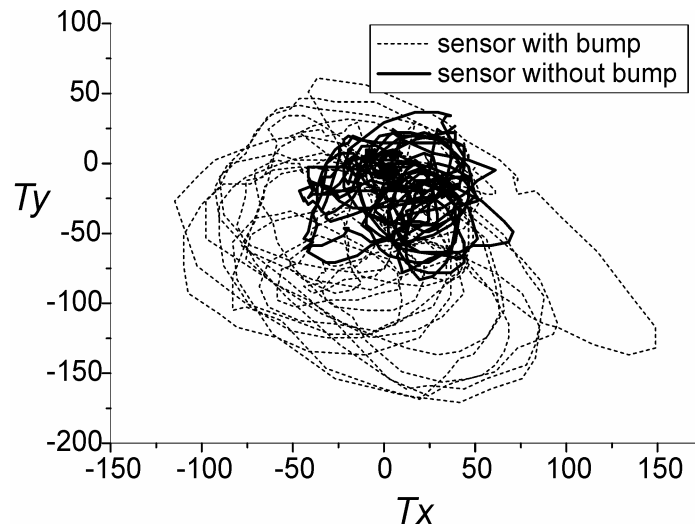
Figure 6.16.   Response of two identical sensors, one with an extra bump on top of the elastic layer. The two axes are the two tangential strain components—curves thereby correspond more or less to the lateral finger motion over the sensors. Sensitivity is increased by the elastic fingerprint-like bump (chip No.: 8b)

I also tested the shear-force sensing capabilities of the enhanced pressure-sensor array with similar simple but spectacular experiments, using the non-writing end and the side of a pencil as an indentation and pressing it against the taxels circularly. The 1D signals were converted to 3D data, and displayed with MatLab (Figure 6.17). Results show that the 1D to 3D conversion of tactile data using the bumps is applicable; the 3D vectors nicely follow the path of the circularly moving point and line indentations. The noise on the unloaded taxels comes from the XSensor itself. There is minimal cross-talk between the neighboring taxels.
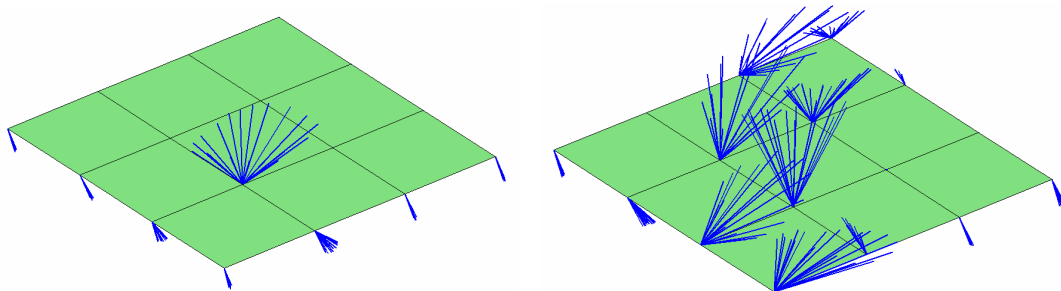
Figure 6.17.   3D vectors calculated from 1D tactile data when one bump is pressed (left), or when a thick line load is present (right). The arrangement of the successive vectors nicely follows the circular shear motion of the indentation in both cases

6.5. Texture classification using the bumpy cover

In this last section I show an application example with the final sensor design. We will once again use our three-axial MEMS devices and will restrict ourselves to the analysis of the signal of one single taxel, as in the previous sections. The array properties of the

same sensors are also investigated by Kis et al. (2006 [1]) during a robotic manipulation task. There one smooth object was held between two fingers of a robot arm. Both fingers were equipped with one 2×2 sensor array. The continuous signal of the two shear components of each taxel in the 2×2 arrays was reduced to the binary direction (+ or –), still resulting in $2^{8 \times 2} = 65536$ possible classifiable tactile events, used for tactile feedback for the robot arm. If we enlarge the number of taxels in the array even more, use more than one bit signals and investigate the spatial-temporal response of complex object profiles (as in any of our own general biological tactile-manipulation tasks), any analysis of these complex, multi-dimensional signal arrays will demand high speed, possibly parallel processing. One ideal cellular-wave computer for this task is the CNN universal machine (Roska and Chua, 1993 [70]) that could be our signal-processing hardware in the future on more extended tactile arrays and tasks. Up to now, we have only 2×2 sized arrays, but as we said we restrict ourselves even more and first we take a look at the spatial-temporal multi-bit signal of *one single taxel* on textured objects.

To show the functionality of the sensors now equipped with the new bumpy cover, we measure the response of different material types pulled over the hemispheres, and extract simple features from the spatial-temporal signals for a basic texture classification.

For the first basic experiments four materials were selected with different texture and roughness. They were pulled over the bumps in all directions, many times within a relatively narrow speed range, but with different amplitude. The characteristic three-axial response to these four materials measured by one of the taxels is shown in Figure 6.18.
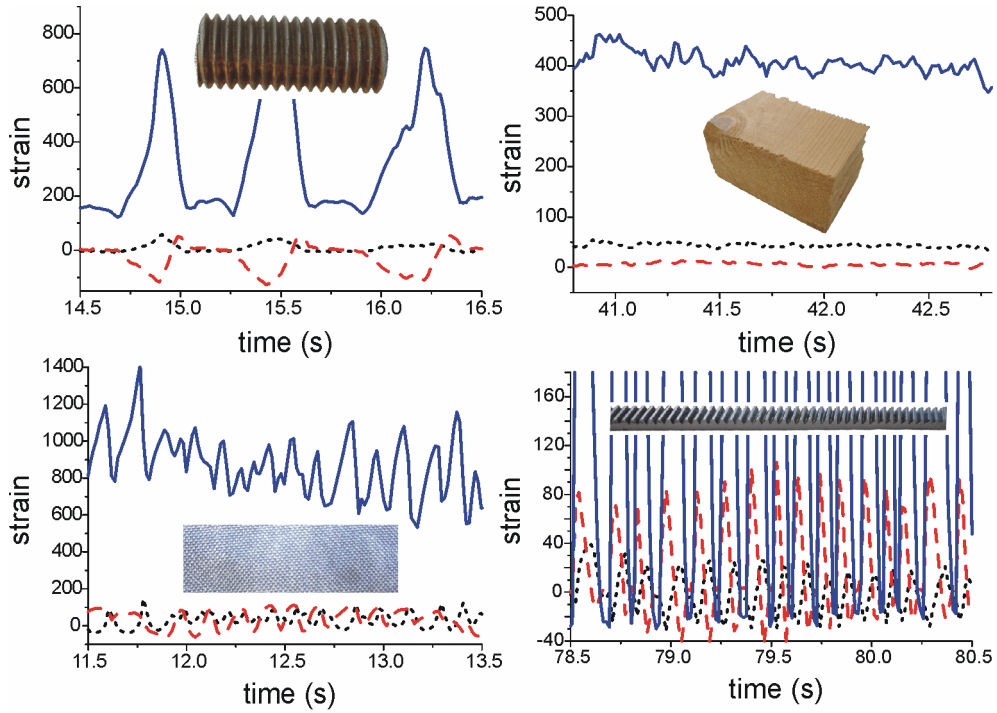
Figure 6.18.   Characteristic three-axial response of a taxel with bump to four different materials pulled over the surface in a straight line. The solid line is the normal, the dotted ones are the two shear components. The four materials: screw, smooth wood, fine textile, rasp

As can be seen in the above figure, the three-axial response of the taxel represents the one dimensional texture of the materials with characteristic features. The changes in the normal component correspond to the fine structure of the surface, while its averaged amplitude shows how much the object was pressed against the sensor. Motion direction can be extracted from the ratio of the shear components, while the ratio of the shear and normal components determines the friction coefficient. The overall raggedness of the signals corresponds to the surface roughness, etc.

My aim in the first run was to extract a few simple features from these signals that are available only in three-axial measurements and are insensitive to motion direction and the overall force applied. I selected two features to create a sample two dimensional classification. One is the *friction coefficient*, averaged on the last T discrete measurement points at time t:

$$\bar{\mu}(t) = \sum_{i=t-T}^{t} \mu(i) = \sum_{i=t-T}^{t} \sqrt{\frac{T_x(i)^2 + T_y(i)^2}{S_n(i)^2}} \quad . \tag{6.3}$$

The other one is an arbitrarily chosen, but good descriptive factor of the *surface roughness* that is defined as the normalized standard deviation of the instantaneous friction coefficient, calculated again on *T* values:

$$R(t) = \frac{100}{\bar{\mu}(t)} \sqrt{\frac{\sum_{i=t-T}^{t} (\bar{\mu}(t) - \mu(i))^2}{T-1}} .$$

(6.4)

In the definition of *R(t)* the multiplicative factor of 100 is used to push the values of the parameter into the integer range. In the experiments *T* was set to 128. Since the scanning time between the frames was 15 ms, the averages at a time were taken from the preceding 2 seconds, accordingly. The result of the classification on these two parameters, with around 3000 data points can be seen in Figure 6.19.
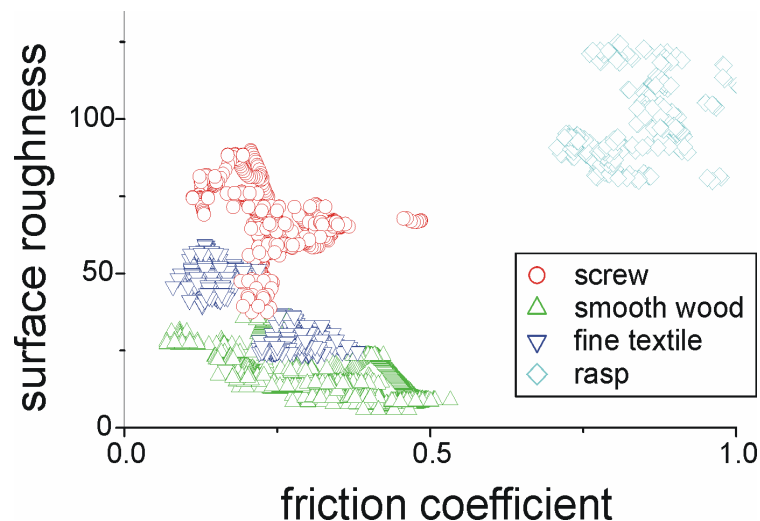
Figure 6.19.   Result of the first basic texture classification. Each of the approximately 3000 points represents one measurement of the two properties. Although the standard deviation of the properties of each material is huge, the classification is applicable even in this case

The above results show that the three-axial signals coded with the elastic hemispheres represent the object's texture properties with high fidelity, and even these two extracted features give us a relatively separable parameter space for texture classification. Introducing some more newly-defined characteristic features, the parameter space can be extended to a lot more dimensions and hence the classification can be improved essentially. Nevertheless, this classification is only an example of the many uses of the new three-axial sensors. They can be used in many other fields concerning tactile

manipulation, texture identification, robotic grip tasks or medical applications, where shear information can improve the quality of the data gained from the tactile sensors.

6.6. Conclusion

In this chapter we gave alternatives to the solution of the complex inverse problem of the elastic cover. We introduced neuromorphic hair- and fingerprint-like elements to the sensor design to enhance the tactile-event detection capabilities of the overall sensory structure, by coding different properties of the indentation profile more directly. With the new designs we could enhance the sensor's sensitivity to different indentation types and features without reducing the level of protection. The extra elements were proved to be efficient, and could be used for extending our knowledge on our own tactile system, too.

In the second part of the chapter we used a finite-element model to analyze the function of elastic hemispheres protruding from the cover surface. Applying these simple bumps on three-axial sensors, we found that they efficiently localize the spatially continuous input over the taxels and code normal and shear load components independently, with linear behavior, abolishing the need for a complex inverse-solution. Properly applying the elastic bumps on an arbitrary pressure-sensor array, we are also able to extract reliable and real-time shear-load information from the one-axial sensors.

The reliability of the theoretical considerations is supported by experimental results in an example texture classification task.

Chapter Seven

SUMMARY

7.1. Main direction of research

In my dissertation I analyzed the behavior of novel three-axial piezoresistive sensors, designed in the MEMS laboratory of MTA MFA. My work stands somewhere between the actual technological process of the sensor development and the final user-side applications. I mainly dealt with the physical description and the characterization of the sensors, first in their pure form and later equipped with different elastic covers. The cover can be treated as the first information-coding layer of the sensory structure, which is a "painful" obstacle when one wants to decode the surface-load profile from the measured, coded signals. Consequently, I gave only one analytic solution to this challenging inverse problem—for the most basic case, the point load. However, we can also exploit the features of this coding mechanism with the conscious design of the cover geometry. Therefore, I added neuromorphic elements to the sensor design to simplify the cover's behavior and thus enhance the overall capabilities and functionality of the sensors. I experimented with hair- and fingerprint-like elements, and finally analyzed the effects of elastic hemispheres over the cover surface. In addition to support the concept on the role of these elements in nature, I could also efficiently improve the characteristics of our sensors. Moreover, I could also use the elastic hemispheres for measuring shear load with simple pressure sensors.

7.2. New scientific results

Thesis I: Qualification of tactile sensors and their elastic cover

To work with tactile sensors efficiently and reliably, we need to be familiar with their performance. First, we need to compare their theoretical response with the measured one, without a cover. Second, we need to characterize our sensors again in the presence of the simplest, flat elastic covers. Finally, we have to support the applicability of the elastic model describing the behavior of the cover, with measurements both in the direct and the inverse approaches.

I.1. I worked out the exact physical model of the MEMS suspended-bridge type, piezoresistive, three-axial tactile device of the MFA, and verified this model and the preliminary finite-element simulations with characterizing experiments on a new, complex measurement setup.

Using the literature, I adjusted the theoretical description of the sensors to describe precisely the bulk micromachined tactile device of the MFA. The linear characteristics of the model and the sensitivity of the sensors predicted by the preliminary finite-element simulations are in accordance with the real measurements performed on the complex experimental setup.

I.2. Establishing high spatial-resolution, three-axial measurements, I verified that the infinite elastic half-space model describes the behavior of the finite, flat elastic covers well. Relying upon my experimental results, I confirmed that the signals of the covered sensors are proportional to three components of the local strain tensor of the cover.

Using a flat elastic cover, the receptive field of a sensor turns into a spatially-continuous, extended region, where the sensitivity of the device is highly inhomogeneous, as described by the material's model. I measured this three-component receptive field distribution with a spatial resolution of 3 µm over the total sensitive area of one single sensory element. I compared the measured distribution with the one predicted by the half-space model and confirmed that the measured signals are proportional to the strain-tensor components, even though it was assumed before that they represent the stress tensor.

I.3. I solved the inverse problem of the elastic half-space for an arbitrary point load, and using the results, I established tactile hyper-accuracy on sensors with a flat cover.

Using the known coding mechanism of the flat elastic cover, I found a solution to determine the exact location, direction and amplitude of an arbitrary point load over the cover surface. I utilized my theoretical results on the sensors and in the meantime verified them with measurements: using the three signals of one single element of a tactile array, I calculated the location of a normal point load on a receptive field size of 300×300 µm with 3 µm (1%) accuracy. I also determined the amplitude of the load

reliably. I integrated the solution into the software environment resulting in a real-time algorithm.

Thesis II: Neuromorphic elements in the tactile-sensor design

The surface of the high-resolution tactile systems of nature is not flat in most of the cases. Instead, it is usually equipped with fingerprints, different kinds of grooves or hair. Thoroughly investigating the role of these characteristics in biological systems, I could introduce new aspects into the artificial sensor design. Using the fingerprints as a model, I changed the geometry of the previously used flat surface to alter several properties, the sensitivity and the general coding mechanism of the cover on purpose. The most important new results are the following:

II.1. Introducing hair- and fingerprint-like elements into the sensor design, I changed the sensors overall characteristics, increased their sensitivity and experimentally verified the role we believe these elements have in biological systems.

Since the complex coding mechanism of the flat elastic cover makes signal processing quite problematic, I designed non-flat covers with specific neuromorphic shape and structure. In addition to successfully improving the characteristics of the sensors and increasing their shear-sensitivity, I also validated the hypotheses that fingerprints are crucial signal-coding and amplifying structures, while hairs are fundamental in shear-load sensing.

II.2. Using finite-element simulation results, I proved that by consciously designing the geometry of the cover, its coding mechanism can be simplified efficiently. Applying elastic hemispheres on the cover surface, I provided a method for localizing the input load and for measuring the three force components directly and independently under the cover.

I verified my theoretical results on the three-axial sensors through a texture-classification example. Using the hemispheres, on the one hand, I maintained the physical protection of the cover; on the other hand, I localized the originally continuous input and thus avoided the inverse-calculation problems originally coming from the complex coding mechanism of the material.

II.3. Using elastic hemispheres on an arbitrary pressure-sensor array, I developed a design plan for a special cover, which enables the extraction of independent shear-load components from the originally one-axial sensors.

The elastic hemispheres can be applied successfully on simple one-axial pressure-sensor arrays as well. In this case one hemisphere covers four one-axial elements of the sensor array. Combining these four signals I gained shear-load information effectively—based on the finite-element simulation results again. The method can be used generally on an arbitrary pressure-sensor array, with any size or element number. I verified my theoretical assumptions with measurements on a 9×9 element capacitive array.

7.3. Application potential

7.3.1. New practical results

There is one main practical result of my work, namely that the three-axial sensors that are being developed for many years now, have reached such a maturity level that they can be used in an arbitrary tactile task without the fuss of interpreting their signals. The sensors with elastic hemispheres code the three component of any surface indentation reliably at every taxel, and the signal of the sensors can be analyzed through a special software that can be executed in a standard PC. In other words, our product—the sensor structure with its cover, the amplification stage and the software background—is close to commercialization now[19].

In my opinion, a promising practical result is the presented opportunity of shear-load measurement using arbitrary pressure-sensor arrays. Although the shear sensitivity of these sensors is not as high as that of our original three-axial sensors, they definitely work. Moreover, the new procedure enables the construction of arbitrary sized, even flexible, three-axial arrays, where the limits of the design are much further away, along with the 10–20 year advantage of the pressure-sensor technology over the development of the three-axial sensor arrays, which are not even available yet.

---

[19] Note that this is a joint work. Special thanks to Attila Kis who's merit is the development of the amplification stage and huge parts of the software, and obviously to the members of the MEMS Laboratory for the sensors.

7.3.2. Examples of application and future trends

The applicability of my results obviously goes along with that of tactile sensors. Their most "handy" function is in an arbitrary grip task on robotic arms. In addition to the industrial use and scientific research aims, nowadays a more and more active market is opening in the medical research field. We can utilize our sensors on endoscopes where manual touch is unattainable. Combining the sensors with a proper haptic display we can construct a system that helps in virtual tele-operation projects. In the long run the sensors could be used as a substitute for the mechanoreceptors on the arm prostheses of amputees.

Throughout all my work I mainly analyzed the temporal behavior of single elements of tactile arrays, without taking into consideration spatial features on neighboring elements. Therefore, in the future I am about to extend my investigations to dynamic tactile scenes, using a cellular-wave computer for signal processing and our new 8×8 element, three-axial tactile-sensor arrays, where the standard CMOS technology and the porous-silicon etching is efficiently combined in a novel smart-sensor design (Figure 7.1).
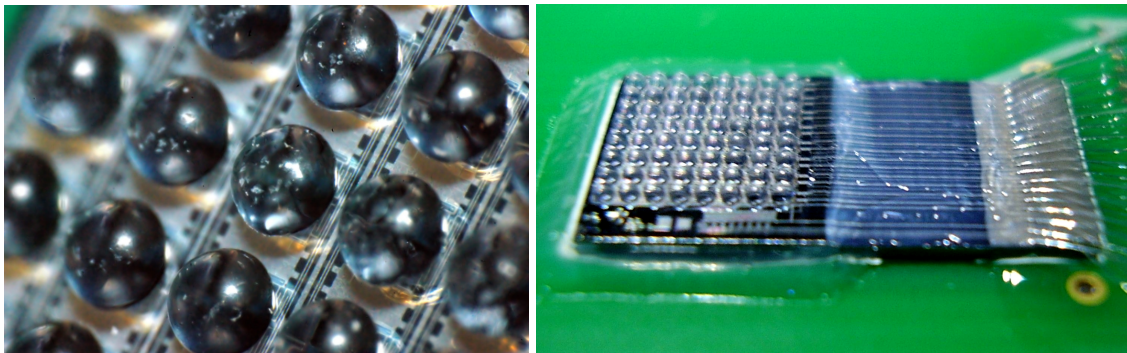

Figure 7.1.   The new 8×8 sensor array

BIBLIOGRAPHY

The whole bibliography is grouped according to either the scientific laboratories and main scientists they originate from, or in the case of single articles, the main scientific field they are related to. The order of the articles is not corresponding to the order of their appearance as a reference in the text. All the articles that are cited in the dissertation have a short summary following them—some additional interesting articles are listed in each group afterwards.

Jedlik Laboratories (PPKE ITK, Budapest)

[1] A. Kis, F. Kovács, P. Szolgay: "3D Tactile Sensor Array Processed by CNN-UM: A Fast Method for Detecting and Identifying Slippage and Twisting Motion," *International Journal on Circuit Theory and Application (CTA), special issue on CNN,* 2006; 34: 517–531

   An article about the application of our sensor arrays on robotic arms for tactile event detection.

[2] A. Kis, F. Kovács, P. Szolgay: "Hardware and Software Environment for a Tactile Sensor Array," *Proceedings of Eurosensors XIX*, 2005, Barcelona, Spain, pp. 324–328

[3] A. Kis, F. Kovács, P. Szolgay: "Grasp Planning Based on Fingertip Contact Forces and Torques," *Proceedings of Eurohaptics 2006,* Paris, France, pp. 455–459

MTA MFA (Budapest)

[4] Zs. Vízváry, P. Fürjes, M. Ádám, Cs. Dücső, I. Bársony, "Mechanical Modelling of an Integrable 3D Force Sensor by Silicon Micromachining*," National Institute for Research and Development in Microtechnologies (Bucharest) (ed.) Special issue featuring selected papers from the 13th European Micromechanics workshop*, MME '02, Bristol: Institute of Physics Publishing, 2003. pp. 165–168

   Details of the mechanical modeling of our three-axial sensors.

[5] É. Vázsonyi, M. Ádám, Cs. Dücső, Zs. Vízváry, A.L. Tóth, I. Bársony, "Three-dimensional Force Sensor by Novel Alkaline Etching Technique," *Sens. Actuators A*, vol. 123–124, no. 23, Sep. 2005, pp. 620–626

   The novel type three-axial sensor that has a rod in the middle of the deformable membrane, mimicking the role of a hair.

Ron S. Fearing (Robotics, Berkeley)

[6] R. S. Fearing, J. M. Hollerbach, "Basic Solid Mechanics for Tactile Sensing," *Int. J. of Robotics Research*, 1985, vol. 4, no. 3

   The first article of Fearing. He uses the elastic half-space model to describe the effects of the tactile sensor's cover for the first time. Point load, line load, normal and shear stress, but all in theory, without real sensors. Mentions the inverse problem and gives partial and not practical solution for a line load. Also mentions the effect of fingerprints in theory.

[7]   R. S. Fearing, "Tactile Sensing Mechanisms," *Int. J. of Robotics Research*, 1990, vol. 9, no. 3, pp. 3–23

      This is a very important article of Fearing, which is cited the most by others, but unfortunately I have not had the opportunity so far to read it… Linear inverse-filtering processes are introduced in it.

[8]   R. S. Fearing and T. O. Binford, "Using a Cylindrical Tactile Sensor for Determining Curvature," *IEEE Transactions on Robotics and Automation*, 1991, vol. 7, no. 6, pp. 806–817

      Non-linear inverse-filter processes to determine the curvature and location of objects, but the methods are far from real-time. They also work in a spatial domain where the characteristic sizes are about one order of magnitude larger than ours.

[9]   U. Singh, R.S. Fearing, "Tactile After-Images from Static Contact," *7th Symp. on Haptic Interfaces for Virtual Environment and Teleoperator Systems*, ASME IMECE Anaheim, CA Nov. 1998

      An investigation about the viscoelasticity of the finger skin for designing tactile displays. The effect of large forces remain in the skin for a few seconds, which is important to know when one is designing a tactile display. They present detailed psychophysical results and a viscoelastic finger model.

[10] G. Moy, R.S. Fearing, "Effects of Shear Stress in Teletaction and Human Perception," *7th Symp. on Haptic Interfaces for Virtual Environment and Teleoperator Systems,* ASME IMECE Anaheim, CA Nov. 1998

      They state that in a tactile display design shear stress decreases the functionality of the display. Therefore, they investigate how shear stress can be reduced with the application of different elastic layers. Results are based on psychophysical measurements.

[11] G. Moy, U. Singh, E. Tan, R.S. Fearing, "Human Psychophysics for Teletaction System Design," *Haptics-e The Electronics Journal of Haptics Research*, 2000, vol. 1, no. 3

      A useful, long and detailed article for tactile displays, treating their inverse problem: what should be displayed to have a certain sensation. Linear elastic model with viscoelasticity, grating orientation discrimination, etc.

[12] R. S. Fearing, G. Moy, E. Tan, "Some Basic Issues in Teletaction," *IEEE Int. Conf. Robotics and Automation*, April 1997

[13] E. J. Nicolson, R. S. Fearing, "The Reliability of Curvature Estimates from Linear Elastic Tactile Sensors," *ICRA* 1995, pp. 1126–1133

Kenneth O. Johnson
(Mind/Brain Institute, Johns Hopkins University)

[14] K. O. Johnson, J. R. Phillips, "Tactile Spatial Resolution I. Two Point Discrimination, Gap Detection, Grating Resolution, and Letter Recognition," *J. Neurophysiology*, 1981, vol. 46, no. 6, pp. 1177–1191

[15] K. O. Johnson, J. R. Phillips, "Tactile Spatial Resolution II. Neural Representation of Bars, Edges, and Gratings in Monkey Primary Afferents," *J.Neurophysiology*, 1981, vol. 46, no. 6, pp. 1192–1203

[16] J. R. Phillips, K. O. Johnson, "Tactile Spatial Resolution III. A Continuum Mechanics Model of Skin Predicting Mechanoreceptor Responses to Bars, Edges, and Gratings," *J. Neurophysiology*, 1981, vol. 46, no. 6, pp. 1204–1225

A fantastic "trilogy" about the function of the mechanoreceptors, their signaling details and receptive field properties. It is the first article describing the skin with continuum-mechanics and stating that the skin itself has information coding behavior. It investigates the response of different indentations through the neural channels of rhesus monkeys and compares the results with the continuum-mechanical theory. Worth reading!

[17] K. O. Johnson, "The Roles and Functions of Cutaneous Mechanoreceptors," *Current Opinion in Neurobiology*, 2001, vol. 11, pp. 455–461

A remarkable review on the roles and functions of cutaneous mechanoreceptors, as can be assumed by the title... Another great work of K. O. Johnson.

Mandayam A. Srinivasan (M.I.T. Touch Lab)

[18] M. A. Srinivasan, K. Dandekar, "An Investigation of the Mechanics of Tactile Sense Using Two Dimensional Models of the Primate Fingertip," *J. Biomechanical Engineering*, 1996, vol. 118, pp. 48–55

A very good article about the first (2D) finite-element model of the primate fingertip. It compares the elastic half-space with finite-element models of different complexity, stating that the difference is not significant. Obviously, the more precise models have more details but response shapes are more or less similar.

[19] K. Dandekar, B. I. Raju, M. A. Srinivasan, "3-D Finite-element Models of Human and Monkey Fingertips to Investigate the Mechanics of Tactile Sense," *J. Biomech. Eng*, 2003, vol. 125(5), pp. 682–91

Same model as before, but now three dimensional. More detailed analysis of the materials but no big change in the output. Mentions but does not incorporate viscoelasticity and finger ridges.

[20] M. A. Srinivasan, J. M. Whitehouse, R. H. LaMotte, "Tactile Detection of Slip: Surface Microgeometry and Peripheral Neural Codes," *J. Neurophysiol*, 1990, vol. 63(6), pp. 1323–32

[21] J. Biggs, M. A. Srinivasan, "Tangential Versus Normal Displacement of Skin: Biomechanics and Perceived Intensity," *Experimental Brain Research* (submitted, 2003)

Makoto Shimojo
(The University of Electro-Communications, Tokyo, Japan)

[22] M. Shimojo, "Spatial Filtering Characteristic of Elastic Cover for Tactile Sensor," *IEEE Int. Conf. on Robotics and Automation*, San Diego, CA, 1994, pp. 287–292

A basic and useful article about the spatial filtering characteristics of the elastic cover, with apparently very poor English… He analyzes the low-pass filtering properties of the point load solution, and its dependence on the value of the Poisson's ratio and Young modulus.

[23] M. Shimojo, "Mechanical Filtering Effect of Elastic Cover for Tactile Sensor," *IEEE Transactions on Robotics and Automation*, 1997, vol. 13, no. 1, pp. 128–132

Same as the previous one, but longer article and with some preliminary, low spatial-resolution measurements on pressure sensors.

[24] M. Shimojo, T. Suzuki, A. Namiki, T. Saito, M. Kunimoto, R. Makino, H. Ogawa, M. Ishikawa, K. Mabuchi, "Development of a System for Experiencing Tactile Sensation from a Robot Hand by Electrically Stimulating Sensory Nerve Fiber," *2003 IEEE International Conference on Robotics and Automation,* pp.1264–1270

Takashi Maeno (Keio University, Yokohama, Japan)

[25] T. Maeno, K. Kobayashi, N. Yamazaki, "Relationship Between the Structure of Human Finger Tissue and the Location of Tactile Receptors," *JSME International Journal*, 1998, vol. 41, pp. 94–100

> An interesting new aspect but not quite convincing proofs. Finite-element model of the human fingertip with skin layers, the bone and fingerprints included. The goal is to provide an explanation for the location of the four mechanoreceptors. Good start, good ideas, but not enough knowledge about neurobiology, in my opinion…

[26] D. Yamada, T. Maeno, Y. Yamada, "Artificial Finger Skin Having Ridges and Distributed Tactile Sensors used for Grasp Force Control," *Journal of Robotics and Mechatronics*, 2002, vol. 14, no. 2, pp. 140–146

> The first tactile sensor with a ridged surface! Their idea is the basis of some of my results. Shear-strain measurement on a huge tactile sensor, used for slippage detection. Good review of slippage detection with many citations.

[27] Y. Mukaibo, H. Shirado, M. Konyo, T. Maeno, "Development of a Texture Sensor Emulating the Tissue Structure and Perceptual Mechanism of Human Fingers," *Proc. IEEE International Conference on Robotics and Automation*, 2005, pp. 2576–2581

> This paper discusses a novel approach in developing a texture sensor emulating the major features of a human finger, like nails, layered soft tissues, epidermal ridges and receptors at different sites in the skin. They use the sensor for softness, roughness and friction estimation of textures.

[28] T. Maeno, T. Kawai, K. Kobayashi, "Analysis and Design of a Tactile Sensor Detecting Strain Distribution Inside an Elastic Finger," *Proc. IEEE/RSJ International Conference on Intelligent Robots and Systems, 1998*, pp. 1658–1663

[29] H. Shirado, T. Maeno, "Modeling of Human Texture Perception for Tactile Displays and Sensors," *The First Joint Eurohaptics Conference and Symposium on Haptic Interface for Virtual Environment and Teleoperator Systems*, 2005, p. 57 (obtained the Best Poster Award)

Danilo De Rossi (Università di Pisa)

[30] C. Domenici, D. De Rossi, "A Stress-Component Selective Tactile Sensor Array," *Sens. Actuators A*, 1992, vol. 31(1–3), pp. 97–100

> A piezoelectric-polymer based tactile sensor measuring six independent components of the stress. One 6-axial sensor is composed of 6 crystals, and a total of 42 elements (7 taxels) are presented in an array. No reliable measurement of shear stress yet.

[31] D. De Rossi, G. Canepa, G. Magenes, F. Germagnoli, A. Caiti, T. Parisini, "Skin-like Tactile Sensor Arrays for Contact Stress Field Extraction," *Material Sciences Engineering C1*, 1993, pp. 23–36

> Another detailed description of the same piezoelectric tactile sensor, with the analysis of the forward elastic problem.

[32] A. Caiti, G. Canepa, D. De Rossi, F. Germagnoli, G. Magenes, T. Parisini, "Towards the Realization of an Artificial Tactile System: Fine-form Discrimination by a Tensorial Tactile Sensor Array and Neural Inversion Algorithms," *IEEE Transactions on Systems, Man and Cybernetics*, 1995, vol. 25, issue 6, pp. 933–946

Numerical solutions to the inverse problem of the elastic cover using neural networks. They try to determine object shapes. Still no reliable shear-load data from the piezoelectric sensors.

[33] F. Lorussi, E.P. Scilingo, M. Tesconi, A. Tognetti, and D. De Rossi. "Strain Sensing Fabric for Hand Posture and Gesture Monitoring," *IEEE Transactions on Information Technology in Biomedicine*, 2005, vol. 9(3), pp. 372–381

[34] G. Canepa, O. Sottile, D. De Rossi, "Extraction of Cutaneous Primitives from Tactile Sensor Images," *IEEE International Conference on Systems, Man, and Cybernetics, 1994. 'Humans, Information and Technology',* 1994, vol. 3, pp. 2641–2646

The Mass Group (University of Illinois at Urbana-Champaign)

[35] J. Engel, J. Chen, and C. Liu, "Development of a Multi-Modal, Flexible Tactile Sensing Skin Using Polymer Micromachining", The *12th International Conference on Solid-State Sensors, Actuators and Microsystems*, Boston, MA, 2003, vol. 2

[36] J. Engel, J. Chen, and C. Liu, "Development of Polyimide Flexible Tactile Sensor Skin," *Journal of Micromechanics and Microengineering*, 2003, vol. 13, no. 3, pp. 359–366

[37] J. Engel, J. Chen, Z. Fan, and C. Liu, "Polymer Micromachined Multimodal Tactile Sensors," *Sens. Actuators A*, 2005, vol. 117, no. 1, pp. 50–61

[38] S-H. Kim, J. Engel, C. Liu, D. L. Jones, "Texture Classification Using a Polymer-based MEMS Tactile Sensor," *Journal of Micromechanics and Microengineering*, 2005, vol. 15, pp. 912–920

Theory of elasticity, elastic half-space model, elastic cover

[39] J. Boussinesq, "Application des Potentials à l'etude de l'équilibre et du movement des solides élastiques," *Paris: Gauthier-Villars*, 1885

The first solution of the equilibrium equations of solid elastic bodies, through the elastic-half space model

[40] A. Flamant, *Paris Compt. Rend.*, 1892, vol. 114, pp. 1465–1465

[41] S. Timoshenko, J. N. Goodier, "Theory of Elasticity,", New York:McGraw-Hill, 1951

[42] A. E. H. Love, "The Mathematical Theory of Elasticity", 4th Edition, Cambridge Univ. Press, 1952

These three above contain basics of the theory of elasticity and the first solutions in the framework of the elastic half-space model.

[43] F. Zee, E. M. G. Holweg, W. Jongkind, G. Honderd, "Shear force measurement using a rubber based tactile matrix sensor," *Proc. 8th Int. Conf. Advanced Robotics, Monterey, CA*, 1997, pp. 733–737

Three-axial tactile array, using conductive, silicon-based rubber. To measure shear forces, they make cuts on the rubber surface, where each section is over a 2×2 normal force sensing sub-array. Same idea as ours, but less effective design of the cover…

[44] N. Chen, H. Zhang, R. Rink, "Tactile Sensing of Point Contact," *IEEE International Conference on Systems, Man and Cybernetics, 1995. 'Intelligent Systems for the 21st Century'*, 1995, vol. 1, pp. 574–579

Inverse problem of the elastic cover using moments and iterative algorithms. They need to combine signals from more than one sensor at once, and lack good experimental data.

[45] G. J. Gerling, G. W. Thomas, "The Effect of Fingertip Microstructures on Tactile Edge Perception," WHC 2005, pp. 63–72

Finite-element model of the fingertip, specializing in the effect of the fingerprints and also taking into account the ragged border of the dermis and the epidermis. They state that the ridges create a so-called "lensing effect" that concentrates the stress to the receptor sites.

[46] M. R. Tremblay, M. R. Cutkosky, "Estimating Friction Using Incipient Slip Sensing During a Manipulation Task," *Proc. 1993 IEEE Int. Conf. Robotics and Automation,* 1993, pp. 429–434

Accelerometers embedded in an elastic material with bumpy surface. They use these bumps to transfer vibrations to the sensors when released by grip. They give a detailed description of the advantages of elastic bumps on a cover surface.

[47] J. Z. Wu, R. G. Dong, S. Rakheja, A.W. Schopper, W.P. Smutz, "A Structural Fingertip Model for Simulating of the Biomechanics of Tactile Sensation," *Medical Engineering and Physics*, 2004, vol. 26, no. 2, pp. 165–175

[48] D. J. Beebe, D. D. Denton, R. G. Radwin, J. G. Webster, "A Silicon-based Tactile Sensor for Finger-mounted Applications," *IEEE Transactions on Biomedical Engineering*, 1998, vol. 45, issue 2, pp. 151–159

[49] R. Kikuuwe, A. Sano, H. Mochiyama, N. Takesue, H. Fujimoto, "Enhancing Haptic Detection of Surface Undulation," *ACM Trans. Appl. Percept.* 2005, vol. 2(1) pp. 46–67

Three-axial tactile sensors

[50] H. Shinoda, N. Morimoto and S. Ando, "Tactile Sensing Using Tensor Cell," *Proc. 1995 IEEE Int. Conf. on Robotics and Automation*, 1995, vol. 1, pp. 825–830

A single-element six-degree-of-freedom tactile sensor.

[51] L. Zhu, J. W. Spronck, "A Capacitive Tactile Sensor for Shear and Normal Force Measurements," *Sens. Actuators A*, 1992, vol. 31(1-3), pp. 115–120

Another single-element three-axial tactile sensor, based on the capacitive working principle.

[52] K. Kamiyama, H. Kajimoto, N. Kawakami, S. Tachi, "Evaluation of a Vision-based Tactile Sensor," *Proc. of 2004 International Conference on Robotics and Automation*, 2004, WP-6

A three-axial tactile sensor based on an optical approach. There are many dots on an elastic surface, and when it deforms, they move. A CCD camera under the transparent elastic layer records the movement of the dots and calculates the three components of the surface displacement from it. Smart, eh?

[53] M. Ohka, Y. Mitsuya, Y. Matsunaga, S. Takeuchi, "Sensing Characteristics of an Optical Three-axis Tactile Sensor Under Combined Loading," *Robotica,* 2004, vol. 22, pp. 213–221

[54] M. Ohka, Y. Mitsuya, I. Higashioka, H. Kabeshita, "An Experimental Optical Three-axis Tactile Sensor for Micro-Robots," *Robotica*, 2005, vol. 23, pp. 457–465

Another optical approach to three-axial tactile sensing. Same idea, but instead of painted dots there are "conical feelers" over a rigid surface, with growing and moving contact area when deformed from above. CCD recording again from below.

[55] S. A. Mascaro, H. H. Asada, "Measurement of Finger Posture and Three-axis Fingertip Force Using Fingernail Sensors," *IEEE Transactions on Robotics and Automation*, 2004, vol. 20(1), pp. 26–35

   Optical solution again, but CCD now records the color of the nail from above. The colored pattern of the blood volume under the nail represents the type of indentation the finger itself has been exposed to.

[56] P. M. Chu, S. Sarro, S. Middelhoek, "Silicon Three-Axial Tactile Sensor," *Sens. Actuators A*, 1996, vol. 54, pp. 505–510

   Capacitive-type, three-axial force-sensor array, using four neighboring capacitances to estimate shear forces (same as our sensors, but not piezoresistive). No measurement results for the constructed 3×3 array; neither accurate enough on a single taxel.

[57] M. Hakozaki, H. Shinoda, "Digital Tactile Sensing Elements Communicating through Conductive Skin Layers," *Proc. 2002 IEEE Int. Conf. on Robotics & Automation*, 2002, pp. 3813–3817

   Capacitive-type three-axial sensor array, measuring oscillation frequency changes, with a lot of cross-talk between components and non-linear behavior. Also proposes an array but shows only one taxel.

[58] L. Wang, D. J. Beebe, "A Silicon-based Shear Force Sensor: Development and Characterization," *Sens. Actuators A,* 2000, vol. 84, pp. 33–44

   A silicon-based MEMS shear-force sensor, with a membrane as a deformable part. Four piezoresistors make up one three-axial taxel, like in our sensor. Contains detailed analysis of piezoresistivity.

[59] B. J. Kane, M.R. Cutkosky, G. T. A. Kovacs, "CMOS Cmpatible. Traction Stress Sensor for Use in High Resolution Tactile Imaging," *Sens. Actuators A*, 1996, vol. 54, pp. 511–516

[60] B. J. Kane, M. R. Cutkosky, G. T. A. Kovacs, "A Traction Stress Sensor Array for Use in High-Resolution Robotic Tactile Imaging," *Journal of Microelectromechanical Systems*, 2000, vol. 9, no. 4, pp. 425–434

   The first multiple-element three-axial tactile sensors, with an array size of 5×5 and 64×64 in the consecutive articles. Although their process is CMOS compatible, which is a crucial point in a large-array design, the structure suffers from the limited sensitivity of the poly-silicon structure and the mechanical stability of the multilayered membrane. However, the MEMS device of the MFA is based more or less on their sensing method.

Mechanoreceptors

[61] H. Ogawa, "The Merkel Cell as a Possible Mechanoreceptor Cell," *Prog Neurobiol.*, 1996, vol. 49(4), pp. 317–34

   A detailed analysis on the Merkel cell–neurite complex investigating the chemical basis of its mechanoreception.

[62] Z. Halata, M. Grim, K. I. Bauman, "Friedrich Sigmund Merkel and his "Merkel cell", Morphology, Development, and Physiology: Review and New Results," *Anat Rec A Discov Mol Cell Evol Biol.,* 2003, vol. 271(1), pp. 225–39

   A very good overview of the origin, development, localization, structure and function of Merkel cells in humans and animals.

[63] I. Moll, M. Roessler, J. M. Brandner, A. C. Eispert, P. Houdek, R. Moll "Human Merkel Cells – Aspects of Cell Biology, Distribution and Functions," *Eur J Cell Biol.*, 2005, vol. 84(2–3), pp. 259–71

Another good overview of the Merkel cells with more attention to cell biological aspects.

[64] K. C. Catania, "A Nose that Looks Like a Hand and Acts Like an Eye: the Unusual Mechanosensory System of the Star-nosed Mole," *J Comp Physiol A*, 1999, vol. 185, pp. 367-372

A fascinating review about the world's most developed tactile nose. If I were a mole I would be very proud of this detailed description, even though I could not see but touch it.

[65] J. N. Hoffmann, A. Montag, N. J. Dominy, "Meissner Corpuscles and Somatosensory Acuity: The Prehensile Appendages of Primates and Elephants," *Anatomical Record*, vol. A281, pp. 1138–1147

An interesting article about the proboscis of elephants and fingertips of primates. It tries to correlate the number of Meissner's corpuscles and the prehensile skills of these animals. It also discusses the role of papillary ridges on the skin surface and gives an interesting overview about the relationship between the location of Meissner's corpuscles and the papillary ridges in different species.

Role of fingerprints

[66] N. Cauna, "Nature and Function of the Papillary Ridges of the Digital Skin," *Anat Rec,* 1954, vol. 119, pp. 449–468

The first article mentioning the role of fingerprints in the mechanotransduction.

[67] R. D. Martin, "Primate Origins and Evolution: a Phylogenetic Reconstruction," *Princeton: Princeton University Press*, 1990

Details about the dual function of papillary ridges. They prevent slippage while serving as a mechanical amplification stage in the procedure of stress transduction in the skin.

[68] S. J. Bolanowski, L. Pawson, "Organization of Meissner Corpuscles in the Glabrous Skin of Monkey and Cat," *Somatosens Mot Res.*, 2003, vol. 20(3–4), pp. 223–31

One interesting result of this article is that Meissner's corpuscles in the fingertip of primates lie mostly along their fingerprint ridges, predicting a role for the fingerprints in the mechanotransduction.

[69] W. J. Babler, "Embryologic Development of Epidermal Ridges and Their Configurations," *Birth Defects Orig Artic Ser.*, 1991, vol. 27(2), pp. 95–112.

CNN technology

[70] T. Roska, L. O. Chua, "The CNN Universal Machine: An analogic array computer", *IEEE Trans. Circuits and Systems-II*, 1993, vol. 40, pp. 163–173

Fundamentals of the cellular neural/nonlinear networks.

[71] T. Roska, L.O. Chua, D. Wolf, T. Kozek, R. Tetzlaff, F. Puffer, "Simulating Nonlinear Waves and Partial Differential Equations via CNN—Part I: Basic Techniques," *IEEE Trans. Circuits and Systems*, 1995, vol. 42, pp. 807–815

[72] T. Kozek, L. O. Chua, T. Roska, D. Wolf, R. Tetzlaff, F. Puffer, K. Lotz, "Simulating Nonlinear Waves and Partial Differential Equations via CNN—Part II: Typical Examples," *IEEE Trans. Circuits Syst.*, 1995, vol. 42, 816–820.

These two are listed because I also wanted to solve the half-space equations on a CNN grid for simulating the behavior of the elastic cover under different indentations. However, results have not achieved such a maturity so far, to have them included in my official work now. Maybe next time :)

Books

[73] H. Hertz, "Principles of Mechanics," London; New York: Macmillan, 1899

[74] K. L. Johnson, "Contact Mechanics," *Cambridge University Press,* 1985

A very good introduction to contact mechanics from all aspects. Detailed description of the elastic half-space and its solutions to many special cases.

[75] E. R. Kandel, J. H. Schwartz, T. M. Jessell "Principles of Neural Science," *McGraw-Hill/Appleton & Lange*; 4th edition (January 5, 2000)

There is no need to introduce this one. It contains all the aspects and details of neurobiology—at the deepest scientific level that can fit in one book.

[76] L. D. Landau, E. M. Lifsic: "Elméleti fizika VII. kötet (Rugalmasságtan)," *TK*, Bp. 1974

The basics of the theory of elasticity for physicists. Very detailed, very accurate.

[77] S. M. Sze, "Semiconductor Sensors," *John Wiley & Sons, Inc*. NY, 1994

Piezoresistivity, MEMS sensors, etc. Useful even after working 10 years in the field of sensors...

THE AUTHOR'S PUBLICATIONS

Journal papers

[1] **G. Vásárhelyi**, M. Ádám, É. Vázsonyi, Zs. Vízváry, A. Kis, I. Bársony, Cs. Dücső, "Characterization of an Integrable Single-Crystalline 3D Tactile Sensor," *IEEE Sensors Journal*, Aug. 2006, vol. 6, no. 4, pp. 928–934

[2] **G. Vásárhelyi**, M. Ádám, É. Vázsonyi, I. Bársony, Cs. Dücső, "Effects of the Elastic Cover on Tactile-Sensor Arrays," *Sens. Actuators A*, 2006, vol. 132, pp. 245-251

[3] **G. Vásárhelyi**, B. Fodor, T. Roska, "Tactile Sensing-Processing: Interface Cover Geometry & the Inverse Elastic Problem," *Sens. Actuators A,* under review

Conference papers

[4] M. Ádám, É. Vázsonyi, I. Bársony, **G. Vásárhelyi** and Cs. Dücső, "Three Dimensional Single Crystalline Force Sensor by Porous Si Micromachining," *Proceedings of IEEE Sensors 2004*, Vienna, vol. 1, pp. 501–504

[5] Kis A., **Vásárhelyi G.**, Ádám M., Szolgay P. – "Taktilis Érzékelés: Szenzorok és Algoritmusok," *XI. MITT Kongresszus*, Pécs (2005)

[6] **G. Vásárhelyi**, M. Ádám, É. Vázsonyi, I. Bársony, Cs. Dücső, "Effects of the Elastic Covering on Tactile Sensor Arrays," *Proceedings of Eurosensors 2005*, Barcelona

[7] **G. Vásárhelyi**, B. Fodor, "Enhancing Tactile Capabilities with Elastic Hemispheres," *Proceedings of EuroHaptics 2006*, Paris, pp. 491–494

Patents pending

[8] **Vásárhelyi G.,** Kis A., Dücső Cs., Fodor B, "Rugalmas borítás tapintásérzékelőkhöz és rugalmas borítással ellátott tapintásérzékelő elrendezés," *Hungarian Patent,* No. P0600892 (submitted on 30/11/2006)

♣ Q.E.D. ♣